A QUALITATIVE SIMULATION OF BLOOD FLOW THROUGH AN ELASTIC CEREBRAL SACCULAR ANEURYSM USING AN IMMERSED BOUNDARY METHOD

by

BRIELLE C.'L. SUTTON

A DISSERTATION

Submitted in partial fulfillment of the requirements
for the degree of Doctor of Philosophy in the
Applied Mathematics Graduate Program
of Delaware State University

DOVER, DELAWARE
May 2018

This dissertation is approved by the following members of the Final Oral Review Committee:

Dr. Dawn A. Lott, Committee Chairperson, Department of Mathematical Sciences, Delaware State University
Dr. Matthew Tanzy, Committee Member, Department of Mathematical Sciences, Delaware State University
Dr. Jinjie Liu, Committee Member, Department of Mathematical Sciences, Delaware State University
Dr. Fengshan Liu, Committee Member, Department of Mathematical Sciences, Delaware State University
Dr. Charles J. Prestigiacomo, External Committee Member, Department of Neurological Surgery, University of Cincinnati

DEDICATION

To young people all around the world,

Don't let distractions block you from your goals and destiny.

Stay focused and keep your eyes on the prize. No matter how challenging the situation or how bad the circumstance, BE RESILIENT!

"*I can do ALL things through Christ which strengtheneth me.*"

Philippians 4:13 KJV

ACKNOWLEDGEMENTS

I would like to acknowledge and extend my greatest gratitude to my Father, God, for the strength, knowledge and guidance He has given me to be able to achieve such a paramount goal in my life. It is because of You that I am where I am today. You have allowed trials and tribulations to come my way for Your glory, to show others that no matter what, they can make it. I have become resilient because of the tests You've allowed for me to go through. Though man and the death of loved ones could have negatively affected me through this journey, You were there to carry, comfort and keep me. You allowed me to rise above it all and for this, I am sincerely and humbly grateful! Thank You and I Love You!!!

I would like to acknowledge and thank my research advisor, Dr. Dawn A. Lott and my committee members, Dr. Matthew Tanzy, Dr. Charles J. Prestigiacomo, Dr. Jinjie Liu and Dr. Fengshan Liu. With their help, guidance, useful input and comments, the process of completing my research and dissertation was a success.

Thank you to the Office of Graduate Studies who financially supported me through a great portion of my graduate studies.

To each and every one of my loved ones who helped, encouraged, and prayed for me along this long journey, I would like to say Thank You! God placed each one of you in my life for such a time as this and I am grateful to each of you for the seen and unseen things that you have done.

A Qualitative Simulation of Blood Flow Through an Elastic Cerebral Saccular Aneurysm Using an Immersed Boundary Method

Brielle C.'L. Sutton

Research Advisor: Dr. Dawn A. Lott

ABSTRACT

Fluid dynamics has been used to simulate blood flow through major arteries of the human body (e.g. aorta and carotid) for advancement of medical technology. This dissertation is directed towards blood flow through a saccular aneurysm attached to a cerebral artery and the effects that the velocity and force of the blood flow have on the aneurysm wall. The two-dimensional nonlinear incompressible Navier-Stokes equations are solved on a staggered Eulerian grid to determine the flow of blood through the artery and aneurysm. An immersed boundary method is utilized to enforce solid boundaries. Subsequently, these nonlinear equations are coupled with the dynamic equation for the motion of an elastic body using an implicit second-order finite-difference scheme on a Lagrangian grid. An efficient and effective numerical program is created that simulates blood flow through a moving artery and its adjoining aneurysm.

TABLE OF CONTENTS

LIST OF FIGURES AND ILLUSTRATIONS . . . . . **vii**
CHAPTER 1 INTRODUCTION AND LITERATURE REVIEW **1**
CHAPTER 2 FLOW WITH A STATIONARY IMMERSED BOUNDARY **16**
2.1 Laminar flow through a cylinder around a stationary circular solid 16
2.1.1 Problem Formulation 16
2.1.2 Methodology 19
2.1.2.1 Algorithm I 20
2.1.3 Defining the Immersed Boundary 23
2.1.4 Determination of Imposed Forces 24
2.1.4.1 Treatment of Nonlinear Terms 24
2.1.4.2 Computation of Laplacian Matrices 25
2.1.4.3 Treatment of Explicit Viscosity Terms 26
2.1.4.4 Computation of Pressure 27
2.1.4.5 Computation of the Force 27
2.1.4.6 Linear Interpolation 30
2.1.5 Nonlinear Terms 34
2.1.6 Implicit Viscosity Terms 34
2.1.7 Computation of Pressure 35
2.1.8 Results 36
2.2 Laminar flow through a rigid cerebral artery with an adjoining rigid saccular aneurysm 41
2.2.1 Problem Formulation 41
2.2.2 Methodology 42
2.2.3 Results 44
2.3 Pulsatile flow through a rigid cerebral artery with an adjoining rigid saccular aneurysm 48
2.3.1 Problem Formulation 48
2.3.2 Methodology 49
2.3.3 Results 50
CHAPTER 3 FLOW WITHIN A DEFORMABLE IMMERSED BOUNDARY **54**
3.1 Problem Formulation 54
3.2 Methodology 55
3.2.1 Eulerian and Lagrangian Grid 55
3.2.2 Numerical Algorithms 59
3.2.2.1 Algorithm II 59
3.2.2.2 Algorithm III 62
3.2.3 Imposed Forces 64
3.2.4 Nonlinear, Viscosity, and Pressure Terms 66
3.2.5 Mass Source/Sink 67

3.2.6 Pseudo-Pressure, Final Velocities, and Updated Pressure 68
3.2.7 Hydrodynamic Force 70
3.2.7.1 Algorithm IV 71
3.2.8 Dynamic Motion Equation Using Finite Difference Methods 71
3.2.8.1 Algorithm V 74
3.2.9 Lagrangian Grid Reconstruction and Transformation 75
3.2.10 Eulerian Velocities of Solid Body After Movement 78
CHAPTER 4 NUMERICAL RESULTS **82**
CHAPTER 5 CONCLUSION **98**
CHAPTER 6 FUTURE WORK **101**
REFERENCES **103**

LIST OF FIGURES AND ILLUSTRATIONS

2.1 The four domain boundaries with imposed no-slip boundary conditions at $z = 0$ and $z = L_z$. 18

2.2 Flow Chart for Flow Around a Rigid Body 22

2.3 Defining the boundary with all points and redefining the boundary with only two points in each cell, one for the U velocity direction (red points) and one for the V velocity direction (blue points). 23

2.4 (a) The original flow domain Λ is enclosed by Ω and solid body surface R_B and (b) the submerged solid is replaced by the same fluid Λ' with proper forces being applied on R_B. 27

2.5 Illustration of the imposed force positions 28

2.6 Illustration of special case for the imposed force positions 29

2.7 Illustration of the force being imposed from the left side of the boundary. . 30

2.8 Illustration of the force being imposed from the right side of the boundary. 31

2.9 Illustration of the force being imposed from the top of the boundary. . . . 32

2.10 Illustration of the force being imposed from the bottom of the boundary. . 33

2.11 (a) U and (b) V velocity profile of laminar flow at $t = 5 \times 10^{-4}$ s. 37

2.12 (a) U and (b) V velocity profile at $t = 5 \times 10^{-3}$ s. 37

2.13 (a) U and (b) V velocity profile at $t = 0.01$ s. 38

2.14 (a) U and (b) V velocity profile at $t = 0.03$ s. 38

2.15 (a) U and (b) V velocity profile at $t = 0.05$ s. 39

2.16 (a) U and (b) V velocity profile at $t = 0.1$ s. 39

2.17 (a) U and (b) V velocity profile at $t = 0.25$ s. 40

2.18 (a) U and (b) V velocity profile at $t = 0.5$ s. 40

2.19 (a) U and (b) V velocity profile at $t = 1.5$ s. 40

2.20 (a) U and (b) V velocity profile at $t = 4$ s. 41

2.21 Illustration of the u_W boundary condition and inflow at the opening of the artery. 42

2.22 Illustration of thickness of boundary with fluid approach 43

2.23 (a) U and (b) V velocity profiles at $t = 5 \times 10^{-4}$ s. 44

2.24 (a) U and (b) V velocity profile at $t = 0.1$ s. 45

2.25 (a) U and (b) V velocity profile at $t = 0.3$ s. 45

2.26 (a) U and (b) V velocity profile at $t = 0.5$ s. 46

2.27 (a) U and (b) V velocity profile at $t = 0.7$ s. 46

2.28 (a) U and (b) V velocity profile at $t = 1$ s. 47

2.29 (a) U and (b) V velocity profile at $t = 1.2$ s. 47

2.30 (a) U and (b) V velocity profile at $t = 1.5$ s. 47

2.31 (a) U and (b) V velocity profile at $t = 1.7$ s. 48

2.32 (a) U and (b) V velocity profile at $t = 2$ s. 48

2.33 Inlet velocity profile of blood flow through artery, $u_{\max}$. 49

2.34 (a) U and (b) V velocity profile at $t = \Delta t$ s, $u_{\max} \approx 1.2073 \times 10^{-1}$ m/s . . 50

2.35 (a) U and (b) V velocity profile at $t = 0.1$ s, $u_{\max} \approx 4.1587 \times 10^{-1}$ m/s . . 50

2.36 (a) U and (b) V velocity profile at $t = 0.3$ s, $u_{\max} \approx 6.8165 \times 10^{-1}$ m/s . . 51

2.37 (a) U and (b) V velocity profile at $t = 0.5$ s, $u_{\max} \approx 5.3618 \times 10^{-2}$ m/s . . 51

2.38 (a) U and (b) V velocity profile at $t = 0.7$ s, $u_{\max} \approx 1.9438 \times 10^{-1}$ m/s . . 52

2.39 (a) U and (b) V velocity profile at $t = 1$ s, $u_{\max} \approx 1.2009 \times 10^{-1}$ m/s . . . 52

2.40 (a) U and (b) V velocity profile at $t = 1.2$ s, $u_{\max} \approx 7.8563 \times 10^{-1}$ m/s . . 52

2.41 (a) U and (b) V velocity profile at $t = 1.7$ s, $u_{\max} \approx 1.9438 \times 10^{-1}$ m/s . . 53

2.42 (a) U and (b) V velocity profile at $t = 2$ s, $u_{\max} \approx 1.2009 \times 10^{-1}$ m/s . . . 53

3.1 Elastic Body 56

3.2 Flow Chart for a Deformable Body 64

3.3 Mass Source/Sink 67

3.4 Illustration of Finite Difference Methods used to calculate the partial derivatives of the center points with respect to s_1. 72

3.5 Illustration of Finite Difference Methods used to calculate the partial derivatives of the center points with respect to s_2. 73

3.6 Mapping between physical and logical space. 75

3.7 Lagrangian center and grid points at the n^{th} level (thin lines and dashed circles) overlapped by the Lagrangian center and grid points at the $(n+1)^{th}$ level (bold lines and solid circles). 77

3.8 Illustration of points needed to define U_P and V_P. 79

4.1 (a) U and (b) V velocity profile at $t = 0.25$ s, $u_{\max} \approx 7.7537 \times 10^{-1}$ m/s . . 82

4.2 (a) U and (b) V velocity profile at $t = 0.5$ s, $u_{\max} = 5.3618 \times 10^{-2}$ m/s . . 83

4.3 (a) U and (b) V velocity profile at $t = 0.75$ s, $u_{\max} \approx 1.6758 \times 10^{-1}$ m/s . . 83

4.4 (a) U and (b) V velocity profile at $t = 1$ s, $u_{\max} \approx 1.2009 \times 10^{-1}$ m/s . . . 84

4.5 (a) U and (b) V velocity profile at $t = 1.3$ s, $u_{\max} \approx 7.7537 \times 10^{-1}$ m/s . . 84

4.6 (a) U and (b) V velocity profile at $t = 1.5$ s, $u_{\max} \approx 5.3612 \times 10^{-2}$ m/s . . 84

4.7 (a) U and (b) V velocity profile at $t = 1.8$ s, $u_{\max} \approx 1.6758 \times 10^{-1}$ m/s . . 85

4.8 (a) U and (b) V velocity profile at $t = 2$ s, $u_{\max} \approx 1.2009 \times 10^{-1}$ m/s . . . 85

4.9 (a) U and (b) V velocity profile at $t = 2.05$ s, $u_{\max} \approx 2.3163 \times 10^{-1}$ m/s . . 86

4.10 (a) U and (b) V velocity profile at $t = 2.1$ s, $u_{\max} \approx 4.1587 \times 10^{-1}$ m/s . . 86

4.11 The aneurysm at $t = 2$ s (red lines) versus $t = 2.1$ s (blue lines, not quite visible). 87

4.12 (a) The proximal and (b) distal side of the aneurysm at $t = 2$ s (red lines) versus $t = 2.1$ s (blue lines, not quite visible). 87

4.13 (a) U and (b) V velocity profile at $t = 2.2$ s, $u_{\max} \approx 7.8563 \times 10^{-1}$ m/s . . 88

4.14 (a) The proximal and (b) distal side of the aneurysm at $t = 2$ s (red lines) versus $t = 2.2$ s (blue lines). 88

4.15 (a) The proximal and (b) distal side of the ostium (neck) at $t = 2$ s (red lines) versus $t = 2.2$ s (blue lines). 88

4.16 (a) U and (b) V velocity profile at $t = 2.3$ s, $u_{\max} \approx 6.8165 \times 10^{-1}$ m/s . . 89

4.17 (a) U and (b) V velocity profile at $t = 2.4$ s, $u_{\max} \approx 2.5242 \times 10^{-1}$ m/s . . 89

4.18 (a) U and (b) V velocity profile at $t = 2.5$ s, $u_{\max} \approx 5.3618 \times 10^{-2}$ m/s . . 90

4.19 (a) Magnification of proximal region of the aneurysm at $t = 2.5$ s 90

4.20 The aneurysm at $t = 2$ s (red lines) versus $t = 2.5$ s (blue lines). 91

4.21 Magnification of (a) the proximal side of the ostium (neck); (b) the distal side of the ostium (neck); (c) the middle region of the bottom of artery at $t = 2$ s. 91

4.22 Magnification of (a) the top of the aneurysm; (b) the proximal side of the aneurysm; (c) the distal side of the aneurysm at $t = 2$ s. 92

4.23 (a) U and (b) V velocity profile at $t = 2.6$ s, $u_{\max} \approx 1.0828 \times 10^{-1}$ m/s . . 92

4.24 (a) U and (b) V velocity profile at $t = 2.7$ s, $u_{\max} \approx 1.9438 \times 10^{-1}$ m/s . . 93

4.25 The aneurysm at $t = 2$ s (red lines) versus $t = 2.7$ s (blue lines). 93

4.26 (a) The proximal and (b) distal side of the ostium leading up to the aneurysm at $t = 2$ s (red lines) versus $t = 2.7$ s (blue lines). 94

4.27 (a) The proximal side of the top artery wall leading up to the ostium and (b) the distal side of the ostium leading down to the artery wall at $t = 2$ s (red lines) versus $t = 2.7$ s (blue lines). 94

4.28 (a) U and (b) V velocity profile at $t = 2.8$ s, $u_{\max} \approx 1.1657 \times 10^{-1}$ m/s . . 95

4.29 (a) U and (b) V velocity profile at $t = 2.9$ s, $u_{\max} \approx 7.4527 \times 10^{-2}$ m/s . . 95

4.30 (a) U and (b) V velocity profile at $t = 3$ s, $u_{\max} \approx 1.2009 \times 10^{-1}$ m/s . . . 95

4.31 The aneurysm at $t = 2$ s (red lines) versus $t = 3$ s (blue lines). 96

4.32 (a) The proximal side of the top artery wall leading up to the ostium,(b) the distal side of the ostium leading down to the artery wall and (c) the middle region of the bottom of artery at $t = 2$ s (red lines) versus $t = 3$ s (blue lines). 96

Chapter 1

INTRODUCTION AND LITERATURE REVIEW

In the past years, researchers have studied fluid mechanics in conjunction with the biomedical field. More specifically, fluid dynamics has been used to simulate blood flow through major arteries of the human body (e.g. aorta and carotid) for advancement of medical technology. This dissertation is directed towards blood flow through a saccular aneurysm attached to a cerebral artery and the effects that the velocity and force of the blood flow have on the aneurysm wall. An efficient and effective numerical code is developed and simulated. Use of this code and future development of these algorithms will enable others to determine the best way to treat a saccular aneurysm.

There are three different treatment methods for aneurysms in-vivo; that is, endovascular coiling, coiling in conjunction with ballooning or stenting, and clipping. Within the last two years, there has been the introduction of "flow diversion" [5] in the setting of treating aneurysms endovascularly. The difference between the coiling, etc., and the flow diversion is that flow diversion depends on placing an object (usually a stent) within the vessel itself which then modifies the flow around the neck of the aneurysm, slows the flow down as blood enters the aneurysm, and further slows its egress from the aneurysm. This results in thrombosis (clotting) of the aneurysm. Another potential mechanism, which has been fully substantiated, is that it "deflects" flow away from the aneurysm and this results in a change in flow dynamics and ultimately stagnation and thrombosis.

A cerebrovascular neurosurgeon specializes in surgical clipping, and an interventional neuro-radiologist/endovascular surgeon specializes in the less invasive treatment of cerebral aneurysms by coiling and/or flow diversion. During neurosurgery, the neurosurgeon places a surgical clip around the aneurysm's neck. The clip seals off the aneurysm so that blood cannot enter, causing thrombosis. During the endovascular procedure, a small tube (catheter)

is directed through the blood vessel into the aneurysm itself. Then, using X-ray guidance, the surgeon carefully places soft platinum micro-coils into the aneurysm and detaches them. The coils stay inside the aneurysm and act as a mechanical barrier to the blood flow reducing the blood's velocity, which promotes thrombosis, thus sealing off the aneurysm. [10]

Most methods for determining the aneurysm characteristics require intracranial intrusion. There are methods for aneurysm treatment that are non-invasive such as mathematical predictions for aneurysm treatment. This research may help to determine the morphology of an aneurysm and thus, its propensity to rupture, by using information regarding the fluid mechanics of blood, the elasticity properties of blood vessels, and mechanical properties of fluid-solid interactions.

The method used will be an aid in predicting how aneurysms may be best treated using the various endovascular treatments in-silico instead of proceeding with an invasive procedure. Another important outcome of this methodology is that one might be able to use this technique to also help predict which aneurysms are at a very high risk of rupture and thus, expose only those patients with a high rupture risk to the risk of treatment.

Morales et al. proposed a virtual coiling technique for treating image-based aneurysm models. They used a dynamic path planning to mimic the structure and distribution of coils inside aneurysm cavities and to reach high packing densities which was desirable by clinicians when treating with coils. Several tests were done to evaluate the performance on idealized and image-based aneurysm models. The proposed technique was validated using clinical information of real coiled aneurysms. The virtual coiling technique reproduced the macroscopic behavior of inserted coils and properly captured the densities, shapes, and coil distributions inside aneurysm cavities. [29]

A practical application was performed by assessing the local hemodynamics, after coiling, using computational fluid dynamics (CFD). Wall shear stress and intra-aneurysmal

velocities were reduced after coiling. Additionally, CFD simulations showed that coils decreased the amount of contrast entering the aneurysm and increased its residence time. [29]

Tremmel et al. presented a study using computational fluid dynamics to quantifying the effect of single and multiple self-expanding Enterprise stents alone or in combination with balloon-mounted stents on aneurysm hemodynamics. They used computed tomographic angiography images to reconstruct the geometry of a wide-necked, saccular, and basilar trunk aneurysm. One to three stents were virtually placed inside the aneurysm and they calculated the hemodynamic parameters after this placement. Their results showed that the complex aneurysmal flow pattern was suppressed by stenting. [40]

Jeong and Rhee studied initiation, progress, and rupture of cerebral aneurysms. They also analyzed results of flow after coiling and stenting of an aneurysm [15]. Wu et al. also studied the effects of placing a stent inside of an intracranial aneurysm [49]. Ventikos et al. evaluated the rupture risk, the thrombogenic characteristics of specific lesions and the efficacy assessment of endovascular coil embolisation and flow diversion using stents [46].

Recent studies have demonstrated that by placing a stent with a high mesh density (low porosity) in the parent vessel across the aneurysm's neck, the flow of blood into the aneurysm can be sufficiently modified to promote thrombosis within the aneurysm itself.

Meuschke et al. presented the first visualization tool that combined patient-specific hemodynamics with information about the vessel wall deformation and wall thickness in cerebral aneurysms. They investigated the morphological and hemodynamic data of patient-specific cerebral aneurysms. They used a linked 2.5-dimensional and 3-dimensional depiction of the aneurysm together with blood flow information that enabled the simultaneous exploration of wall characteristics and hemodynamic attributes during the cardiac cycle. They developed a GPU-based (graphics processing unit) implementation of their visualizations with a flexible interactive data exploration mechanism. They designed their techniques in collaboration with domain experts, and provide details about the evaluation. [27]

Lott et al. developed a virtual two-dimensional flow model replicating an in vitro aneurysm model to analyze how changes in morphology modified flow characteristics. They concluded that the data suggested that neck and proximal dome configuration, independent of size, were important characteristics of flow. [24]

Mikhal wrote a thesis which focused on the role of computational fluid dynamics for identifying and classifying therapeutic options in the treatment of aneurysms. The contribution made was computing the precise patient-specific pulsatile flow in all spatial and temporal details, using an immersed boundary method (IBM). Computations of the flow inside the aneurysm to predict high and low stress regions, indicative of possible growth of an aneurysm, were done. Visualization of vortical structures in the flow indicating the quality of local blood circulation were done. Mikhal showed that as the size of the aneurysm increased, qualitative changes in the flow behavior arose. [28]

Bazilevs et al. [3], Endres et al. [8], Jiang et al. [16], Karmonik et al. [18], Marzo et al. [26], Oubel et al. [31], Paál et al. [32], Sugiyama et al. [37], Tateshima et al. [38], Torii et al. [39], Valen-Sendstad et al. [42], and Wong et al. [48] studied the hemodynamics of an intracranial aneurysm using computational fluid dynamics. These authors studied fluid-structure interaction, took into consideration the wall shear and tension stresses of the aneurysm, examined the motion of the wall as blood moved through the aneurysm including the outer forces on the aneurysm wall, and they examined the morphology of the aneurysm. Though slightly different methods and subjects were used to be successful in their studies, they all had the same idea in studying the hemodynamics of intracranial aneurysms.

Valencia et al. carried out eight computational structural dynamics simulations, one computational fluid dynamics simulation, and four fluid-structure interaction simulations in an anatomically realistic model of a saccular cerebral aneurysm with the objective of quantifying the effects of type of simulation on principal fluid and solid mechanics results. The results allowed the study of the influence of the type of material elements in the solid, the

aneurysm's wall thickness, and the type of simulation on the modeling of a human cerebral aneurysm. [43]

Arthurs et al. developed a two-dimensional model of arteriolar fluid flow and mass transport. The model included a phenomenological representation of the myogenic response of the arteriolar wall, in which an increase in perfusion pressure stimulated vasoconstriction. The model also included the release, advection, diffusion, degradation, and dilatory action of nitric oxide, a potent, but short-lived, vasodilatory agent. Parameters for the model were taken primarily from the experimental literature of the rat renal afferent arteriole. Solutions to the incompressible Navier-Stokes (N-S) equations were approximated by means of a splitting technique that used upwind differencing for the inertial term and a spectral method for the viscous term and incompressibility condition. The immersed boundary method was used to include the forces arising from the arteriolar walls. The advection of nitric oxide was computed by means of a high-order flux-corrected transport scheme; the diffusion of nitric oxide was computed by a spectral solver. [1]

Simulations demonstrated the efficacy of the numerical methods employed, and grid refinement studies confirmed anticipated first-order temporal convergence and demonstrated second-order spatial convergence in key quantities. By providing information about the effective width of the immersed boundary and sheer stress magnitude near that boundary, the grid refinement studies indicated the degree of spatial refinement required for quantitatively reliable simulations. Owing to the dominating effect of nitric oxide advection, relative to degradation and diffusion, simulations indicated that nitric oxide had the capacity to produce dilation along the entire length of the arteriole. [1]

Valencia and Solis described the flow dynamics and arterial wall interaction in a representative model of a terminal aneurysm of the basilar artery, and they compared its wall shear stress, pressure, effective stress, and wall deformation with those of a healthy basilar artery. The arterial wall was assumed to be elastic (or hyper-elastic), isotropic, incompressible, and

homogeneous. The flow was assumed to be laminar, Newtonian, and incompressible. The incompressible Navier-Stokes equations with arbitrary Lagrangian-Eulerian (ALE) formulation were used as the governing equations which were suitable for problems with fluid structure interaction and frequent mesh adjustments. [44]

The intra-aneurysmal pulsatile flow showed single recirculation region during both systole and diastole. The pressure and shear stress on the aneurysm wall exhibited large temporal and spatial variations. The wall thickness, the Youngs modulus in the elastic wall model, and the hyper-elastic Mooney–Rivlin wall model affected the aneurysm deformation and effective stress in the wall especially at systole. [44]

Jones compared varying middle cerebral artery (MCA) bifurcation angles to uncover any changes to fluid flow and wall shear stress that could simulate aneurysm growth. Eight pre-aneurysm MCA bifurcation models were created. The laminar fluid flow module was used on these models to simulate non-Newtonian blood flow. Fluid flow profiles showed little to no change between the models. [17]

Rossitti investigated whether the branching geometry determined an underlying increase of shear stress on the vessel wall in cerebral arteries of patients with aneurysms located distally to the circle of Willis. The ratio between shear stress in the branches and shear stress in the parent vessel at bifurcations was estimated using exponential relations of vessel caliber. Cerebral angiograms of 10 patients with an aneurysm of the distal anterior cerebral artery were analyzed and compared with normal values from an earlier study. The branching geometry determined a relatively small but significant increase on shear stress in branches and of shear stress gradients at bifurcation apices on cerebral arteries of patients with an aneurysm. [33] Jansen et al. compared intracranial aneurysm hemodynamics based on generalized versus patient-specific inflow boundary conditions. Geometric models of aneurysms were determined for 36 patients by using 3D rotational angiography. Two-dimensional phase contrast MR imaging velocity measurements of the parent artery were performed. Compu-

tational fluid dynamics simulations were performed twice. Resulting mean and maximum wall shear stress and oscillatory shear index values were analyzed, and hemodynamic characteristics were qualitatively compared. [14]

A non-uniform rational B-splines (NURBS)-based isogeometric fluid–structure interaction formulation, coupling incompressible fluids with non-linear elastic solids, and allowing for large structural displacements, was developed by Bazilevs et al. Their methodology, encompassing a very general class of applications, was applied to problems of arterial blood flow modeling and simulation. A set of procedures enabling the construction of analysis-suitable NURBS geometries directly from patient-specific imaging data was outlined. The approach was compared with representative benchmark problems, yielding very good results. Computation of a patient-specific abdominal aorta was also performed, giving qualitative agreement with computations by other researchers using similar models. [2]

Isaksen et al. aimed to develop a computational model for simulation of fluid-structure interaction in cerebral aneurysms based on patient specific lesion geometry, with special emphasis on wall tension. They developed an advanced isogeometric fluid-structure analysis model incorporating a flexible aneurysm wall based on patient specific computed tomography angiogram images. The simulation results exposed areas of high wall tension and wall displacement located where aneurysms usually rupture. [13]

Carallo et al. investigated the relationships between shear stress and circumferential wall tension and between these hemodynamic factors and the intima-media thickness (IMT) of the common carotid artery in healthy men. Fifty-eight subjects were studied. Shear stress was calculated as blood viscosity×blood velocity/internal diameter. Circumferential wall tension was calculated as blood pressure×internal radius. Blood velocity, internal diameter, and IMT were measured by a high-resolution echo-Doppler. Their findings confirmed that common carotid shear stress varied among healthy individuals and decreased as age, blood pressure, and body mass index (BMI) increased. Their findings also demonstrated that circumferential

wall tension was directly associated with wall thickness, age, and BMI and that shear stress was associated with common carotid IMT independent of other hemodynamic, clinical, or biochemical factors. [6]

Lind et al. investigated if a reduced shear stress was also related to the echolucency of plaque and the intima-media complex. A population-based study of 1016 subjects aged 70 were studied in the Prospective Study of the Vasculature in Uppsala Seniors (PIVUS) study. The left common carotid artery diameter, IMT, the grey scale median (GSM) of the intima-media complex (IM-GSM), and the blood flow velocity were measured, for each subject, by ultrasound. They found that a low shear stress in the common carotid artery was associated with both a thick IMT and an echolucent intima-media complex. [23]

Yang and Stern presented a direct forcing immersed boundary framework for the simple and efficient simulation of strongly coupled fluid–structure interactions. The immersed boundary method developed by Yang and Balaras was greatly simplified by eliminating several complicated geometric procedures without sacrificing the overall accuracy. The fluid–structure coupling scheme of Yang et al. was also significantly expedited by moving the fluid solver out of the predictor–corrector iterative loop without altering the strong coupling property. [52]

They reformulated the field extension strategy and the evaluation of fluid force and moment exerted on the immersed bodies, by taking advantage of the direct forcing idea in a fractional-step method. Several cases with prescribed motions were examined first to validate the simplified field extension approach. Then, a variety of strongly coupled fluidstructure interaction problems, including vortex induced vibrations of a circular cylinder, transverse and rotational galloping of rectangular bodies, and fluttering and tumbling of rectangular plates, were computed. The excellent agreement between the present results and the reference data from experiments and other simulations demonstrated the accuracy,

simplicity, and efficiency of the new method and its applicability in a wide range of complicated fluid-structure interaction problems. [52]

Wang and Eldredge presented a strong coupling algorithm for simulating the dynamic interactions between incompressible viscous flows and rigid-body systems in both two-and three-dimensional problems. In this work, the Navier–Stokes equations for incompressible flow were solved on a uniform Cartesian grid by the vorticity-based immersed boundary projection method of Colonius and Taira. Dynamical equations for arbitrary rigid-body systems were also developed. The proposed coupling method attempted to unify the treatment of constraints in the fluid and structure (the incompressibility of the fluid), the linkages in the rigid-body system, and the conditions at the interface (through the use of Lagrange multipliers). [47]

The resulting partitioned system of equations was solved with a simple relaxation scheme, based on an identification of virtual inertia from the fluid. The scheme achieved convergence in only two to five iterations per time step for a wide variety of mass ratios. The formulation required that only a subset of the discrete fluid equations be solved in each iteration. Several two-and three-dimensional numerical tests were conducted to validate and demonstrate the method, including a falling cylinder, flapping of flexible wings, self-excited oscillations of a system of many linked plates in a free stream, and passive pivoting of a finite aspect ratio plate under the influence of gravity in a free stream. The results from the current method were compared with previous experimental and numerical results and good agreement was achieved. [47]

Di and Ge improved and implemented Uhlmanns direct-forcing IBM on a supercomputer with CPU–GPU (central processing unit-graphics processing unit) hybrid architecture. The direct-forcing IBM was modified by solving the Poissons equation for pressure before evaluation of the body force, and the force was only distributed to the Cartesian grids inside the immersed boundary. A multi direct forcing scheme was used to evaluate the body force.

These modifications resulted in a divergence-free flow field in the fluid domain and the no-slip boundary condition at the immersed boundary simultaneously. [7]

Di and Ge's method was implemented in an explicit finite-difference fractional-step scheme, and was validated by two-dimensional simulations of lid-driven cavity flow, Couette flow between two concentric cylinders, and flow over a circular cylinder. The method was used to simulate the sedimentation of two circular particles in a channel. The results agreed very well with previous experimental and numerical data, and were more accurate than the conventional direct-forcing method, especially in the vicinity of a moving boundary. [7]

In 1981, Hirt and Nichols described a simple, but powerful, method that was based on the concept of a fractional volume of fluid (VOF). To illustrate the method, a description was given for an incompressible hydrodynamics code, SOLA-VOF (solution algorithm-volume of fluid), which used the VOF technique to track free fluid surfaces. [11]

Kim, J. et al. developed a new immersed-boundary method for simulating flows over or inside complex geometries by introducing a mass source/sink as well as a momentum forcing. A stable second-order interpolation scheme for evaluating the momentum forcing on the body surface or inside the body was also proposed. [19]

Shen and Chan later developed a combined immersed boundary and volume of fluid (VOF) methodology to simulate the interactions of free-surface waves and submerge solid bodies. They used the immersed boundary method to account for the no-slip boundary condition at solid interfaces and the VOF method to track free surfaces. The Navier-Stokes equations were used to capture the essential features of the flow-structure interactions. [35] Xu and Wang implemented the immersed interface method to incorporate the jump conditions, previously derived for simulating incompressible viscous flows subject to moving boundaries in 3D with second-order spatial and temporal accuracy near the boundaries, in a two-dimensional numerical scheme. They studied the accuracy, efficiency, and robustness of their method by simulating Taylor–Couette flow, flow induced by a relaxing balloon, flow

past single and multiple cylinders, and flow around a flapping wing. Their results showed that their code had second-order accuracy in the infinity norm for both the velocity and the pressure; the addition of an object introduced relatively insignificant computational cost; and the method was equally effective in computing flow subject to boundaries with prescribed force or boundaries with prescribed motion. [51]

Udaykumar et al. presented a Cartesian grid method for computing flows with complex immersed and moving boundaries. A mixed Eulerian-Lagrangian framework was used which allowed them to treat the immersed moving boundary as a sharp interface. They discretized the incompressible Navier-Stokes equations using a second-order-accurate finite-volume technique. They also used a second-order accurate fractional-step scheme for time advancement. Their methodology was validated by comparing it to the experimental data on two cases, the flow in a channel with a moving indentation on one wall, and vortex shedding from a cylinder oscillating in a uniform free-stream. [41]

Vanella et al. developed a structured adaptive mesh refinement (S-AMR) strategy for fluid–structure interaction problems in laminar and turbulent incompressible flows. The computational grid consisted of a number of nested grid blocks at different refinement levels. The filtered Navier–Stokes equations for incompressible flow were advanced in time using an explicit second-order projection scheme, where all spatial derivatives were approximated using second-order central differences on a staggered grid. For transitional and turbulent flow regimes, the large-eddy simulation (LES) approach was used, where special attention was paid on the discontinuities introduced by the local refinement. [45]

For all the fluid-structure interaction problems reported in their study, the complete set of equations governing the dynamics of the flow and the structure were simultaneously advanced in time using a predictor corrector strategy. An embedded-boundary method was utilized to enforce the boundary conditions on a complex moving body which was not aligned

with the grid lines. Several examples of increasing complexity were given to demonstrate the robustness and accuracy of their proposed formulation. [45]

Huang and Sung proposed an immersed boundary method for simulation of fluid-flexible structure interaction. They used an efficient Navier-Stokes solver, adopting the fractional step method, and a staggered Cartesian grid system to solve the incompressible fluid motion in an Eulerian domain. They also used a moving Lagrangian grid to discretize the structure domain [12].

Le et al. presented an implicit immersed boundary method for the incompressible Navier-Stokes equation which was capable of handling three-dimensional membrane-fluid flow interactions. Their goal was to greatly improve the time step by using the Jacobian-free Newton-Krylov method (JFNK) to advance to location of the elastic membrane implicitly [20]. Li et al. used an immersed boundary method to track the morphology of an animal cell membrane during cytokinesis. They performed numerical simulations on the axisymmetric domain to have sufficient resolution and incorporated three-dimensional effects [22].

Shishir et al. investigated the dynamics of blood flow in saccular cerebral aneurysms. They computationally analyzed the flow field by the three-dimensional Navier-Stokes equations for laminar flow of incompressible Newtonian fluid. This study was done for a rigid vascular wall where different sizes of circular and elliptical necks was studied. Results showed that the geometrical parameter of the aneurysm caused variations with the vortex location, inflow area in the neck, and other aspects of the solid body. [36]

Xenos studied the blood flow in an aneurysm by developing a method that would track the moving tissue and account for its interaction with the fluid. A mixed Euler-Lagrangian formulation was used to study blood flow in the aneurysm during the cardiac cycle. A coupled and nonlinear system of partial differential equations made up the motion equation and were discretized using the finite volume method. Results showed that the pulsating wall greatly influenced the flow velocity, Reynolds and Womersley numbers increased as

pulsatility increased, and the wall shear stress was amplified at the shoulders of the moving wall compared to that of the rigid wall. [50]

Similar methods are used in this research as done in [50]. The difference is that Xenos used the finite volume method to discretize the system of nonlinear partial differential equations. In this research, a finite difference method is used for discretization of such system.

Mori and Peskin recognized that the immersed boundary method is a computational framework for problems involving the interaction of fluid and immersed elastic structures, and immersed boundary computations typically evaluate the elastic forces explicitly in the configuration of the immersed elastic structure. As a result, they concluded that, in many applications, these aspects result in a severe restriction on the time step. Hence, they presented a semi-implicit and a fully implicit second-order accurate immersed boundary method. The methods provided a natural way to handle mass on the immersed elastic structures. They demonstrated the performance for a prototypical fluid-structure interaction problem. The methods were shown to possess superior stability properties that significantly alleviate the typically severe time step restriction of explicit computations. [30]

Seibold created a compact and fast code to solve the incompressible Navier-Stokes equations on a rectangular domain. It contained fundamental components such as discretization on a staggered grid, an implicit viscosity step, a projection step, and the visualization of the solution over time [34]. This code serves as the foundation for this research.

Lee and Choi presented an immersed boundary method for the simulation of flow around an elastic slender body. Their method was based on the discrete-forcing immersed boundary method for a stationary, rigid body proposed by Kim, J. et al. They implicitly coupled the incompressible Navier-Stokes equations with the dynamic equation for an elastic slender body motion. Eulerian and Lagrangian coordinates were used to accomplish this fluid-structure interaction. [21]

Ghaffari et al. presented an efficient algorithm for simulation of deformable bodies interacting with two-dimensional incompressible fluid flows. The temporal and spatial discretizations of the NavierStokes equations in vorticity stream-function formulation were based on classical fourth-order RungeKutta scheme and compact finite differences, respectively. Using a uniform Cartesian grid, they benefited from the advantage of a new fourth-order direct solver for the Poisson equation to ensure the incompressibility constraint down to machine zero over an optimal grid. For introducing a deformable body in fluid flow, the volume penalization method was used. [9]

A Lagrangian structured grid with prescribed motion covered the deformable body which was interacting with the surrounding fluid due to the hydrodynamic forces and the torque calculated on the Eulerian reference grid. An efficient law for controlling the curvature of an anguilli-form fish, swimming toward a prescribed goal, was proposed which was based on the geometrically exact theory of nonlinear beams and quaternions. Validation of the developed method showed the efficiency and expected accuracy of the algorithm for fish-like swimming and also for a variety of fluid–solid interaction problems. [9]

This dissertation is a unique, novel combination work of the methods used by Mori and Peskin, Seibold, Lee and Choi, and Ghaffari et al. to create fluid-structure interaction using a finite-difference, immersed boundary method to simulate blood flow through a cerebral artery and its adjoining saccular aneurysm. A semi-implicit numerical code solving the two-dimensional nonlinear incompressible Navier-Stokes equations is created [34] and simulations of laminar and pulsatile blood flow through the rigid cerebral artery and its adjoining aneurysm are simulated in Chapter 2. This benchmark problem is tested for accuracy and stability and is the framework for Chapter 3.

In Chapter 3, the two-dimensional Navier-Stokes equations are coupled with the equation of motion for an elastic body [21] to simulate fluid flow through a deformable vessel and adjoining aneurysm. The numerical method, in Chapter 2, is modified to incorporate a fluid-

solid algorithm and a deformable immersed boundary for the simulation of blood–aneurysm vessel interaction.

The Navier-Stokes equations, discretized on a staggered Eulerian grid, is coupled with a semi-implicit, second-order finite-difference scheme (Crank-Nicolson) on a Lagrangian grid. Numerical results depicting aneurysm and vessel movement in response to fluid flow are presented in Chapter 4. The discussion and conclusion are presented in Chapter 5. This dissertation concludes with Chapter 6, Future Work.

Chapter 2

FLOW WITH A STATIONARY IMMERSED BOUNDARY

2.1 Laminar flow through a cylinder around a stationary circular solid

2.1.1 Problem Formulation

Accurate, stable, and consistent results for the problems presented in this dissertation are obtained by first developing a fluid-solid numerical code [34] that simulates laminar flow in a right, circular cylinder around a rigid circular solid. This problem is the benchmark example and is utilized for code development and verification. The flow of an incompressible fluid is governed by the two-dimensional incompressible Navier-Stokes equations. In vector form, the Navier-Stokes equations are,

$$\frac{\partial \boldsymbol{u}}{\partial t} = -\boldsymbol{u} \cdot \nabla \boldsymbol{u} + \frac{1}{Re} \nabla^2 \boldsymbol{u} - \nabla p + \boldsymbol{f}, \tag{2.1}$$

where $\boldsymbol{u} = (U, V)^\top$ are the fluid velocities, Re is the Reynolds number, p is the pressure, and $\boldsymbol{f}$ is the momentum force. Along with the Navier-Stokes equations is the continuity equation in vector form,

$$\nabla \cdot \boldsymbol{u} = 0, \tag{2.2}$$

which enforces time-dependent pressure. Equations (2.1) and (2.2) are formulated as a system of nonlinear equations as follows,

$$U_t = -(U^2)_x - (UV)_z + \frac{1}{Re}(U_{xx} + U_{zz}) - P_x + F_U, \tag{2.3}$$

$$V_t = -(UV)_x - (V^2)_z + \frac{1}{Re}(V_{xx} + V_{zz}) - P_z + F_V, \tag{2.4}$$

$$U_x + V_z = 0. \tag{2.5}$$

Here, U and V are the fluid velocity vectors in the x and z directions, respectively; t is the time variable, x and z are the spatial variables, P_x and P_z are the derivatives of the pressure in the x and z directions, respectively; F_U and F_V are the momentum forcing components defined at the cell faces on or inside the immersed boundary to satisfy the no-slip boundary condition on the immersed boundary. Re,

$$Re = \frac{\rho \, u_{\max} \, L_z}{\mu}, \tag{2.6}$$

is the Reynolds number, ρ is the fluid density, μ is the dynamic viscosity of the fluid, $u_{\max}$ is the maximum velocity of the fluid flow (characteristic velocity), and L_z is the length of the domain in the z direction. All time is in *seconds* and length is scaled to *meters*.

The above incompressible Navier-Stokes equations are solved in the Eulerian coordinate system on a rectangular domain $\Omega = [0, L_x] \times [0, L_z]$ which is fixed in time where L_x is the length of the domain in the x direction and L_z is as above [34]. The time step, Δt, is chosen based on the grid size to insure stability of the numerical code. A fixed grid of dimension $n_x \times n_z$, where n_x and n_z denote the number of cells in the x and z directions, respectively [34], is defined when the length $[0, L_x]$ is partitioned into n_x cells and the width $[0, L_z]$ is partitioned into n_z cells. Hence, the dimension of one grid cell is $h_x \times h_z$ where,

$$h_x = \frac{L_x}{n_x}, \qquad h_z = \frac{L_z}{n_z}. \tag{2.7}$$

The velocities, U and V, and the pressure, P, are initialized as zero matrices in there respective dimensions.

A staggered grid is used for stability purposes [34] where U (red dots) and V (blue dots) are placed on the vertical and horizontal cell interfaces, respectively, and the pressure, P (black dots), is placed in the center of each cell interface (See figure 2.1). For the staggered

grid, the U and V velocities are defined with the interior resolution of the U velocity equal to $(n_x - 1) \times n_z$ and the interior resolution of the V velocity equal to $n_x \times (n_z - 1)$.

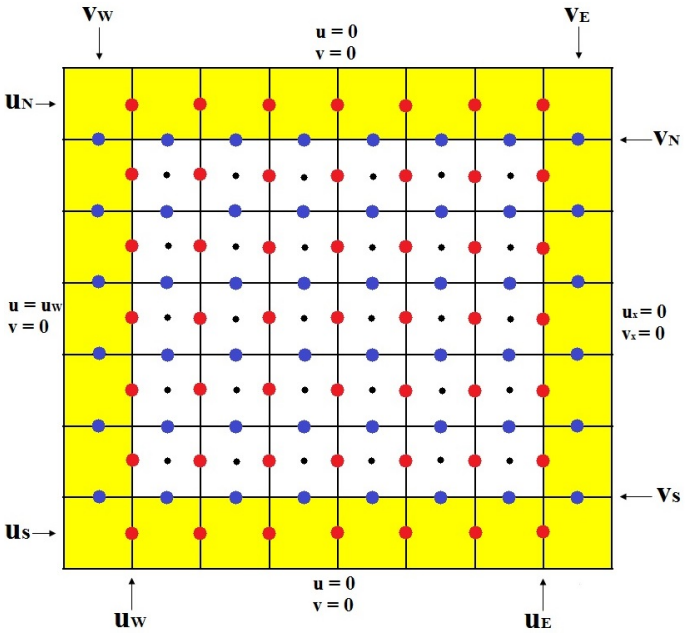

Figure 2.1: The four domain boundaries with imposed no-slip boundary conditions at $z = 0$ and $z = L_z$.

In figure 2.1, the four domain boundaries are denoted as North, South, East, and West. The no-slip boundary conditions are imposed on the North and South boundaries as follows [34],

$$u(x, L_z) = u_N(x) = 0 \tag{2.8}$$

$$v(x, L_z) = v_N(x) = 0 \tag{2.9}$$

$$u(x, 0) = u_S(x) = 0 \tag{2.10}$$

$$v(x, 0) = v_S(x) = 0. \tag{2.11}$$

The Dirichlet boundary conditions imposed on the West boundary are,

$$u(0,z) = u_W(z) \tag{2.12}$$

$$v(0,z) = v_W(z) = 0, \tag{2.13}$$

and the Neumann boundary conditions imposed on the East boundary are,

$$u_x(L_x,z) = 0 \tag{2.14}$$

$$v_x(L_x,z) = 0. \tag{2.15}$$

Notice that all of the boundary conditions are set equal to zero except the West boundary for the U velocity vector, u_W. This is done to simulate laminar flow, i.e. fluid flowing in from the West boundary. Fluid is free to flow out of the East boundary by setting the velocity derivatives equal to zero. The West boundary condition, u_W, is parabolic and dependent upon the maximum velocity of the fluid, $u_{\max}$, the height of the domain, L_z, and z where,

$$u_W = \frac{4u_{\max}}{L_z^2}\, z(L_z - z). \tag{2.16}$$

As a result of this derivation, the u_W boundary condition simulates laminar (Poiseuille) flow through the West domain.

2.1.2 Methodology

The two-dimensional incompressible Navier-Stokes equations are discretized in time and space and are solved numerically. The computational steps used to solve the two-dimensional incompressible Navier-Stokes equations, modeling laminar flow in a cylinder around a rigid circular solid, are described in Algorithm I.

2.1.2.1 Algorithm I

1. Initialization:

   (a) Flag cells as solid, fluid, or boundary cells.

   (b) For each boundary cell, determine the fluid approach direction to be used in computing the force on the boundary.

   (c) Initialize computational variables U, V, and P.

   (d) Define inlet velocity of fluid for u_W.

2. Begin computation at $t = n\,\Delta t$, for $n = 1$ and continue for $n = 2, ..., NT$, where NT is the maximum number of iterations.

3. Compute the terms to be used in calculating the imposed forces on the rigid solid:

   (a) Compute the preliminary nonlinear terms $\mathcal{N}(\boldsymbol{u}^n)$,

$$\mathcal{N}(U^n) = \left((U^n)^2\right)_x + \left(U^n V^n\right)_z , \tag{2.17}$$

$$\mathcal{N}(V^n) = \left(U^n V^n\right)_x + \left((V^n)^2\right)_z . \tag{2.18}$$

   (b) Compute the preliminary viscosity terms $\mathcal{L}(\boldsymbol{u}^n)$ explicitly,

$$\mathcal{L}(U^n) = \frac{1}{Re}\left(U^n_{xx} + U^n_{zz}\right), \tag{2.19}$$

$$\mathcal{L}(V^n) = \frac{1}{Re}\left(V^n_{xx} + V^n_{zz}\right). \tag{2.20}$$

   (c) Compute the gradient of the pressure, ∇P^n,

$$\nabla P^n = \left\langle \left(P^n\right)_x, \left(P^n\right)_z \right\rangle . \tag{2.21}$$

(d) Compute the imposed forces F_U^{n+1} and F_V^{n+1},

$$F_U^{n+1} = \frac{\tilde{U}^n - U^n}{\Delta t} + (P^n)_x + \mathcal{N}(U^n) - \mathcal{L}(U^n), \tag{2.22}$$

$$F_V^{n+1} = \frac{\tilde{V}^n - V^n}{\Delta t} + (P^n)_z + \mathcal{N}(V^n) - \mathcal{L}(V^n), \tag{2.23}$$

where $\tilde{U}^n$ and $\tilde{V}^n$ are the velocities that are interpolated to enforce the velocities at the boundary to be zero.

4. Compute the intermediate velocities $\boldsymbol{u}^\diamond$, $\boldsymbol{u}^{\diamond\diamond}$, and $\boldsymbol{u}^{\diamond\diamond\diamond}$:

(a) Update $\boldsymbol{u}^\diamond$ by forcing terms,

$$U^\diamond = U^n + \Delta t\ F_U^{n+1}, \tag{2.24}$$

$$V^\diamond = V^n + \Delta t\ F_V^{n+1}. \tag{2.25}$$

(b) Update $\boldsymbol{u}^{\diamond\diamond}$ by nonlinear terms,

$$U^{\diamond\diamond} = U^\diamond - \Delta t \left[\left((U^n)^2 \right)_x + (U^n V^n)_z \right], \tag{2.26}$$

$$V^{\diamond\diamond} = V^\diamond - \Delta t \left[(U^n V^n)_x + \left((V^n)^2 \right)_z \right]. \tag{2.27}$$

(c) Update $\boldsymbol{u}^{\diamond\diamond\diamond}$ by computing viscosity terms implicitly,

$$U^{\diamond\diamond\diamond} = U^{\diamond\diamond} + \frac{\Delta t}{Re} \left(U_{xx}^{\diamond\diamond\diamond} + U_{zz}^{\diamond\diamond\diamond} \right), \tag{2.28}$$

$$V^{\diamond\diamond\diamond} = V^{\diamond\diamond} + \frac{\Delta t}{Re} \left(V_{xx}^{\diamond\diamond\diamond} + V_{zz}^{\diamond\diamond\diamond} \right). \tag{2.29}$$

5. Compute the pressure by solving the Poisson equation followed by computing the gradient of the pressure yielding the final velocities $\boldsymbol{u}^{n+1}$,

$$U^{n+1} = U^{\diamond\diamond\diamond} - \Delta t \left(P^{n+1}\right)_x, \tag{2.30}$$

$$V^{n+1} = V^{\diamond\diamond\diamond} - \Delta t \left(P^{n+1}\right)_z. \tag{2.31}$$

6. Update $t = (n+1)\Delta t$.

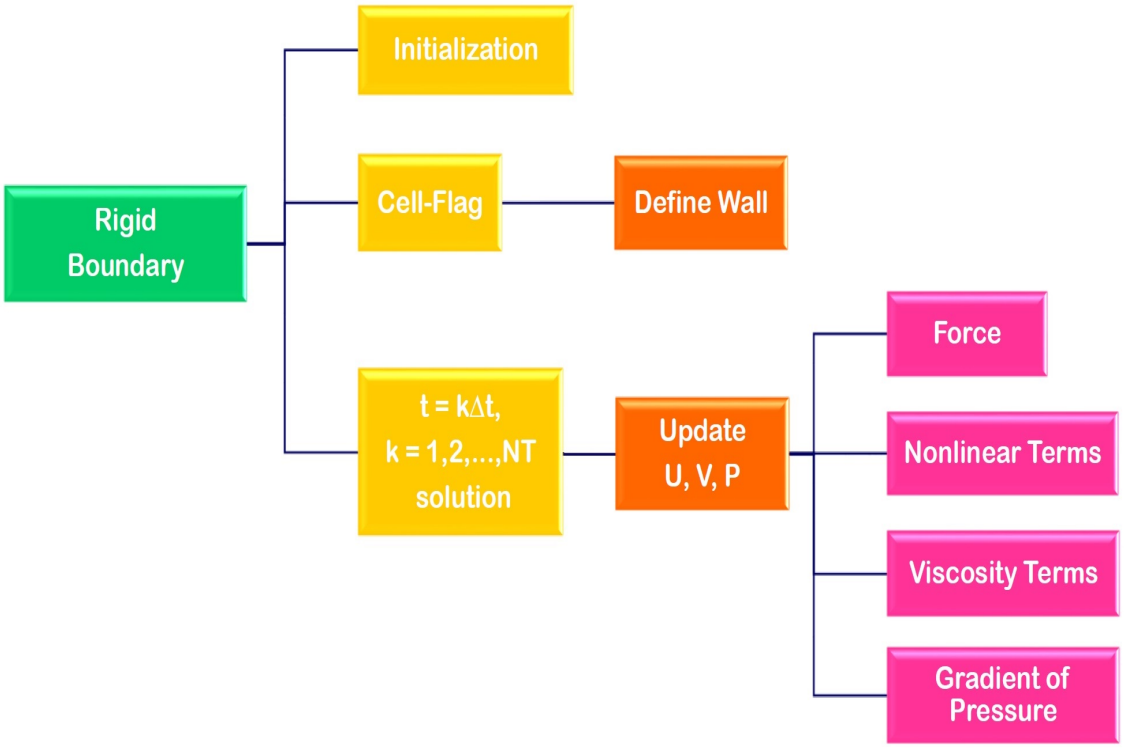

Figure 2.2: Flow Chart for Flow Around a Rigid Body

2.1.3 Defining the Immersed Boundary

The immersed boundary is defined as a circle of radius r_0 with center (x_0, z_0) where,

$$x = r_0 \cos(\theta) + x_0 \tag{2.32}$$

$$z = -r_0 \sin(\theta) + z_0. \tag{2.33}$$

The maximum number of points defining the boundary are chosen to ensure there is at least one point in each of the Eulerian boundary cells (See figure 2.3).

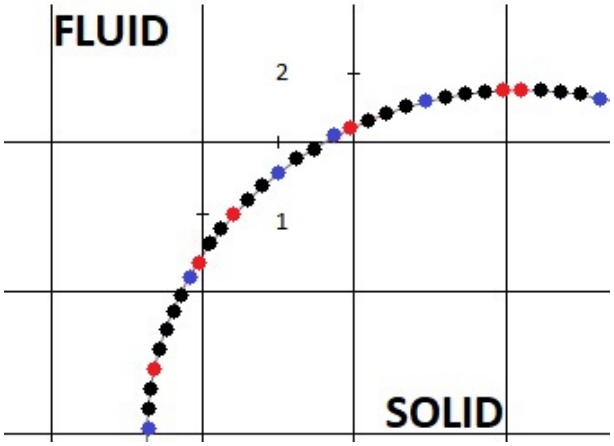

Figure 2.3: Defining the boundary with all points and redefining the boundary with only two points in each cell, one for the U velocity direction (red points) and one for the V velocity direction (blue points).

From the many points that are created to define the boundary, only two points are chosen in each cell, one for the U velocity direction, defined as $B_U(x, z)$ and one for the V velocity direction, defined as $B_V(x, z)$. It is possible for one point to be used for both velocity directions. Where only one point is needed in order to flag the cell as a boundary cell, the two points are needed to effectively compute the imposed forces that will be described in Section 2.1.4. There are two cases to consider before minimizing the number of points in each Eulerian boundary cell.

1. A point in the boundary cell lines up with a discrete vertical and/or horizontal velocity. In figure 2.3, in cell *1*, the red and blue dots represent the points that are used to define forces on this cell which contribute to the discrete horizontal and vertical velocities for this cell, respectively.

2. A point in the boundary cell does not line up with a discrete vertical and/or horizontal velocity. In figure 2.3, in cell *2*, the points closest to the discrete vertical (blue dot) and horizontal (red dot) velocities are used.

The cells that contain these boundary points are flagged as fluid-solid cells. The cells that are completely inside the solid are flagged as solid cells, and the cells that are completely in the fluid are flagged as fluid cells. Cell-flagging aids in determining the location of the fluid with respect to the boundary.

2.1.4 Determination of Imposed Forces

2.1.4.1 Treatment of Nonlinear Terms

The first step in Algorithm I is to compute the forcing terms. This is done by computing the nonlinear terms at time $t = t^n$. To compute these terms, the right side of equations 2.17 and 2.18 must be solved,

$$\mathcal{N}(U^n) = \left((U^n)^2\right)_x + (U^n V^n)_z \,, \tag{2.34}$$

$$\mathcal{N}(V^n) = (U^n V^n)_x + \left((V^n)^2\right)_z \,. \tag{2.35}$$

In order to treat these terms, the U and V matrices are extended to include their respective boundary points (i.e., the North, South, East, and West boundaries). Next, $(UV)_x$ and $(UV)_z$ are computed by averaging and differentiating the extended U velocity vertically and the extended V velocity horizontally and by using γ, the transition parameter [34] yielding,

$$UV_x = \frac{\partial(U_a V_a - \gamma |U_a| V_d)}{\partial x}, \tag{2.36}$$

$$UV_z = \frac{\partial((U_a V_a - \gamma U_d |V_a|)^T)^T}{\partial z}. \tag{2.37}$$

Here, U_a, V_a, U_d, and V_d are the averages of U and V and the derivatives of U and V, respectively. The parameter, γ, is used to implement a smooth transition between centered differencing and up-winding.

$$\gamma = min\left(1.2\Delta t\ max\left(\frac{max\,(max\,|U|)}{h_x}, \frac{max\,(max\,|V|)}{h_z}\right), 1\right). \tag{2.38}$$

Gamma is the maximum fraction of cells for which information can travel in one time step, multiplied by 1.2 and capped at 1 [34].

Next, $(U^2)_x$ and $(V^2)_z$ are computed by averaging and differentiating the extended U velocity horizontally and the extended V velocity vertically and by using γ to get [34],

$$\left(U^2\right)_x = \frac{\partial(U_a^2 - \gamma |U_a| U_d)}{\partial x}, \tag{2.39}$$

$$\left(V^2\right)_z = \frac{\partial((V_a^2 - \gamma |V_a| V_d)^T)^T}{\partial z}. \tag{2.40}$$

Substituting each part into equations 2.17 and 2.18 yields the nonlinear terms needed to compute the force. The same method is used for computing the nonlinear terms in equations 2.26 and 2.27 when updating the intermediate velocities, $U^{\diamond\diamond}$ and $V^{\diamond\diamond}$.

2.1.4.2 Computation of Laplacian Matrices

Computation of the Laplacian matrices for U, V, and P are needed in order to treat the viscosity terms of velocities U and V and for the pressure field P at each time step.

The Laplace operator with appropriate boundary conditions are discretized in the Laplacian matrices Lu ($\equiv \Delta_U$), Lv ($\equiv \Delta_V$), and Lp ($\equiv \Delta_p$) for U, V, and P, respectively [34].

The Kronecker tensor product is utilized to construct the block matrices in two dimensional space which combines the sparse identity matrix of dimension $(nx \times nx)$ or $(nz \times nz)$ and the tridiagonal matrix, K_1, approximating either $\frac{\partial^2}{\partial x^2}$ or $\frac{\partial^2}{\partial z^2}$, both in one dimensional space [34]. K_1 generates the following matrix,

$$K_1 = \frac{1}{h^2}\begin{bmatrix} -a_{11} & 1 & & & \\ 1 & -2 & 1 & & \\ & \ddots & \ddots & \ddots & \\ & & 1 & -2 & 1 \\ & & & 1 & -b_{11} \end{bmatrix} \tag{2.41}$$

where a_{11} and b_{11} denote the boundary condition parameters.

Before creating the system matrices, Lu, Lv, and Lp, the boundary conditions for U, V, and P have to be determined in terms of either Neumann, Dirichlet (for points on the boundary), or mid-Dirichlet (for boundary between two points) boundaries with parameters denoted as 1, 2, or 3, respectively. A second-order central-differencing scheme is used to determine the boundary conditions for the U and V velocities. For this scheme, U requires both Neumann and Dirichlet boundary conditions in the x direction and the mid-Dirichlet boundary condition in the z direction; V requires both Neumann and mid-Dirichlet boundary conditions in the x direction and the Dirichlet boundary condition in the z direction. Neumann boundary conditions are prescribed for P [34].

2.1.4.3 Treatment of Explicit Viscosity Terms

After computing the Laplacian matrices, the explicit viscosity terms of equations 2.19 and 2.20 can be determined. Multiplication of the Laplacian matrices, Lu and Lv, by the

velocities, U^n and V^n, yield the explicit computation of the viscosity terms, equations 2.19 and 2.20. The modified Laplacian equations for U^n and V^n are,

$$\Delta U^n = \frac{1}{Re}\left(\frac{\partial^2}{\partial x^2}+\frac{\partial^2}{\partial z^2}\right)U^n, \tag{2.42}$$

$$\Delta V^n = \frac{1}{Re}\left(\frac{\partial^2}{\partial x^2}+\frac{\partial^2}{\partial z^2}\right)V^n. \tag{2.43}$$

2.1.4.4 Computation of Pressure

The gradient of the pressure field is needed at the n^{th} level to compute the force (equation 2.21),

$$\nabla P^n = \langle (P^n)_x , (P^n)_z \rangle . \tag{2.44}$$

2.1.4.5 Computation of the Force

The immersed boundary method used consists of replacing an actual solid body with the force being imposed on the body surface (See figure 2.4.) [35].

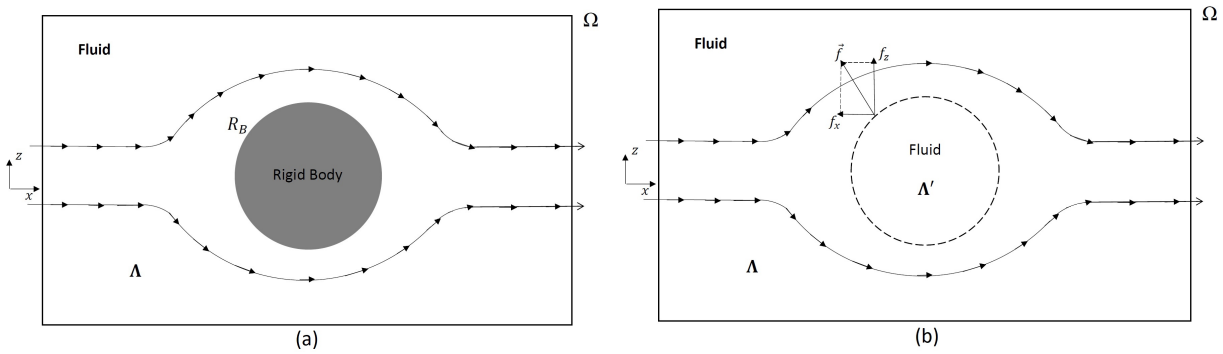

Figure 2.4: (a) The original flow domain Λ is enclosed by Ω and solid body surface R_B and (b) the submerged solid is replaced by the same fluid Λ' with proper forces being applied on R_B.

The forces are applied before the intermediate velocities are computed and they satisfy the no-slip boundary conditions on the immersed boundary. Recall equations 2.22 and 2.23,

$$F_U^{n+1} = \frac{\tilde{U}^n - U^n}{\Delta t} + (P^n)_x + \mathcal{N}(U^n) - \mathcal{L}(U^n), \tag{2.45}$$

$$F_V^{n+1} = \frac{\tilde{V}^n - V^n}{\Delta t} + (P^n)_z + \mathcal{N}(V^n) - \mathcal{L}(V^n). \tag{2.46}$$

Since the forces are imposed on the solid boundary, the imposed forcing components have to be shifted to the associated positions nearest to the solid boundary [35].

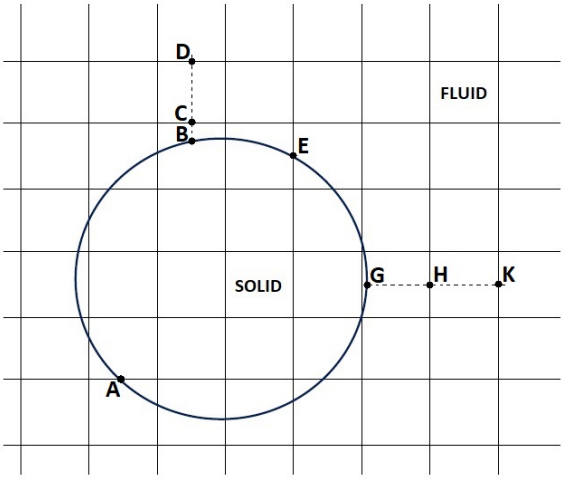

Figure 2.5: Illustration of the imposed force positions

There are three cases that must be considered when computing the imposed force on each boundary cell. Figure 2.5 illustrates the two most frequently occurring cases.

1. The discrete vertical or horizontal velocity is located at a point on the immersed boundary. At point A, there is a vertical velocity, and at point E, there is a horizontal velocity. Note that there can be a case where there is both a horizontal and vertical velocity in any given cell. The imposed force in the x direction for point E is numerically determined by equation 2.22 with $\tilde{U}^n = \tilde{U}_E$ where $\tilde{U}_E$ is the x-component velocity of the boundary. The same method is used for point A in the vertical direction where $\tilde{V}^n = \tilde{V}_A$ in equation 2.23.

2. A discrete vertical or horizontal velocity is not located at a point on the immersed boundary. In figure 2.5, point B does not coincide with a discrete vertical velocity, and point G does not coincide with a discrete horizontal velocity. In this case, the associated force term will be calculated at the nearest position to the boundary [35]. Thus, for point C, in the vertical direction, the z-component force imposed at this point is computed using equation 2.23 with $\tilde{V}^n = \tilde{V}_C$ where linear interpolation is used to determine the velocity $\tilde{V}_C$ using velocities V_B and V_D. For point H, in the horizontal direction, the x-component force imposed at this point is determined using equation 2.22 with $\tilde{U}^n = \tilde{U}_H$ where linear interpolation is used to determine the velocity $\tilde{U}_H$ using velocities U_G and U_K.

3. Figure 2.6 illustrates the special case where a cell has an interpolated velocity in the z direction but not in the x direction and vice versus. Since we must have a velocity in both directions for each cell, we choose a discrete vertical or horizontal velocity closest to the boundary point defined for that cell and we use that velocity in computing the imposed force for that boundary cell.

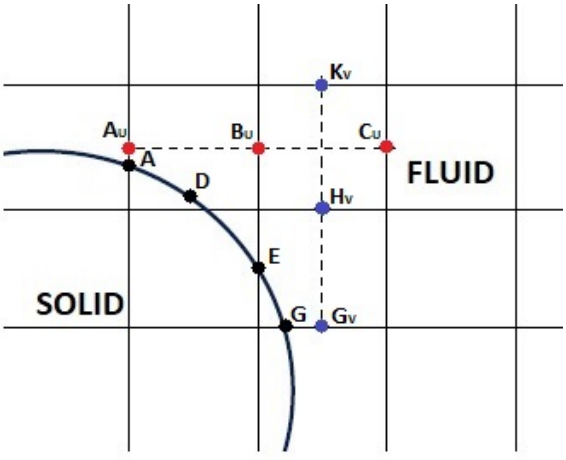

Figure 2.6: Illustration of special case for the imposed force positions

For example, we let A_U be the discrete horizontal velocity closest to point A. Then the points A_U and C_U are used to do linear interpolation to find the velocity at B_U. Similar steps are taken for determining the velocity at H_V in the vertical direction using G_V and K_V. Hence, the imposed force in the x direction for point B_U is numerically determined by equation 2.22 with $\tilde{U}^n = \tilde{U}_{B_U}$ where linear interpolation is used to determine the velocity $\tilde{U}_{B_U}$ using A_U and C_U. The same method is used for point H_V in the vertical direction.

2.1.4.6 Linear Interpolation

The numerical code determines the direction in which the fluid is approaching the boundary of each cell and this information is used when linearly interpolating a velocity. There are four directions in which the fluid can approach the boundary.

- Left Approach:

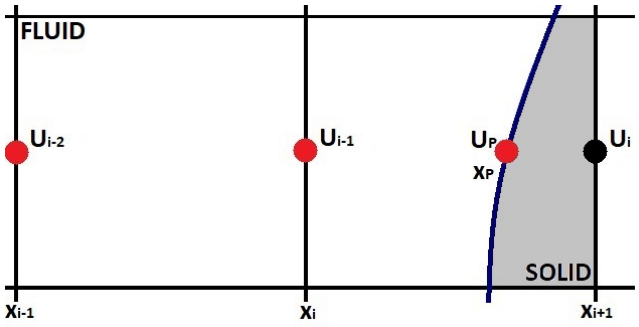

Figure 2.7: Illustration of the force being imposed from the left side of the boundary.

In figure 2.7, the velocity, $\tilde{U}_{i-1}$, at the x_i location is numerically determined by the following equation,

$$\tilde{U}_{i-1} = \frac{U_{i-2} - U_P}{x_P - x_{i-1}}(x_P - x_i) + U_P, \tag{2.47}$$

where x_P ($\equiv BU(x)$) is the location of the point on the boundary in the horizontal direction and U_P is the velocity at that point. In this case, every point on the immersed

boundary is stationary, i.e., $U_P = 0$. Hence, equation 2.47 simplifies to,

$$\tilde{U}_{i-1} = \frac{x_P - x_i}{x_P - x_{i-1}}(U_{i-2}). \tag{2.48}$$

- Right Approach:

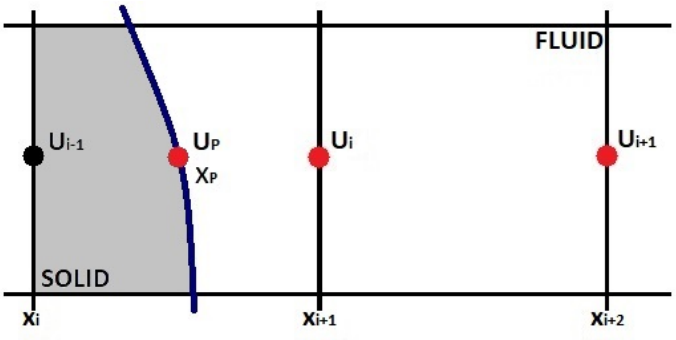

Figure 2.8: Illustration of the force being imposed from the right side of the boundary.

In figure 2.8, the velocity, $\tilde{U}_i$, at the x_{i+1} location is numerically determined by the following equation,

$$\tilde{U}_i = \frac{U_{i+1} - U_P}{x_{i+2} - x_P}(x_{i+1} - x_P) + U_P, \tag{2.49}$$

where x_P and U_P are the same as defined in the left approach example. Since $U_P = 0$ in this case also, equation 2.49 simplifies to,

$$\tilde{U}_i = \frac{x_{i+1} - x_P}{x_{i+2} - x_P}(U_{i+1}). \tag{2.50}$$

- Top Approach:

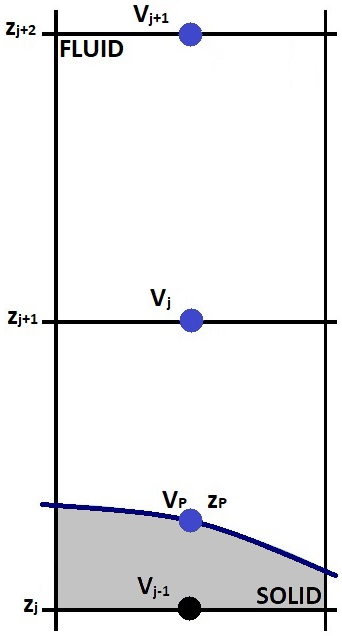

Figure 2.9: Illustration of the force being imposed from the top of the boundary.

In figure 2.9, the velocity, $\tilde{V}_j$, at the z_{j+1} location is numerically determined by the following equation,

$$\tilde{V}_j = \frac{V_{j+1} - V_P}{z_{j+2} - z_P}(z_{j+1} - z_P) + V_P, \tag{2.51}$$

where z_P ($\equiv BV(z)$) is the location of the point on the boundary in the vertical direction and V_P is the velocity at that point. Since $V_P = 0$ due to the rigid boundary, equation 2.51 simplifies to,

$$\tilde{V}_j = \frac{z_{j+1} - z_P}{z_{j+2} - z_P}(V_{j+1}). \tag{2.52}$$

- Bottom Approach:

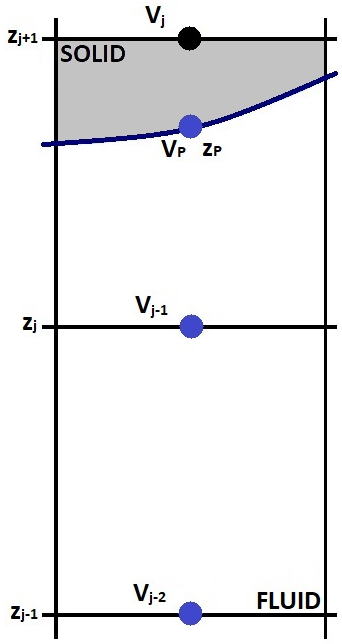

Figure 2.10: Illustration of the force being imposed from the bottom of the boundary.

Lastly, in figure 2.10, the velocity, $\tilde{V}_{j-1}$, at the z_j location is numerically determined by the following equation,

$$\tilde{V}_{j-1} = \frac{V_{j-2} - V_P}{z_P - z_{j-1}}(z_P - z_j) + V_P, \tag{2.53}$$

where z_P and V_P are the same as defined in the top approach example. Since $V_P = 0$ in this case also, equation 2.53 simplifies to,

$$\tilde{V}_{j-1} = \frac{z_P - z_j}{z_P - z_{j-1}}(V_{j-2}). \tag{2.54}$$

Once the velocities, $\tilde{\boldsymbol{u}}$, of the boundary cells are computed at their respective positions, the forces are calculated and used to update the intermediate velocities, $U^\diamond$ and $V^\diamond$, which

yield equations 2.24 and 2.25,

$$U^{\diamond} = U^n + \Delta t \; F_U^{n+1}, \tag{2.55}$$

$$V^{\diamond} = V^n + \Delta t \; F_V^{n+1}. \tag{2.56}$$

2.1.5 Nonlinear Terms

The nonlinear terms computed in Section are used to update $U^{\diamond\diamond}$ and $V^{\diamond\diamond}$ to obtain equations 2.26 and 2.27,

$$U^{\diamond\diamond} = U^{\diamond} - \Delta t \left[\left((U^n)^2 \right)_x + \left(U^n V^n \right)_z \right], \tag{2.57}$$

$$V^{\diamond\diamond} = V^{\diamond} - \Delta t \left[\left(U^n V^n \right)_x + \left((V^n)^2 \right)_z \right]. \tag{2.58}$$

2.1.6 Implicit Viscosity Terms

Cholesky decomposition is used to solve the viscosity terms of equations 2.28 and 2.29 implicitly in order to update the intermediate velocities, $U^{\diamond\diamond\diamond}$ and $V^{\diamond\diamond\diamond}$. Rewriting equations 2.28 and 2.29 yield,

$$U^{\diamond\diamond} = U^{\diamond\diamond\diamond} - \frac{\Delta t}{Re} \left(U_{xx}^{\diamond\diamond\diamond} + U_{zz}^{\diamond\diamond\diamond} \right), \tag{2.59}$$

$$V^{\diamond\diamond} = V^{\diamond\diamond\diamond} - \frac{\Delta t}{Re} \left(V_{xx}^{\diamond\diamond\diamond} + V_{zz}^{\diamond\diamond\diamond} \right). \tag{2.60}$$

Letting,

$$\Delta_U = \left[I - \frac{\Delta t}{Re} \left(\frac{\partial^2}{\partial x^2} + \frac{\partial^2}{\partial z^2} \right) \right], \tag{2.61}$$

$$\Delta_V = \left[I - \frac{\Delta t}{Re} \left(\frac{\partial^2}{\partial x^2} + \frac{\partial^2}{\partial z^2} \right) \right], \tag{2.62}$$

yields,

$$U^{\diamond\diamond} = \Delta_U \left(U^{\diamond\diamond\diamond} \right), \tag{2.63}$$

$$V^{\diamond\diamond} = \Delta_V \left(V^{\diamond\diamond\diamond} \right). \tag{2.64}$$

Taking the Laplacian inverse of both sides of equations 2.63 and 2.64 yields,

$$U^{\diamond\diamond\diamond} = \Delta_U^{-1} \left(U^{\diamond\diamond} \right), \tag{2.65}$$

$$V^{\diamond\diamond\diamond} = \Delta_V^{-1} \left(V^{\diamond\diamond} \right), \tag{2.66}$$

resulting in the updated intermediate velocities, $U^{\diamond\diamond\diamond}$ and $V^{\diamond\diamond\diamond}$, of equations 2.28 and 2.29.

2.1.7 Computation of Pressure

The final velocities are updated by computing the gradient of the pressure at the $(n+1)^{th}$ level. Taking the gradient of the pressure enforces incompressibility by applying the continuity equation.

$$\frac{U^{n+1} - U^{\diamond\diamond\diamond}}{\Delta t} = -\left(P^{n+1} \right)_x \tag{2.67}$$

$$\frac{V^{n+1} - V^{\diamond\diamond\diamond}}{\Delta t} = -\left(P^{n+1} \right)_z. \tag{2.68}$$

Writing equations 2.67 and 2.68 in vector form yields,

$$\frac{1}{\Delta t} \boldsymbol{u}^{n+1} - \frac{1}{\Delta t} \boldsymbol{u}^{\diamond\diamond\diamond} = -\nabla P^{n+1}. \tag{2.69}$$

Applying the gradient to both sides of equation 2.69 and the continuity equation (equation 2.5) yields the Poisson equation (equations 2.30 and 2.31) written in vector form,

$$-\frac{1}{\Delta t}\nabla \cdot \boldsymbol{u}^{\diamond\diamond\diamond} = -\Delta P^{n+1}. \tag{2.70}$$

The Laplacian inverse is applied to both sides of equation 2.70 using Lp from Section 2.1.4.2 to obtain P^{n+1},

$$P^{n+1} = \Delta_p^{-1}\left(\frac{1}{\Delta t}\nabla \boldsymbol{u}^{\diamond\diamond\diamond}\right). \tag{2.71}$$

Note that a simple matrix inverse of the system matrix for the pressure is computed. Cholesky decomposition for the pressure is not used since the system matrix for the pressure is not positive definite.

Applying the divergence to both sides of equation 2.71 and updating the velocity field yields the final velocities (equations 2.30 and 2.31),

$$U^{n+1} = U^{\diamond\diamond\diamond} - \Delta t\left(P^{n+1}\right)_x, \tag{2.72}$$

$$V^{n+1} = V^{\diamond\diamond\diamond} - \Delta t\left(P^{n+1}\right)_z. \tag{2.73}$$

2.1.8 Results

Figures 2.11-2.20 depict the U and V velocity profiles of laminar flow through a cylinder around a rigid circular solid. The following parameters used to run this simulation are: $\rho = 993.3$, $\mu = 6.913 \times 10^{-4}$, $u_{\max} = 1.201 \times 10^{-3}$, $L_x = 1$, $L_z = 8.66 \times 10^{-1}$, $r_0 = 2.165 \times 10^{-1}$, $x_0 = 5 \times 10^{-1}$, $z_0 = 4.33 \times 10^{-1}$, $n_x = 130$, $n_z = 500$, $Re = 1.4944 \times 10^3$, $\Delta x = 7.7 \times 10^{-3}$, $\Delta z = 1.7 \times 10^{-3}$, $\Delta t = 5 \times 10^{-4}$, and $NT = 8000$.

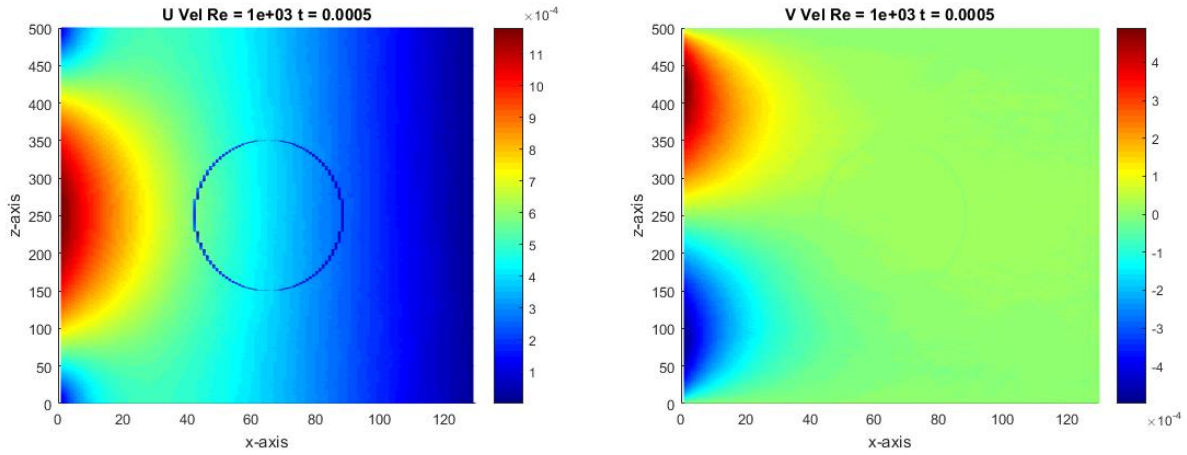

Figure 2.11: (a) U and (b) V velocity profile of laminar flow at $t = 5 \times 10^{-4}$ s.

Figure 2.11 is the initial step of fluid flow as it enters the cylinder from the west boundary. The fluid has an inlet velocity of 1.201×10^{-3} m/s.

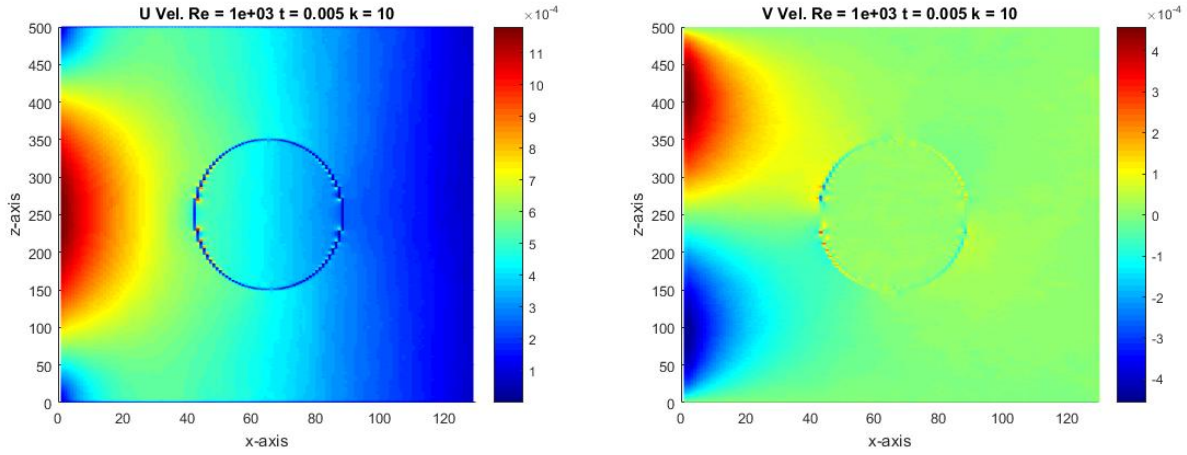

Figure 2.12: (a) U and (b) V velocity profile at $t = 5 \times 10^{-3}$ s.

Figure 2.12 represent the boundary being completely defined and the fluid is being forced to go around the solid region as it approaches it. The fluid "trapped" inside the solid region begins to slow down automatically as the immersed boundary becomes more defined. The light blue region inside the solid darkens representing no movement inside the solid region. Figure 2.12(b) demonstrates the V velocity profile which shows no fluid is entering

or exiting the domain. The red and blue regions are the effects of the U velocity since both velocity profiles are dependent on each other.

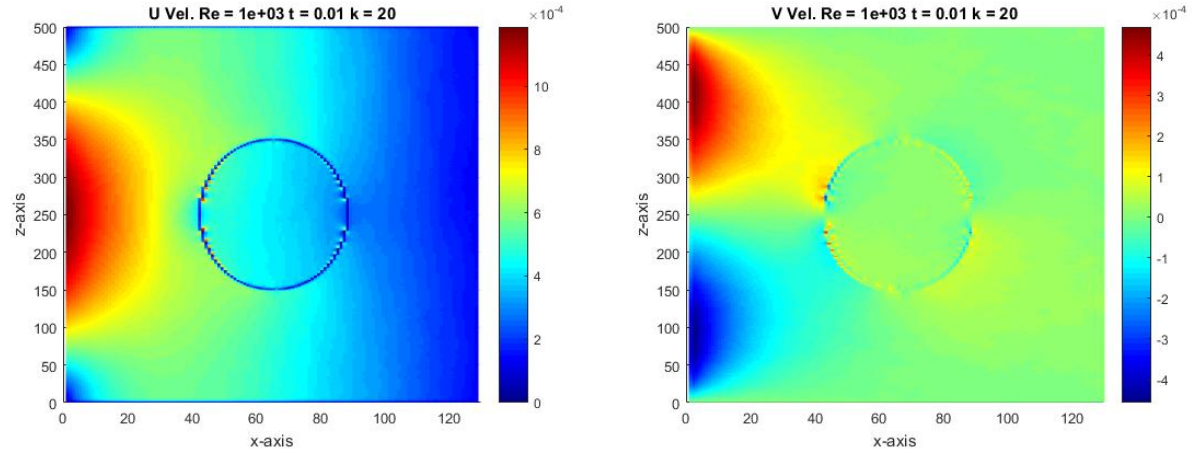

Figure 2.13: (a) U and (b) V velocity profile at $t = 0.01$ s.

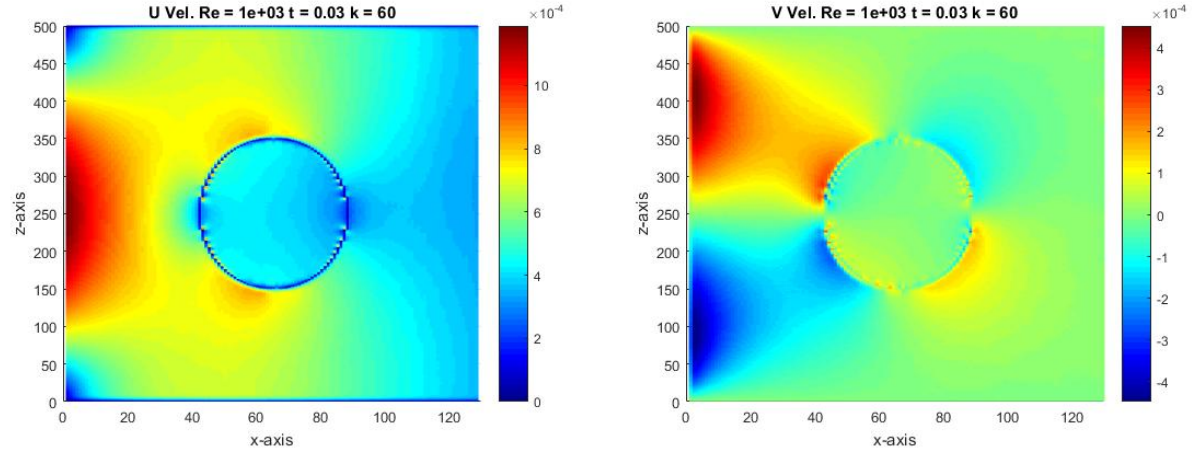

Figure 2.14: (a) U and (b) V velocity profile at $t = 0.03$ s.

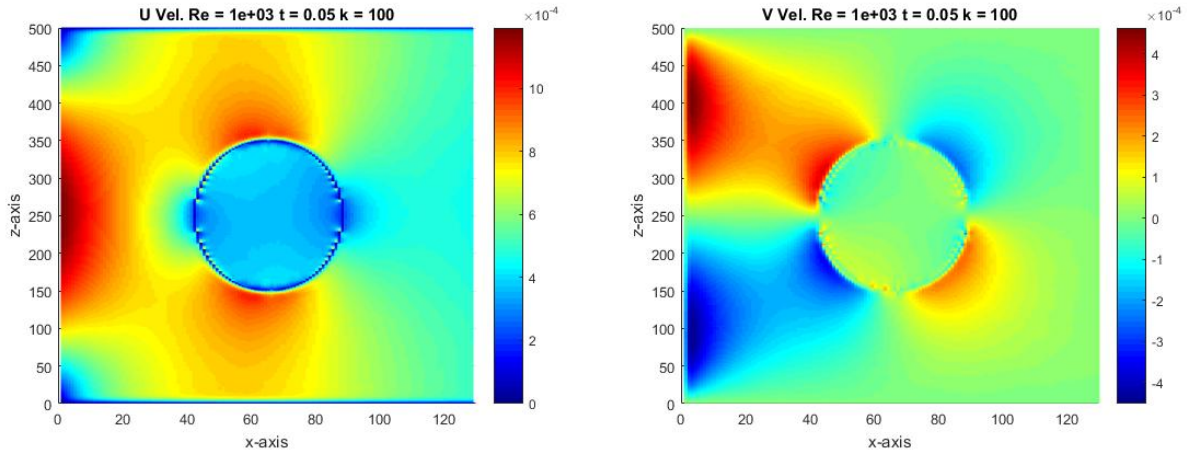

Figure 2.15: (a) U and (b) V velocity profile at $t = 0.05$ s.

As the fluid is forced to go around the immersed solid, it speeds up. This is because the fluid is still entering the fluid domain at the same velocity but now, the fluid has a smaller region that it has to pass through as it passes through the small enclosed area between the circular solid and the cylinder wall. The no-slip boundary conditions causes the fluid to be zero at the wall of the solid and the wall of the cylinder (the dark blue regions). The Neumann boundary conditions at the East boundary allow for the fluid to flow out of the East domain freely.

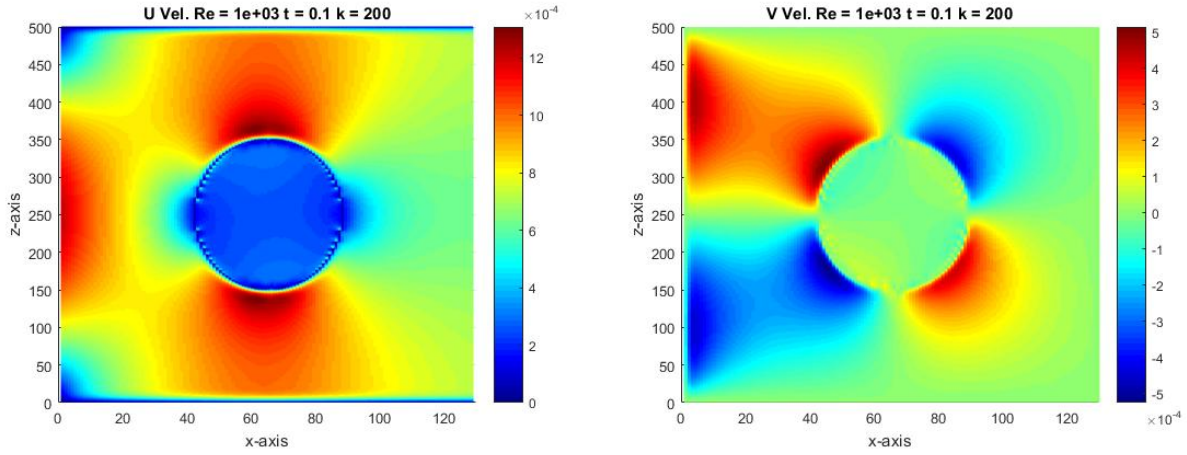

Figure 2.16: (a) U and (b) V velocity profile at $t = 0.1$ s.

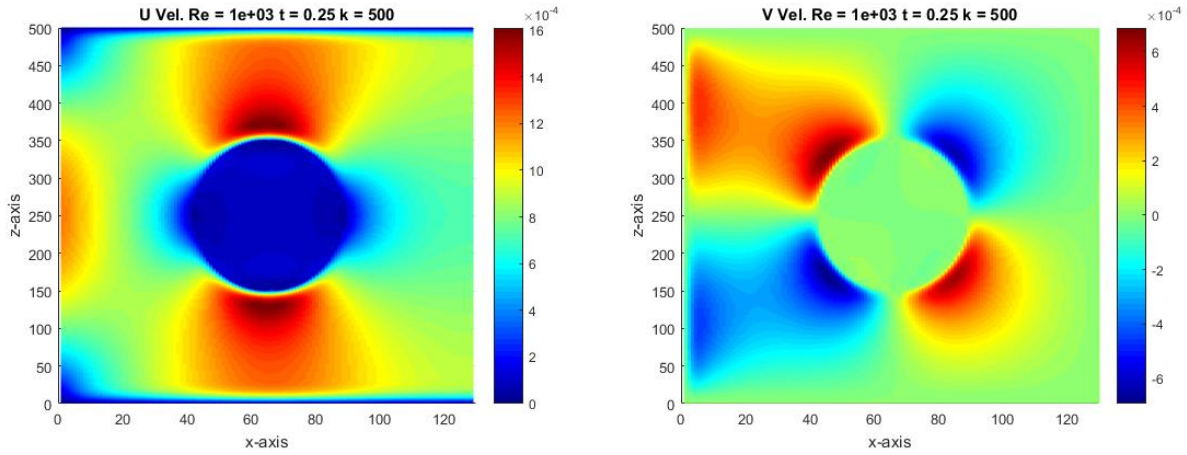

Figure 2.17: (a) U and (b) V velocity profile at $t = 0.25$ s.

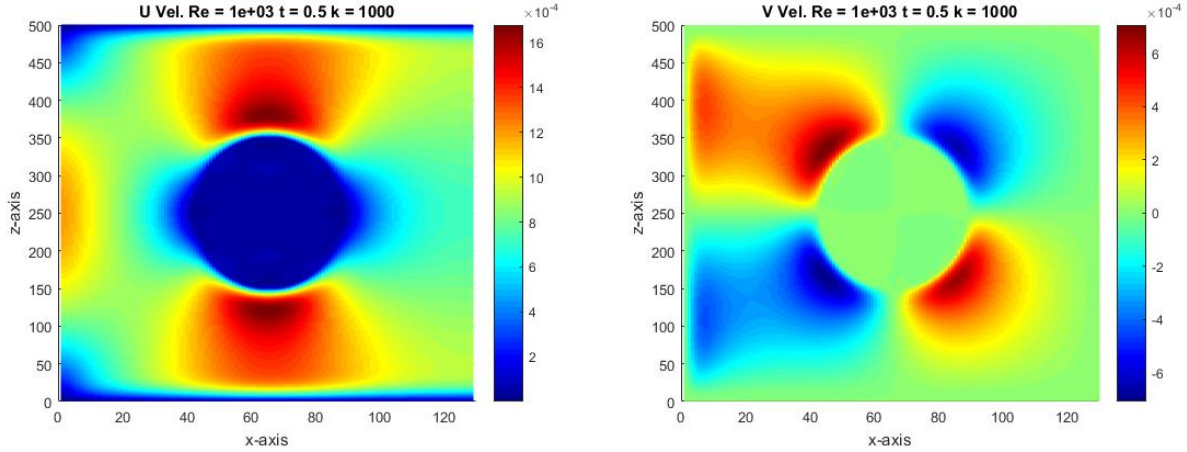

Figure 2.18: (a) U and (b) V velocity profile at $t = 0.5$ s.

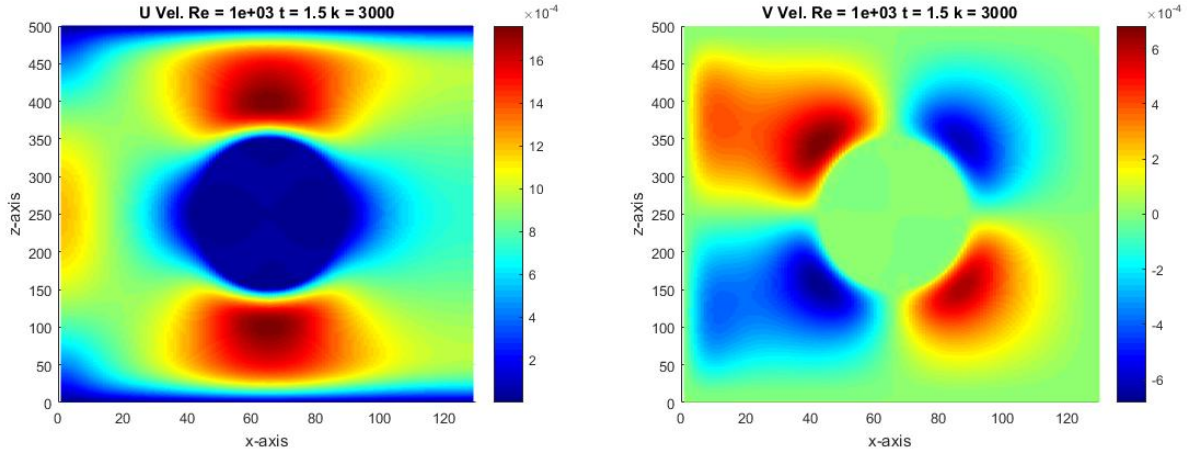

Figure 2.19: (a) U and (b) V velocity profile at $t = 1.5$ s.

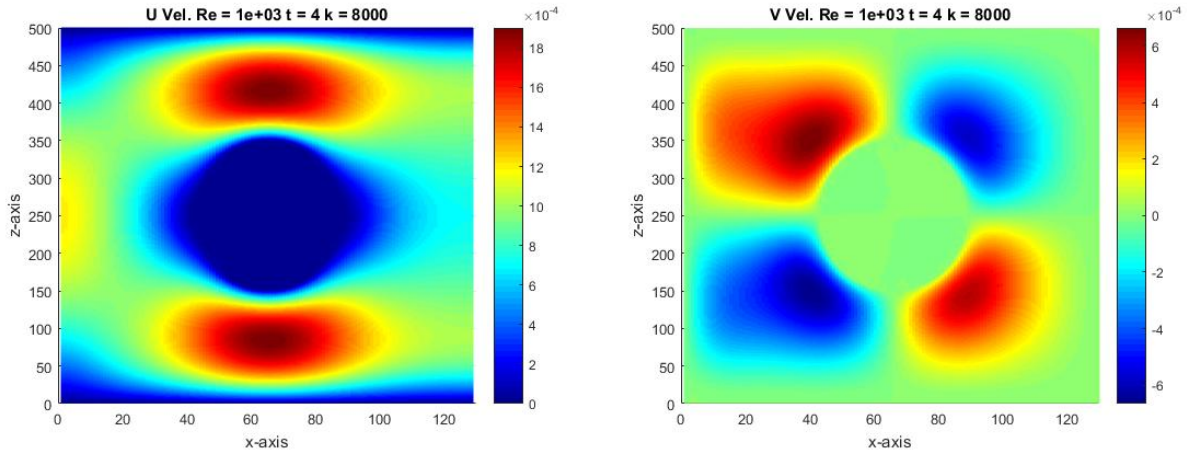

Figure 2.20: (a) U and (b) V velocity profile at $t = 4$ s.

Figure 2.20 displays the stationary solid body immersed inside of a fluid region. The dark blue area represents the solid which has a zero velocity, and also, the solid blue region of the walls of the cylinder represents that the wall is not moving and the no-slip boundary conditions are effective. The numerical code is verified and then modified to solve for flow through an artery with an adjoining rigid saccular aneurysm described in Section 2.2.

2.2 Laminar flow through a rigid cerebral artery with an adjoining rigid saccular aneurysm

2.2.1 Problem Formulation

In this section, laminar flow through a rigid cerebral artery and its adjoining rigid saccular aneurysm is computed and simulated. The two-dimensional incompressible Navier-Stokes equations in Section 2.1.1 model the flow of blood. That is,

$$U_t = -P_x - (U^2)_x - (UV)_z + \frac{1}{Re}(U_{xx} + U_{zz}) + F_U, \tag{2.74}$$

$$V_t = -P_z - (UV)_x - (V^2)_z + \frac{1}{Re}(V_{xx} + V_{zz}) + F_V, \tag{2.75}$$

$$U_x + V_z = 0. \tag{2.76}$$

The initial conditions and boundary conditions are the same as used in Section 2.1 except for the u_W boundary condition. Fluid is now restricted to flowing through a very small portion of the West boundary at the opening of the artery. At other locations on the West boundary, u_W is set to zero (See figure 2.21).

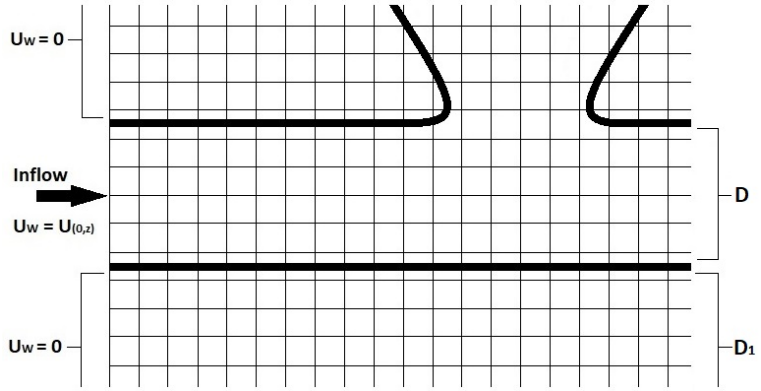

Figure 2.21: Illustration of the u_W boundary condition and inflow at the opening of the artery.

The West boundary condition, u_W, is defined using the velocity of the inflow fluid, the location of the opening of artery in the Eulerian domain, the diameter of the artery, and the equation of a parabola similar to in Section 2.1. In figure 2.21, defining the length of the lower region under the bottom of the artery as D_1, and the inflow region as D, results in the following equation for u_W, for the inflow region only,

$$u_W = \frac{u_{\max}}{D^2} \left((D_1 + D) - z\right)(z - D_1) \tag{2.77}$$

The result of this flow is that of laminar (Poiseuille) flow through the designated domain.

2.2.2 Methodology

The numerical methods for this problem are discussed in detail in Section 2.1.2with a couple of modifications needed in order to obtain the desired results for this specific problem. In the cell-flagging process, we modify how the coordinate points are determined for the

immersed boundary. The initial coordinate points for the shape of the artery and aneurysm are taken from [24]. A thickness of the boundary is created in order to simulate a replica of an in-vivo artery and adjoining aneurysm. All dimensions are scaled to fit the numerical scaling of this problem.

Flagging of the interior, exterior, and boundary cells for the cerebral artery and adjoining saccular aneurysm are interchanged to simulate fluid flow through the immersed boundary instead of around it.

Algorithm I (Section 2.1.2.1) is used to determine the final velocities of the fluid domain. The forcing components are calculated the same way as done in Section 2.1.4 except, now, the boundary is given a thickness. Therefore, there is an exterior boundary wall and an interior boundary wall. The exterior boundary wall will have fluid approaching from the outside whereas the interior boundary wall will have fluid approaching from the inside. See figure 2.22 below.

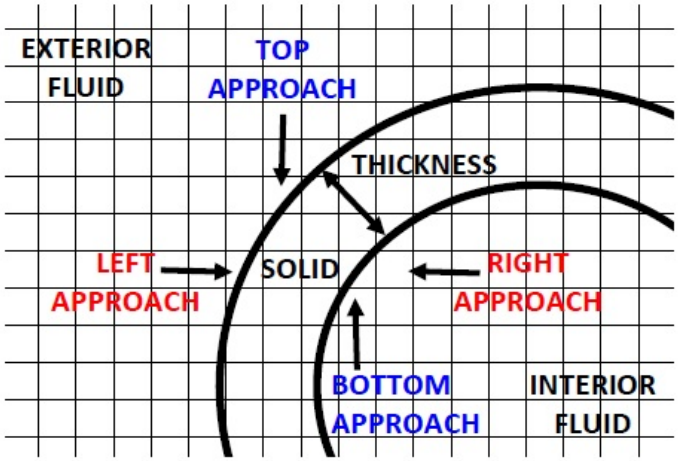

Figure 2.22: Illustration of thickness of boundary with fluid approach

Since the boundary is rigid in this problem as in the first problem, the velocities of the boundary are zero. Depending on the orientation of the boundary in each cell with respects to the location of the fluid on that boundary, it can be determined whether a left or right

approach will be use in the horizontal direction and whether a top or bottom approach will be used in the vertical direction.

2.2.3 Results

Figures 2.23-2.32 simulate the U and V velocity profiles of laminar blood flow through a rigid cerebral artery with an adjoining rigid saccular aneurysm. The following parameters used to run this simulation are: $\rho = 1060$, $\mu = 2.78 \times 10^{-3}$, $u_{\max} \approx 7.958 \times 10^{-1}$, $L_x = 1$, $L_z = 0.4$, $D = 8.66 \times 10^{-2}$, $Th = 5 \times 10^{-3}$ which is the two-dimensional thickness of the arterial wall, $n_x = 800$, $n_z = 240$, $Re = 1000$, $\Delta x = 1.25 \times 10^{-3}$, $\Delta z \approx 1.67 \times 10^{-3}$, $\Delta t = 5 \times 10^{-4}$, and $NT = 4000$.

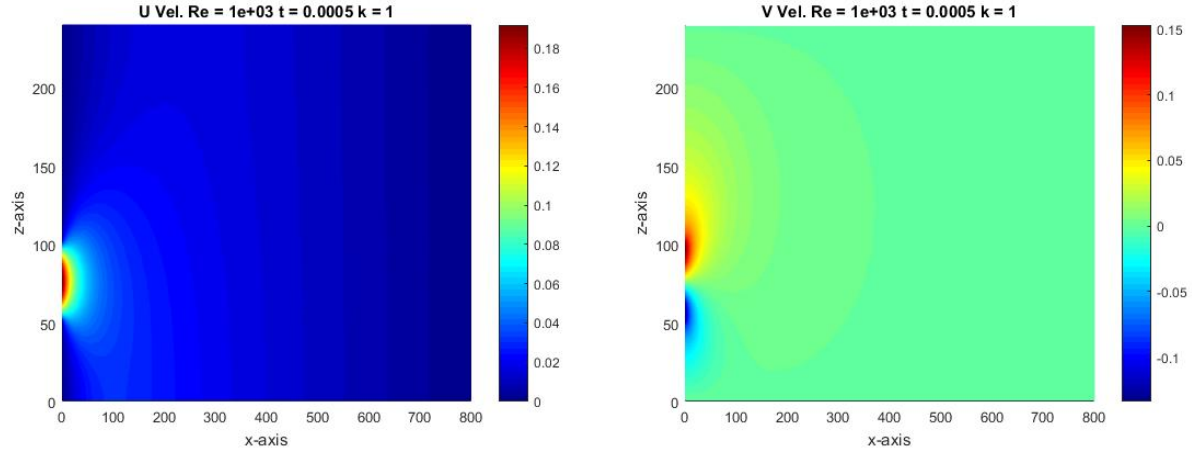

Figure 2.23: (a) U and (b) V velocity profiles at $t = 5 \times 10^{-4}$ s.

Figure 2.23 is the initial step of blood flow as it enters the artery from the West boundary. The blood has an inlet velocity of approximately 7.958×10^{-1} m/s between the top and bottom boundaries of the artery. The velocity is set to zero everywhere else on the West boundary. At this early time, the boundary is not yet defined by the numerical calculations.

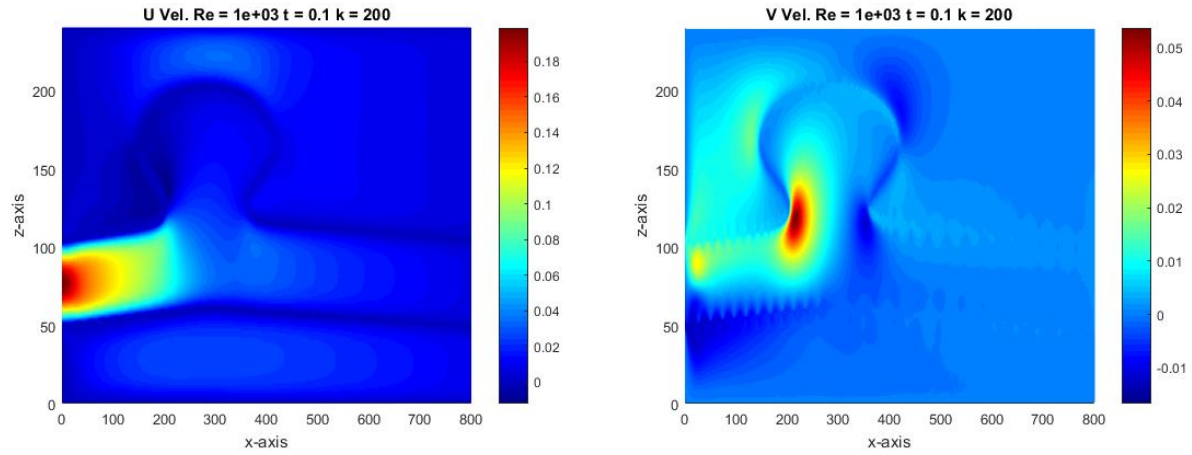

Figure 2.24: (a) U and (b) V velocity profile at $t = 0.1$ s.

Figure 2.24(a) represents a clearly defined boundary of the artery and aneurysm walls which is defined as dark blue (no movement). Therefore, all velocities shown here, not equal to zero, are effects from the inflow of the U velocity. The appearance of fluid moving outside of the artery and aneurysm walls are from the initial effects of x-velocities prior to boundary enforcement and not the dynamic effects of fluid moving through the artery.

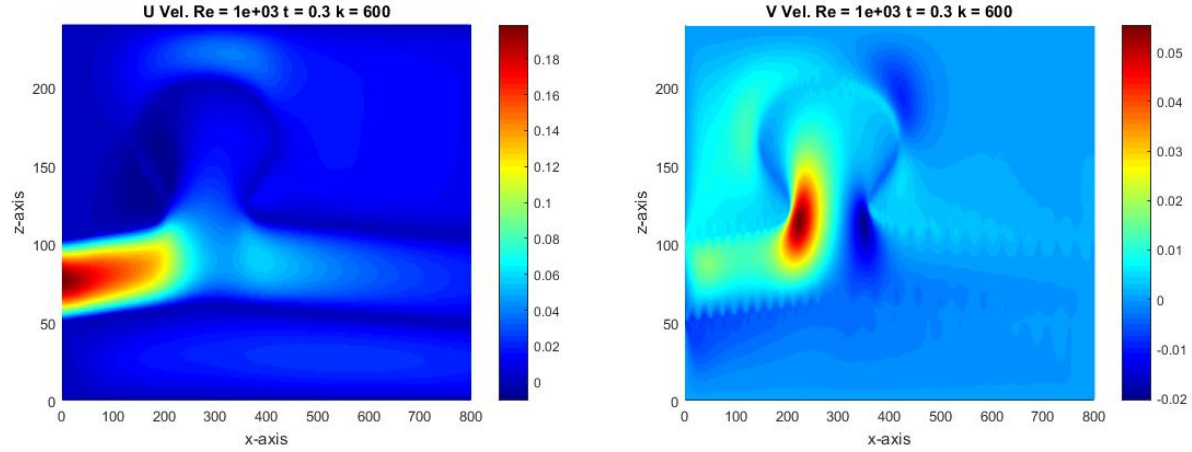

Figure 2.25: (a) U and (b) V velocity profile at $t = 0.3$ s.

As the fluid approaches the opening of the aneurysm, fluid is forced upwards into the aneurysm hitting the right side of the aneurysm. Note that the velocities on the outside of

the solid body are independent of the interior fluid flow and are artifact of the numerical code. These velocities are still trying to slow down from the initial step when they were first introduced when there was no boundary clearly defined and fluid was free to go everywhere.

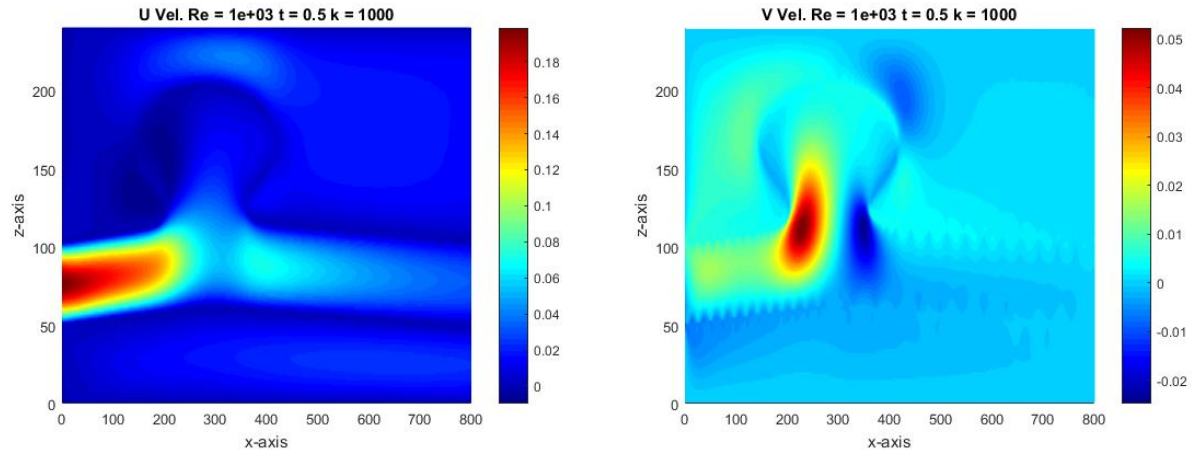

Figure 2.26: (a) U and (b) V velocity profile at $t = 0.5$ s.

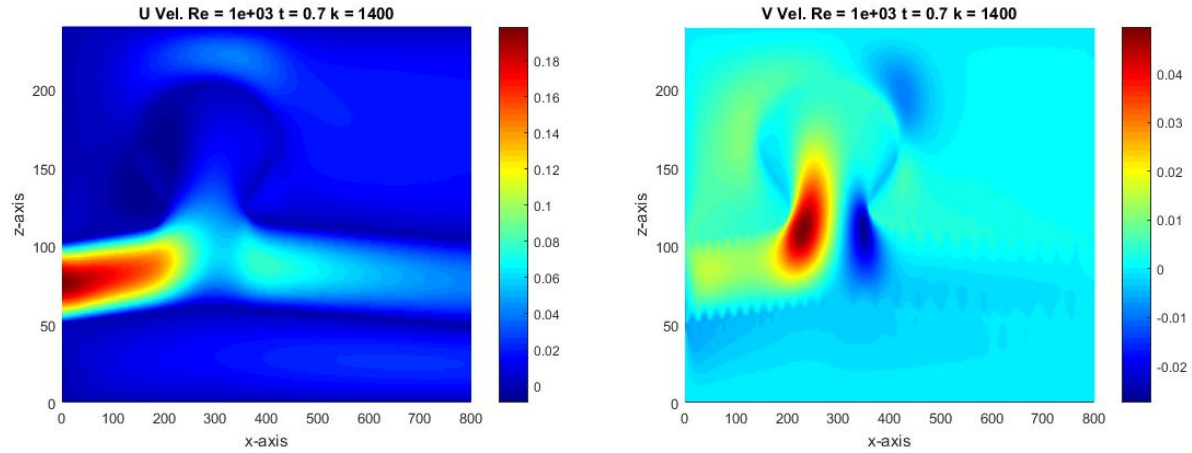

Figure 2.27: (a) U and (b) V velocity profile at $t = 0.7$ s.

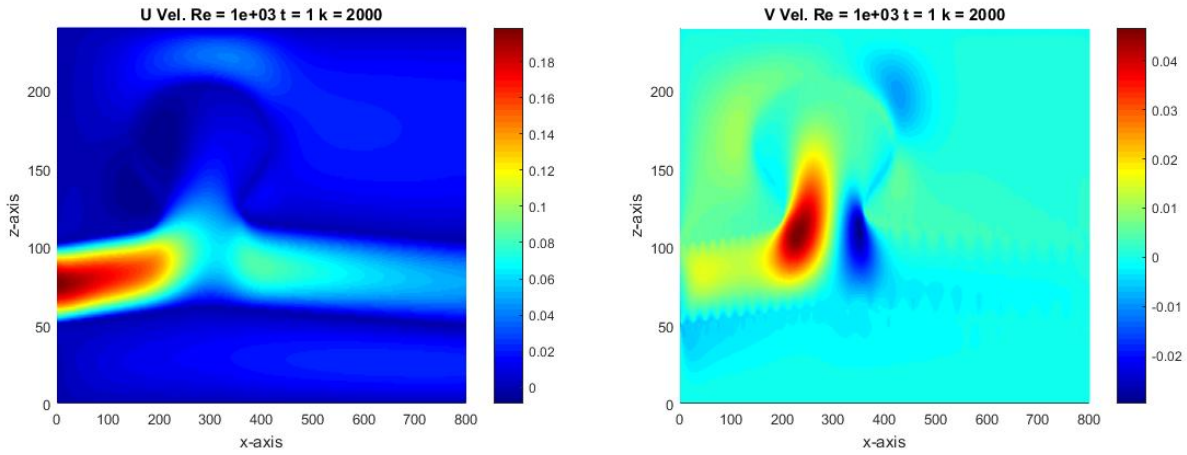

Figure 2.28: (a) U and (b) V velocity profile at $t = 1$ s.

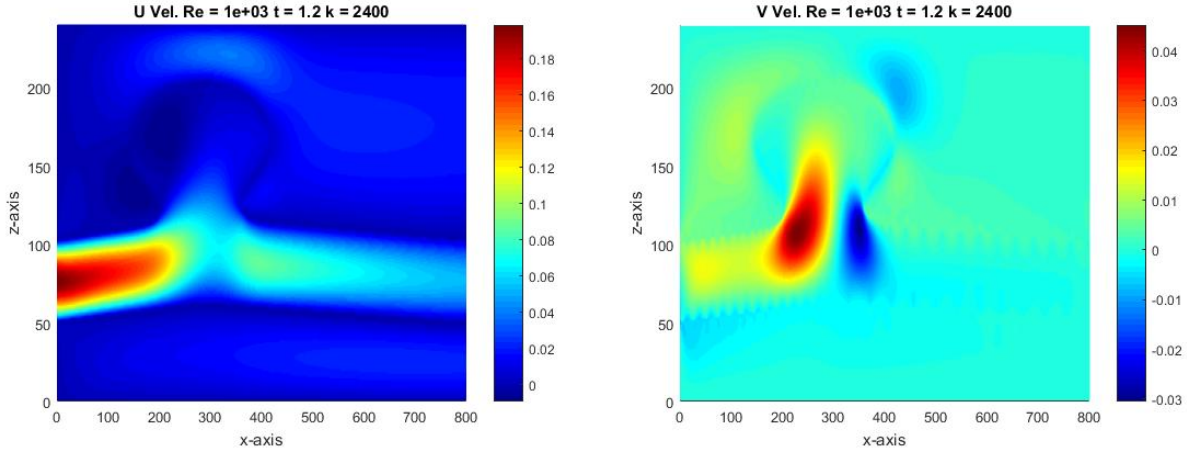

Figure 2.29: (a) U and (b) V velocity profile at $t = 1.2$ s.

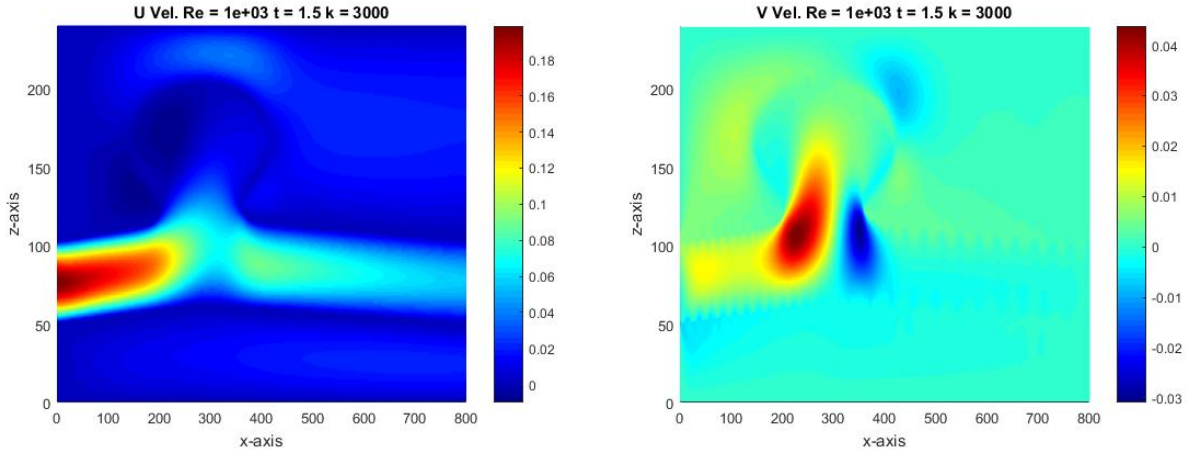

Figure 2.30: (a) U and (b) V velocity profile at $t = 1.5$ s.

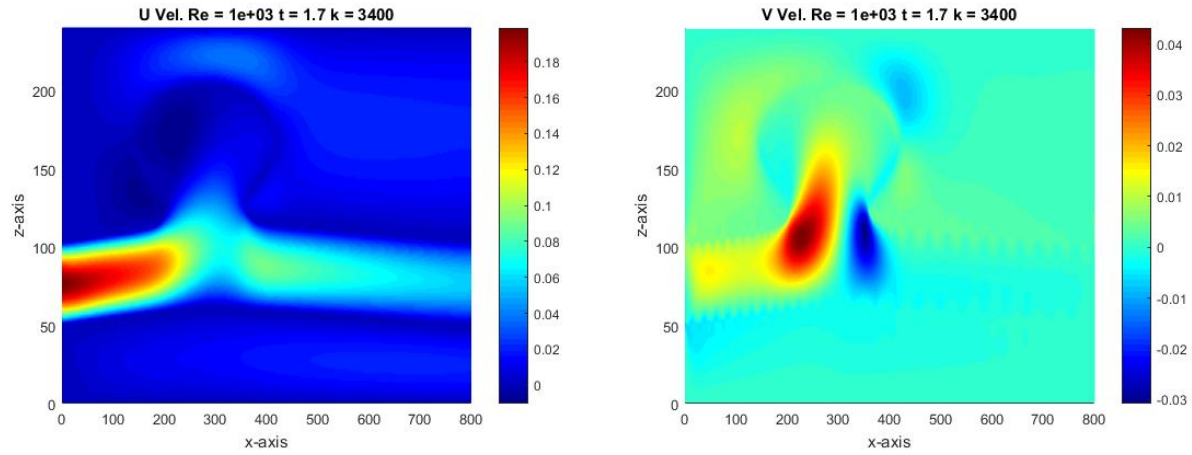

Figure 2.31: (a) U and (b) V velocity profile at $t = 1.7$ s.

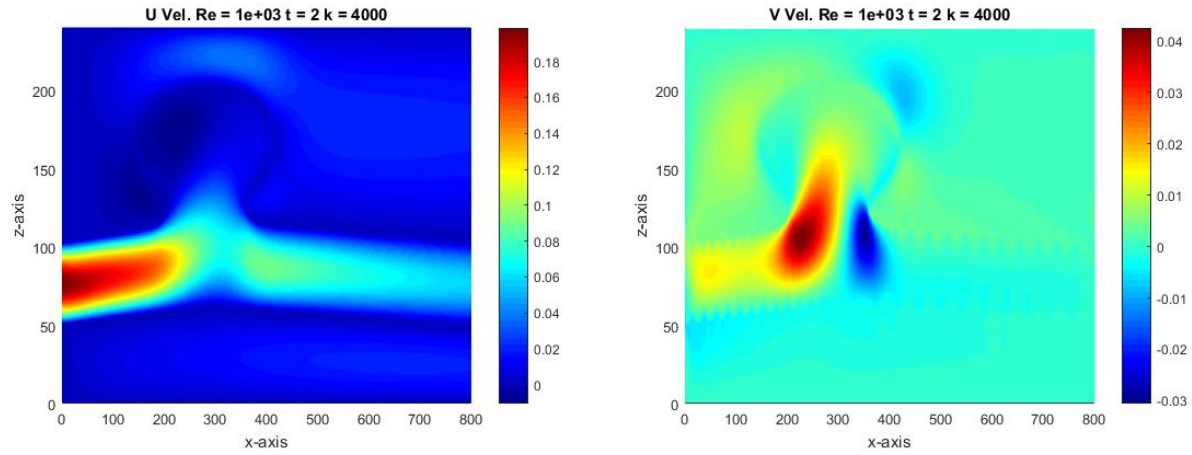

Figure 2.32: (a) U and (b) V velocity profile at $t = 2$ s.

These results are qualitatively in agreement with results in [24]. Pulsatile blood flow is now introduced at the inflow domain and is presented in Section 2.3.

2.3 Pulsatile flow through a rigid cerebral artery with an adjoining rigid saccular aneurysm

2.3.1 Problem Formulation

In this section, pulsatile flow through a rigid cerebral artery and its adjoining rigid saccular aneurysm are computed and simulated. This is done using the same two-dimensional

incompressible Navier-Stokes equations used in Section 2.1.1. The initial conditions and boundary conditions are the same as used in Section 2.2.

2.3.2 Methodology

The numerical method is discussed in detail in Section 2.1.2. The immersed boundary is defined the same as in Section 2.2.2. Here, we define pulsatile flow through the artery by changing the inlet velocity, $u_{\max}$, at each time step in equation 2.78. The new profile represents one heart beat averaging 60 beats per minute. Using a fast Fourier transform, the approximation of the inlet fluid flow is defined as [24],

$$u_{\max} = \frac{\mu}{5d\rho} \sum_{n=1}^{9} \left(a_n \cos\left(2\pi(n-1)t\right) + b_n \sin(2\pi(n-1)t)\right). \tag{2.78}$$

Figure 2.33 illustrates the inlet velocity boundary profile on the West boundary of the artery.

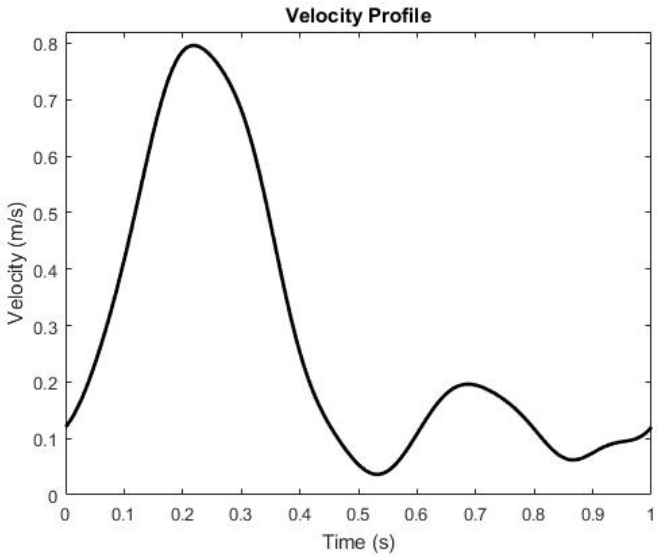

Figure 2.33: Inlet velocity profile of blood flow through artery, $u_{\max}$.

The inflow velocity is at its minimum around $t = 5.3 \times 10^{-1}$ s and it is at its maximum around $t = 2.2 \times 10^{-1}$ s.

2.3.3 Results

Figures 2.34 – 2.42 simulate the U and V velocity profiles of pulsatile fluid flow through a rigid cerebral artery with an adjoining rigid saccular aneurysm. Note changes in the color-bar for each figure at each time-step. The following parameters used to run this simulation are: $\rho = 1060$, $\mu = 2.78 \times 10^{-3}$, $L_x = 1$, $L_z = 0.4$, $D = 8.66 \times 10^{-2}$, $Th = 5 \times 10^{-3}$, $n_x = 800$, $n_z = 240$, $Re = 1000$, $\Delta x = 1.25 \times 10^{-3}$, $\Delta z \approx 1.67 \times 10^{-3}$, $\Delta t = 5 \times 10^{-4}$, and $NT = 4000$.

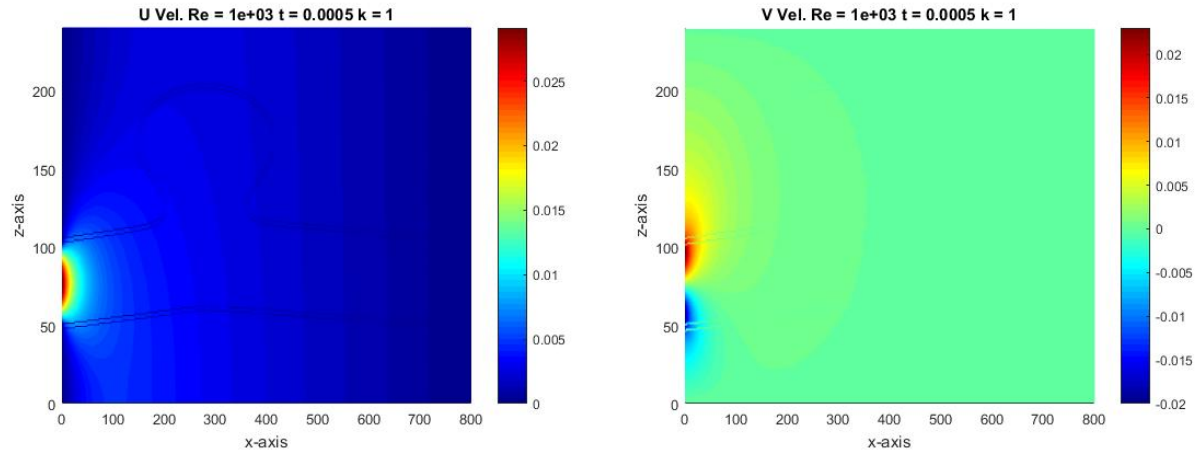

Figure 2.34: (a) U and (b) V velocity profile at $t = \Delta t$ s, $u_{\max} \approx 1.2073 \times 10^{-1}$ m/s

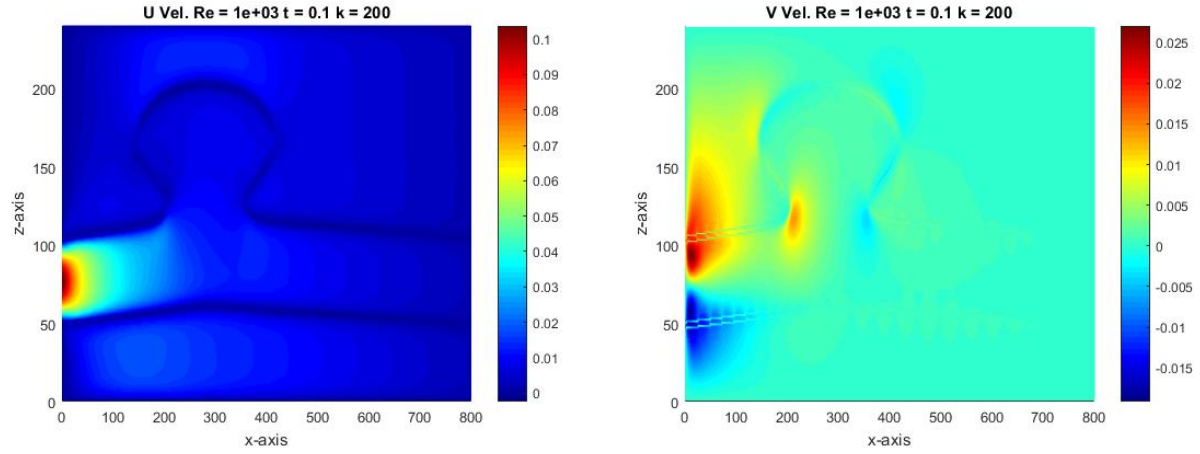

Figure 2.35: (a) U and (b) V velocity profile at $t = 0.1$ s, $u_{\max} \approx 4.1587 \times 10^{-1}$ m/s

Figure 2.34 is the initial step of blood flow as it enters the artery from the West boundary. Figure 2.35(a) displays a completely defined boundary of the artery and aneurysm wall. The

interior and exterior fluids have become independent of each other. In figure 2.35(b), flow outside of the vessel is trying to converge to zero, even though it has effects from the initial U inlet velocities.

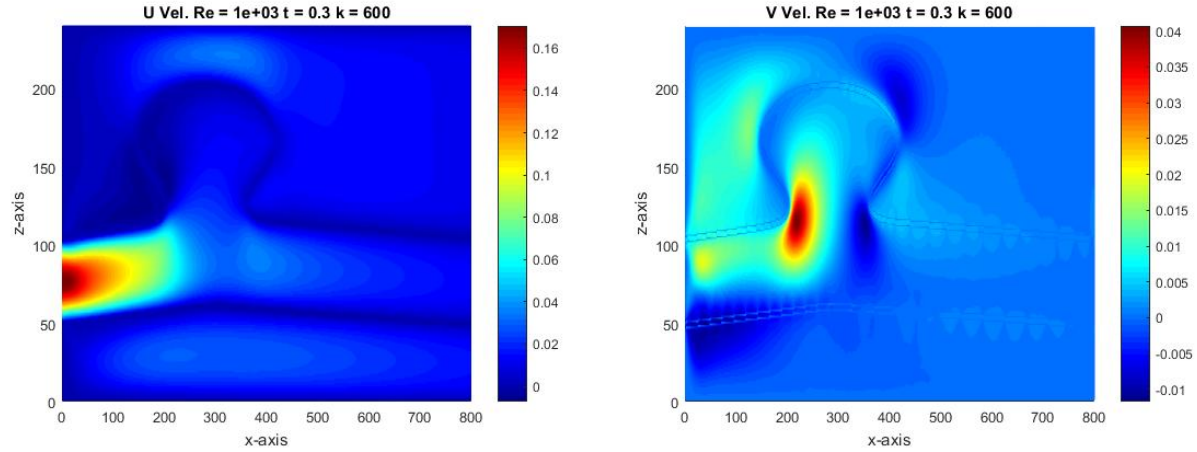

Figure 2.36: (a) U and (b) V velocity profile at $t = 0.3$ s, $u_{\max} \approx 6.8165 \times 10^{-1}$ m/s

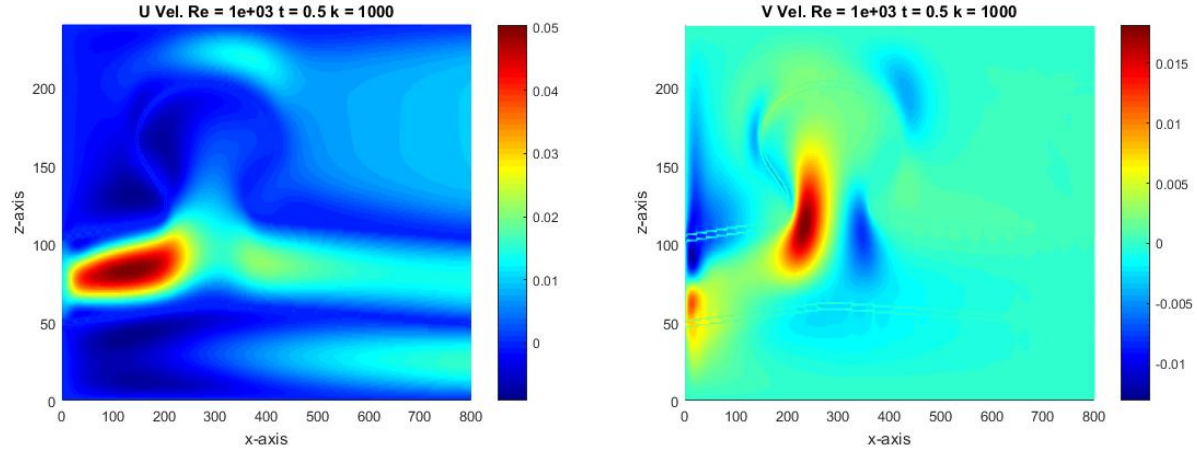

Figure 2.37: (a) U and (b) V velocity profile at $t = 0.5$ s, $u_{\max} \approx 5.3618 \times 10^{-2}$ m/s

In figure 2.37(a), as the fluid is pulsating, negative velocity is occurring as the fluid is beginning to slow down at this time-step. Figure 2.37(b) is trying to converge to zero. The red region represents flow in the positive z direction, and the dark blue region represents flow in the negative z direction which is the beginning of a vortex inside the aneurysm.

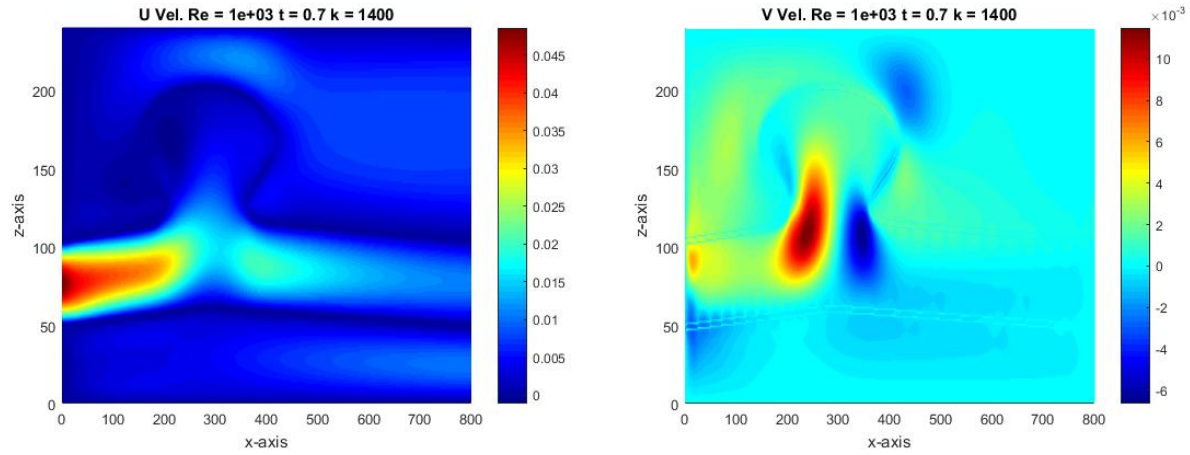

Figure 2.38: (a) U and (b) V velocity profile at $t = 0.7$ s, $u_{\max} \approx 1.9438 \times 10^{-1}$ m/s

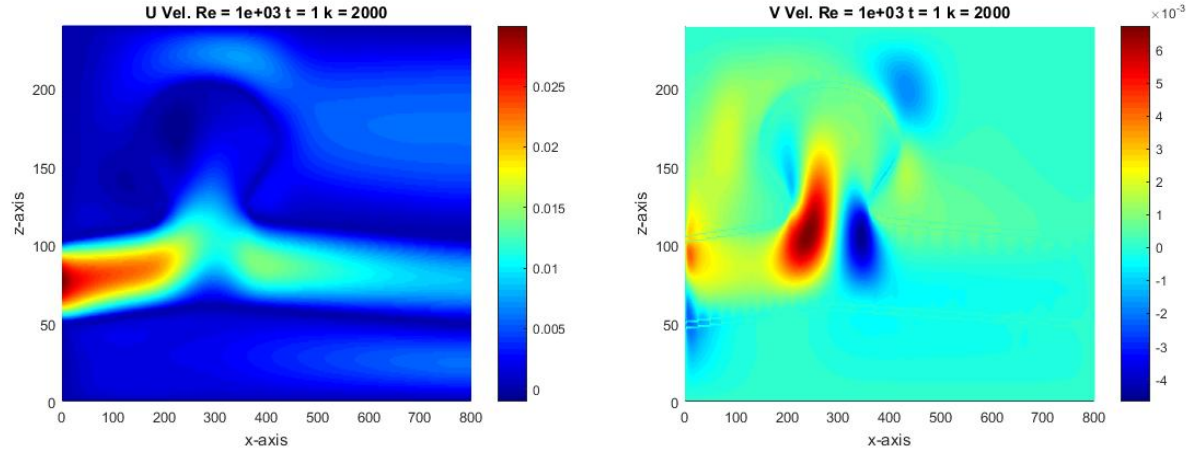

Figure 2.39: (a) U and (b) V velocity profile at $t = 1$ s, $u_{\max} \approx 1.2009 \times 10^{-1}$ m/s

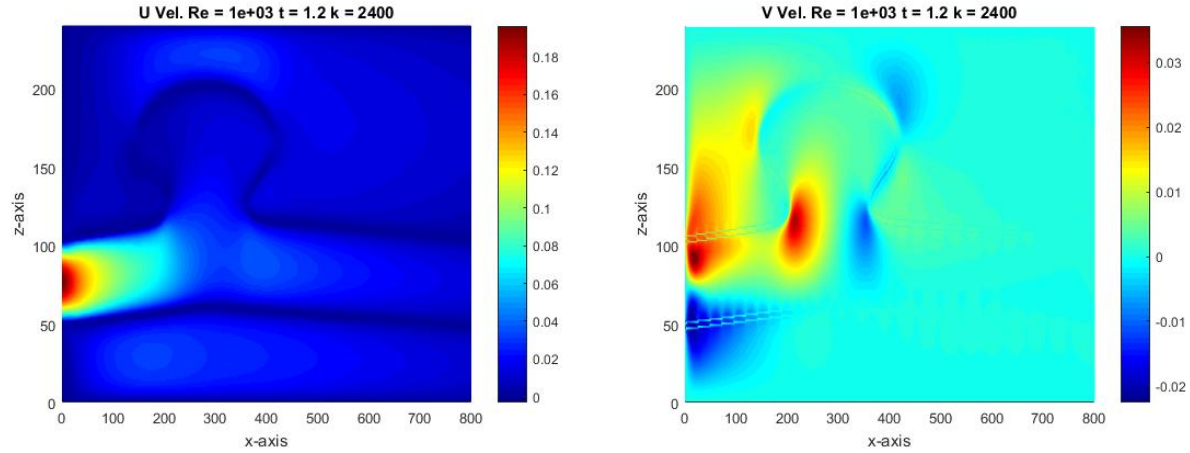

Figure 2.40: (a) U and (b) V velocity profile at $t = 1.2$ s, $u_{\max} \approx 7.8563 \times 10^{-1}$ m/s

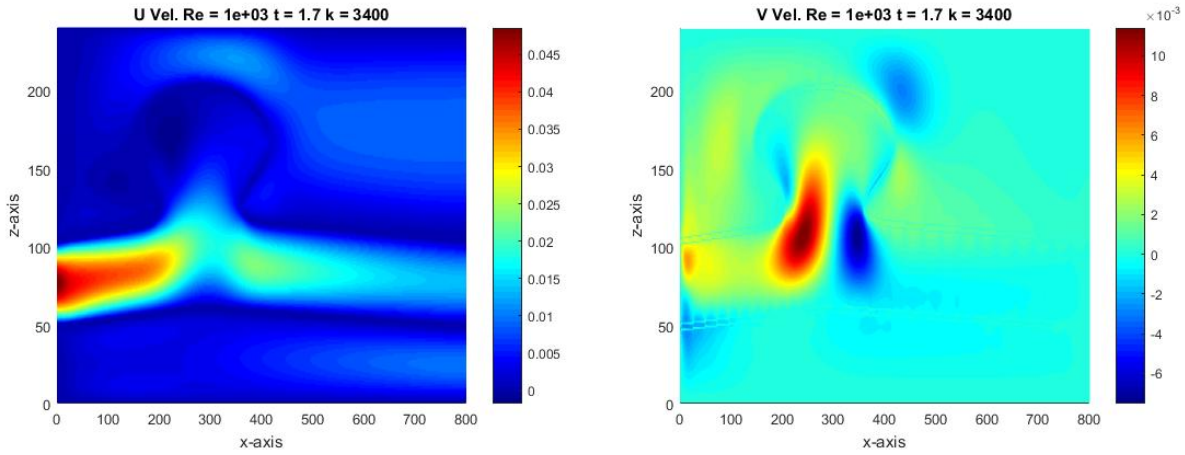

Figure 2.41: (a) U and (b) V velocity profile at $t = 1.7$ s, $u_{\max} \approx 1.9438 \times 10^{-1}$ m/s

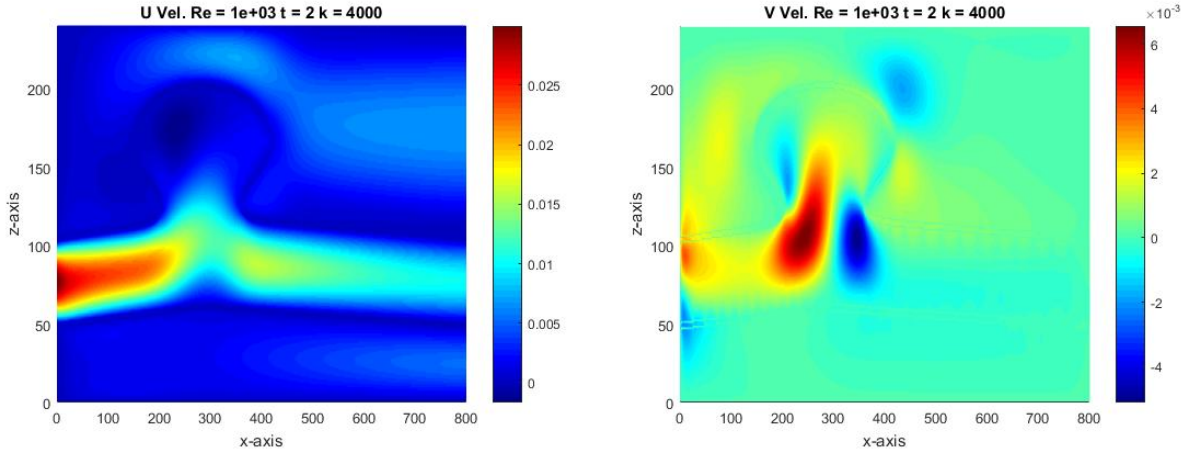

Figure 2.42: (a) U and (b) V velocity profile at $t = 2$ s, $u_{\max} \approx 1.2009 \times 10^{-1}$ m/s

All figures in this section simulate pulsatile blood flow through a rigid cerebral artery and its adjoining rigid saccular aneurysm at the chosen time-steps. Blood remains inside the inflow domain as it pulsates through. No fluid is leaking out of the boundary. With results obtained from this project, the numerical code is modified to simulate movement of the artery and aneurysm walls. This is simulated in the final project presented in Chapter 3.

Chapter 3

FLOW WITHIN A DEFORMABLE IMMERSED BOUNDARY

In this chapter, we focus on the fluid-solid interaction of an elastic body and its surrounding fluid. The coupling of fluid and structure systems allow for the movement of the cerebral artery and its adjoining saccular aneurysm as fluid forces are imposed upon it, internally and externally. The Navier-Stokes equations used in Section 2.1.1 are coupled with the dynamic equation for the motion of an elastic body as done in [21]. The Navier-Stokes equations are solved in the Eulerian coordinate system as done in the previous projects, and the dynamic motion equation is solved in the Lagrangian coordinate system.

3.1 Problem Formulation

Consider the vector form of the two-dimensional Navier-Stokes equations for motion of the incompressible fluid in the Eulerian coordinate space (equation 2.1),

$$\frac{\partial \boldsymbol{u}}{\partial t} = -\boldsymbol{u} \cdot \nabla \boldsymbol{u} + \frac{1}{Re}\nabla^2 \boldsymbol{u} - \nabla p + \boldsymbol{f},$$

along with the modified continuity equation,

$$\nabla \cdot \boldsymbol{u} - q = 0, \tag{3.1}$$

where q is the mass source/sink to satisfy the mass conservation for the cell containing the immersed boundary [21]. As done with the pressure, the mass source/sink is also applied at the cell center.

The two-dimensional Navier-Stokes equations are coupled with the dynamic equation for the motion of an elastic body in the Lagrangian coordinate system in order to create

movement of the solid body. Each block is moved by external and internal forces such as the elastic ($\boldsymbol{F}_E$), buoyancy ($\boldsymbol{F}_G$), and hydrodynamic ($\boldsymbol{F}_H$) forces, and the motion equation for each block is described by Newton's second law,

$$\rho_s V \frac{\partial^2 \boldsymbol{X}}{\partial t^2} = \boldsymbol{F}_E + \boldsymbol{F}_G + \boldsymbol{F}_H, \tag{3.2}$$

where ρ_s is the density of the elastic body, V is the volume of each block, and $\boldsymbol{X}$ is the location of each material point [21].

The following section will explain the methodology of the coupling of the Navier-Stokes equations with the equation for the motion of an elastic body. Algorithms are given as well as a flow chart. Derivation of the Navier-Stokes equations is briefly explained as they were previously derived in Chapter 2.

3.2 Methodology

3.2.1 Eulerian and Lagrangian Grid

The Eulerian-Lagrangian approach is introduced where both systems are coupled in order for the fluid-structure interaction to take place. The incompressible Navier-Stokes equations are solved in the Eulerian coordinate system on a rectangular domain which is fixed in time as described in Section 2.1.1. The initial conditions of U, V, and P, and the boundary conditions are defined the same way as in Section 2.1.1. The method for flagging each cell after movement at each time-step is the same method used for the last two projects and can be found in Section 2.2.2. The inlet velocity for the West boundary at each time step is defined in Section 2.3.2.

The dynamic equation for the motion of an elastic body is solved in the Lagrangian coordinate system. The solid body is divided by a finite number of cells where each cell has

a central point $\boldsymbol{X}$ in the Lagrangian coordinate system, (s_1, s_2), and Lagrangian lengths of Δs_1 and Δs_2 (figure 3.1) [21].

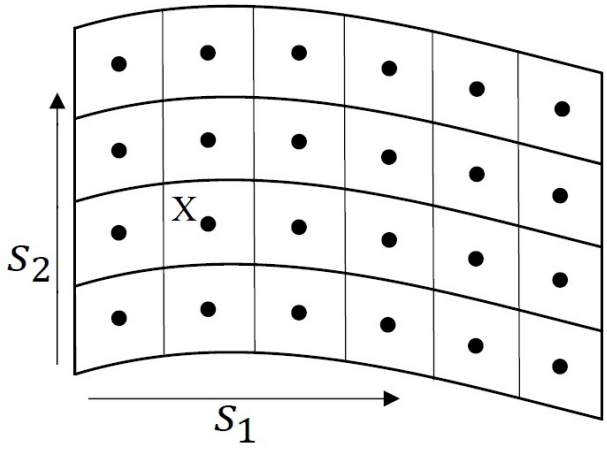

Figure 3.1: Elastic Body

Modifications of defining the elastic body take place in comparison to the structure used in the paper written by Lee and Choi.

Recall equation 3.2,

$$\rho_s V \frac{\partial^2 \boldsymbol{X}}{\partial t^2} = \boldsymbol{F}_E + \boldsymbol{F}_G + \boldsymbol{F}_H. \tag{3.3}$$

The elastic force, $\boldsymbol{F}_E$ is derived by first taking into consideration the equation for the elastic energy as follows [21],

$$E(\boldsymbol{X}) = \iint \sum_{a,b=1}^{2} \left[c_{ab}^T \left(T_{ab} - T_{ab}^0 \right)^2 + c_{ab}^B \left(B_{ab} - B_{ab}^0 \right)^2 \right] ds_1 ds_2. \tag{3.4}$$

Here, T_{ab} and B_{ab} are the tension ($a = b$) or shearing ($a \neq b$) effect and bending ($a = b$) or twisting ($a \neq b$) effect defined as,

$$T_{ab} = \frac{\partial \boldsymbol{X}}{\partial s_a} \cdot \frac{\partial \boldsymbol{X}}{\partial s_b} \tag{3.5}$$

$$B_{ab} = \sqrt{\frac{\partial^2 \boldsymbol{X}}{\partial s_a \partial s_b} \cdot \frac{\partial^2 \boldsymbol{X}}{\partial s_a \partial s_b}}, \tag{3.6}$$

and c_{ab}^T and c_{ab}^B are the tension or shearing and bending or twisting constants, respectively [21]. The initial conditions for the tension or shearing effect and bending or twisting effect, T_{ab}^0 and B_{ab}^0 [21], respectively, are defined as,

$$T_{ab}^0 = \begin{cases} 1, & \text{if } a = b, \\ 0, & \text{if } a \neq b, \end{cases} \quad and \quad B_{ab}^0 = 0. \tag{3.7}$$

Thus, the elastic force is defined by,

$$\boldsymbol{F}_E = \sum_{a,b=1}^{2} \left[\frac{\partial}{\partial s_a} \left(\kappa_{ab}^T \left(T_{ab} - T_{ab}^0 \right) \frac{\partial \boldsymbol{X}}{\partial s_b} \right) - \frac{\partial^2}{\partial s_a \partial s_b} \left(\kappa_{ab}^B \left(B_{ab} - B_{ab}^0 \right) \right) \right] A, \tag{3.8}$$

where $\kappa_{ab}^T = 4c_{ab}^T$ is the tension or shearing coefficient, $\kappa_{ab}^B = 2c_{ab}^B$ is the bending or twisting coefficient, and $A = \Delta s_1 \Delta s_2$ [21]. The non-dimensional dynamic equation for motion of the elastic body is expressed by,

$$\begin{aligned} \rho^* \frac{\partial^2 \boldsymbol{X}^*}{\partial t^{*\,2}} &= \sum_{a,b=1}^{2} \left[\frac{\partial}{\partial s_a^*} \left(K_{ab}^T \left(T_{ab}^* - T_{ab}^0 \right) \frac{\partial \boldsymbol{X}^*}{\partial s_b^*} \right) - \frac{\partial^2}{\partial s_a^* \partial s_b^*} \left(K_{ab}^B \left(B_{ab}^* - B_{ab}^0 \right) \right) \right] \\ &\quad + \rho^* \, \hat{i}_g Fr + \frac{\mathbf{F}_H^*}{V^*}, \end{aligned} \tag{3.9}$$

where $K_{ab}^T = \kappa_{ab}^T / \rho_f \, U^2 h$, $K_{ab}^B = \kappa_{ab}^B / \rho_f \, U^2 D^2 h$, $\rho^* = \rho_s / \rho_f$ is the ratio of solid to fluid densi-

ties, $\hat{i} = g/|g|$ where g is the gravitational acceleration, $Fr = |\boldsymbol{g}|D/U^2$ is the Froude number, $V* = \Delta s_1 \Delta s_2 h/D^3$ is the non-dimensional volume of each block, $\boldsymbol{F}_H^* = \boldsymbol{F}_H/\rho_f U^2 D^2$ is the non-dimensional hydrodynamic force acting on the immersed boundary, U ($\equiv u_{\max}$) is the maximum velocity of the fluid, and D is the characteristic length defined for each flow problem. [21]

We neglect gravitational acceleration of the fluid and the bending and twisting effects of the immersed boundary. Noting that this problem is solved in two-dimensional space, yielding $A = \Delta s_1 \Delta s_2/D^2$, the modified motion equation that is coupled with the Navier-Stokes equations is,

$$\rho \frac{\partial^2 \boldsymbol{X}}{\partial t^2} = \sum_{a,b=1}^{2} \left[\frac{\partial}{\partial s_a} \left(K_{ab}^T \left(T_{ab} - T_{ab}^0 \right) \frac{\partial \boldsymbol{X}}{\partial s_b} \right) \right] + \frac{\boldsymbol{F}_H}{A}. \tag{3.10}$$

The Crank-Nicolson method, an implicit second-order finite difference scheme, is used to discretize equation 3.10 in time for constant Δt as follows,

$$\begin{aligned} \rho \frac{\boldsymbol{X}^{n+1} - 2\boldsymbol{X}^n + \boldsymbol{X}^{n-1}}{\Delta t^2} &= \frac{1}{2} \sum_{a,b=1}^{2} \left[\frac{\partial}{\partial s_a} \left(K_{ab}^T \left(T_{ab}^{n+1} - T_{ab}^0 \right) \frac{\partial \boldsymbol{X}^{n+1}}{\partial s_b} \right) \right] \\ &+ \frac{1}{2} \sum_{a,b=1}^{2} \left[\frac{\partial}{\partial s_a} \left(K_{ab}^T \left(T_{ab}^{n} - T_{ab}^0 \right) \frac{\partial \boldsymbol{X}^{n}}{\partial s_b} \right) \right] \\ &+ \frac{1}{2} \frac{1}{A} \left(\mathbf{F}_H^{n+1} + \mathbf{F}_H^n \right). \end{aligned} \tag{3.11}$$

Substituting in the equations for the tension or shearing effects yields,

$$\begin{aligned}
\rho \frac{\boldsymbol{X}^{n+1} - 2\boldsymbol{X}^{n} + \boldsymbol{X}^{n-1}}{\Delta t^2} &= \frac{1}{2} \sum_{a,b=1}^{2} \left[\frac{\partial}{\partial s_a} \left(K_{ab}^{T} \left(\frac{\partial \boldsymbol{X}^{n+1}}{\partial s_a} \cdot \frac{\partial \boldsymbol{X}^{n+1}}{\partial s_b} - T_{ab}^{0} \right) \frac{\partial \boldsymbol{X}^{n+1}}{\partial s_b} \right) \right] \\
&+ \frac{1}{2} \sum_{a,b=1}^{2} \left[\frac{\partial}{\partial s_a} \left(K_{ab}^{T} \left(\frac{\partial \boldsymbol{X}^{n}}{\partial s_a} \cdot \frac{\partial \boldsymbol{X}^{n}}{\partial s_b} - T_{ab}^{0} \right) \frac{\partial \boldsymbol{X}^{n}}{\partial s_b} \right) \right] \\
&+ \frac{1}{2} \frac{1}{A} \left(\mathbf{F}_{H}^{n+1} + \mathbf{F}_{H}^{n} \right). \qquad (3.12)
\end{aligned}$$

Note that K_{ab}^{T} is chosen qualitatively for stability purposes. The center of each Lagrangian cell, $\boldsymbol{X}$, moves in time according to equation 3.12 [21]. The hydrodynamic forcing components are obtained directly from the Navier-Stokes equations.

3.2.2 Numerical Algorithms

3.2.2.1 Algorithm II

1. Initialize the Eulerian grid (fluid region) and the Lagrangian grid (solid region).

2. Define boundary conditions, initial conditions, and input parameters (as necessary).

The following steps are necessary to get a defined immersed boundary before movement of the boundary can take place:

3. Begin computation loop for rigid boundary at $t = \Delta t$.

4. Define inlet velocity of fluid for u_W.

5. Compute the terms to be used in calculating the imposed forces on the rigid body:

(a) Compute the preliminary nonlinear terms $\mathcal{N}(\boldsymbol{u}^n)$,

$$\mathcal{N}(U^n) = \left((U^n)^2\right)_x + \left(U^n V^n\right)_z \tag{3.13}$$

$$\mathcal{N}(V^n) = \left(U^n V^n\right)_x + \left((V^n)^2\right)_z . \tag{3.14}$$

(b) Compute the preliminary viscosity terms $\mathcal{L}(\boldsymbol{u}^n)$ explicitly,

$$\mathcal{L}(U^n) = \frac{1}{Re}\left(U^n_{xx} + U^n_{zz}\right) \tag{3.15}$$

$$\mathcal{L}(V^n) = \frac{1}{Re}\left(V^n_{xx} + V^n_{zz}\right). \tag{3.16}$$

(c) Compute the gradient of the pressure terms ∇p^n,

$$\tilde{P}^n = \left\langle \left(P^n\right)_x, \left(P^n\right)_z \right\rangle . \tag{3.17}$$

(d) Compute the imposed forces F_U^{n+1} and F_V^{n+1},

$$F_U^{n+1} = \frac{\tilde{U}^n - U^n}{\Delta t} + \nabla P_U^n + \mathcal{N}(U^n) - \mathcal{L}(U^n) \tag{3.18}$$

$$F_V^{n+1} = \frac{\tilde{V}^n - V^n}{\Delta t} + \nabla P_V^n + \mathcal{N}(V^n) - \mathcal{L}(V^n). \tag{3.19}$$

6. Update the intermediate velocities $\boldsymbol{u}^{\diamond}$, $\boldsymbol{u}^{\diamond\diamond}$, $\boldsymbol{u}^{\diamond\diamond\diamond}$, and $\boldsymbol{u}^{4\diamond}$:

   (a) Update $\boldsymbol{u}^{\diamond}$ by forcing terms,

$$U^{\diamond} = U^n + \Delta t\ F_U^{n+1} \tag{3.20}$$

$$V^{\diamond} = V^n + \Delta t\ F_V^{n+1}. \tag{3.21}$$

   (b) Update $\boldsymbol{u}^{\diamond\diamond}$ by nonlinear terms,

$$U^{\diamond\diamond} = U^{\diamond} - \Delta t \left[\left((U^n)^2 \right)_x + \left(U^n V^n \right)_z \right] \tag{3.22}$$

$$V^{\diamond\diamond} = V^{\diamond} - \Delta t \left[\left(U^n V^n \right)_x + \left((V^n)^2 \right)_z \right]. \tag{3.23}$$

   (c) Update $\boldsymbol{u}^{\diamond\diamond\diamond}$ by viscosity terms,

$$U^{\diamond\diamond\diamond} = U^{\diamond\diamond} + \frac{\Delta t}{Re} \left(U_{xx}^{\diamond\diamond\diamond} + U_{zz}^{\diamond\diamond\diamond} \right) \tag{3.24}$$

$$V^{\diamond\diamond\diamond} = V^{\diamond\diamond} + \frac{\Delta t}{Re} \left(V_{xx}^{\diamond\diamond\diamond} + V_{zz}^{\diamond\diamond\diamond} \right). \tag{3.25}$$

   (d) Update $\boldsymbol{u}^{4\diamond}$ by computing the gradient of the pressure terms,

$$U^{4\diamond} = U^{\diamond\diamond\diamond} - \Delta t \left(\tilde{P}^{n+1} \right)_x \tag{3.26}$$

$$V^{4\diamond} = V^{\diamond\diamond\diamond} - \Delta t \left(\tilde{P}^{n+1} \right)_z. \tag{3.27}$$

7. Update $t = k\Delta t$, $k = 2, 3, ..., NK$, where NK is the number of iterations needed to clearly define the rigid immersed boundary.

3.2.2.2 Algorithm III

The following steps are necessary to compute movement of the fluid and the motion of the immersed boundary:

1. Begin computation loop for the deformable boundary at $t = k\Delta t$, $k = (NK + 1)$.

2. Compute steps 4. - 6. from Algorithm II.

3. Compute the hydrodynamic force [21]:

   (a) Calculate the mass source/sink,

$$q^{n+1} = \frac{1}{\Delta x \Delta z}\left[\left(U_2^{4\diamond} - U_1^{4\diamond}\right)\Delta z + \left(V_2^{4\diamond} - V_1^{4\diamond}\right)\Delta x\right]. \tag{3.28}$$

   (b) Calculate the Laplacian of the pseudo-pressure,

$$\nabla^2\phi^{n+1} = \frac{1}{\Delta t}\left(U_x^{4\diamond} + V_z^{4\diamond} - q^{n+1}\right). \tag{3.29}$$

   (c) Determine the final velocities, $\boldsymbol{u}^{n+1}$,

$$\boldsymbol{u}^{n+1} = \boldsymbol{u}^{4\diamond} - \Delta t \nabla\phi^{n+1}. \tag{3.30}$$

   (d) Calculate the hydrodynamic force,

$$\mathbf{F}_H^{n+1} = \int_A \left(\frac{\boldsymbol{u}^{n+1} - \boldsymbol{u}^n}{\Delta t} + \mathcal{N}\left(\boldsymbol{u}^n\right) - \boldsymbol{f}^{n+1}\right) dA. \tag{3.31}$$

4. Update the pressure [21],

$$P^{n+1} = \tilde{P}^{n+1} + \phi^{n+1} - \frac{\Delta t}{\mathrm{Re}}\nabla^2\phi^{n+1}. \tag{3.32}$$

5. Calculate the dynamic motion equation by solving for the partial derivatives which include the shearing and tension effects, T_{ab}, and by plugging the hydrodynamic force into equation 3.12,

$$\begin{aligned}\rho \frac{\boldsymbol{X}^{n+1} - 2\boldsymbol{X}^{n} + \boldsymbol{X}^{n-1}}{\Delta t^2} &= \frac{1}{2}\sum_{a,b=1}^{2}\left[\frac{\partial}{\partial s_a}\left(K_{ab}^{T}\left(\frac{\partial \boldsymbol{X}^{n+1}}{\partial s_a}\cdot\frac{\partial \boldsymbol{X}^{n+1}}{\partial s_b} - T_{ab}^{0}\right)\frac{\partial \boldsymbol{X}^{n+1}}{\partial s_b}\right)\right] \\ &+ \frac{1}{2}\sum_{a,b=1}^{2}\left[\frac{\partial}{\partial s_a}\left(K_{ab}^{T}\left(\frac{\partial \boldsymbol{X}^{n}}{\partial s_a}\cdot\frac{\partial \boldsymbol{X}^{n}}{\partial s_b} - T_{ab}^{0}\right)\frac{\partial \boldsymbol{X}^{n}}{\partial s_b}\right)\right] \\ &+ \frac{1}{2}\frac{1}{A}\left(\mathbf{F}_{H}^{n+1} + \mathbf{F}_{H}^{n}\right). \end{aligned} \tag{3.33}$$

6. Reconstruct the Lagrangian grid as a result of the moved center points $\boldsymbol{X}^{n+1}$.

7. Compute the new desired velocities of the solid boundary in each Eulerian cell containing the boundary to be used in computing the imposed forces.

8. Flag (or re-flag) each Eulerian cell as a solid, fluid, or boundary cell.

9. Update $t = k\Delta t$, $k = (n+2), ..., NT$, where NT is the maximum number of iterations chosen.

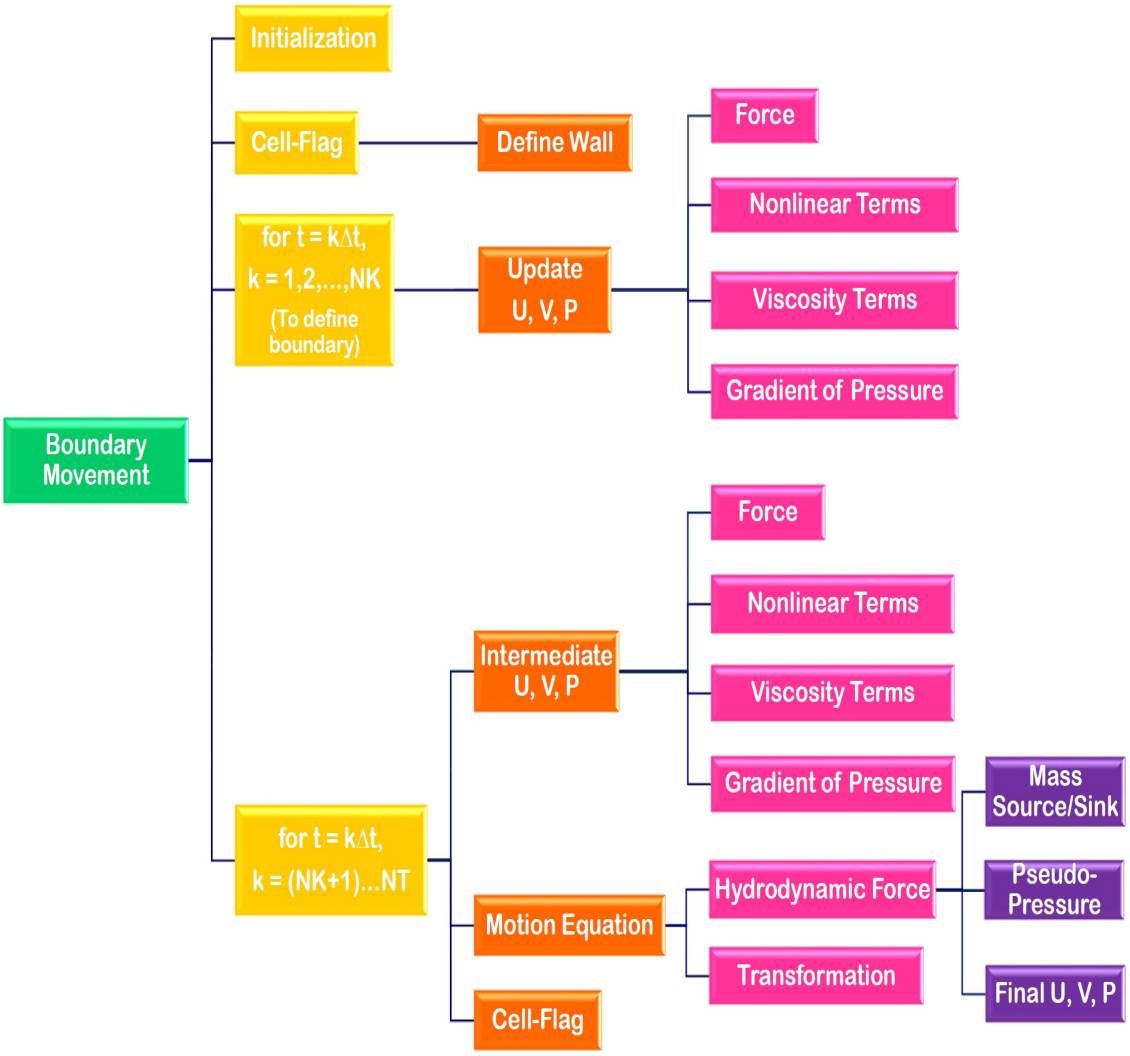

Figure 3.2: Flow Chart for a Deformable Body

3.2.3 Imposed Forces

In order to compute the imposed forcing terms, the preliminary values of the nonlinear, viscosity, and gradient of the pressure terms must be computed as done in Section 2.1.4. The steps are similar for both the rigid body and the elastic body. Linear interpolation must also take place on the boundary cells where needed as done in Section 2.1.4. The only difference is modification of the linear interpolation process on the boundary cells once the boundary begins to move.

After computing each term needed for calculation of the imposed forces, F_U^{n+1} and F_V^{n+1} (equations 3.18 and 3.19), are calculated as follows,

$$F_U^{n+1} = \frac{\tilde{U}^n - U^n}{\Delta t} + P_U^n + \mathcal{N}(U^n) - \mathcal{L}(U^n) \tag{3.34}$$

$$F_V^{n+1} = \frac{\tilde{V}^n - V^n}{\Delta t} + P_V^n + \mathcal{N}(V^n) - \mathcal{L}(V^n), \tag{3.35}$$

where $\tilde{U}^n$ and $\tilde{V}^n$ are to be determined.

Recall, equations 2.47, 2.49, 2.51, and 2.53 from Section 2.1.4 which solved for $\tilde{U}^n$ and $\tilde{V}^n$ in their respective positions,

$$\tilde{U}_{i-1} = \frac{U_{i-2} - U_P}{x_P - x_{i-1}}(x_P - x_i) + U_P, \tag{3.36}$$

$$\tilde{U}_i = \frac{U_{i+1} - U_P}{x_{i+2} - x_P}(x_{i+1} - x_P) + U_P, \tag{3.37}$$

$$\tilde{V}_j = \frac{V_{j+1} - V_P}{z_{j+2} - z_P}(z_{i+1} - z_P) + V_P, \tag{3.38}$$

$$\tilde{V}_{j-1} = \frac{V_{j-2} - V_P}{z_P - z_{j-1}}(z_P - z_j) + V_P. \tag{3.39}$$

For a rigid body, U_P and V_P, which are the velocities at the boundary (See figures 2.7-2.10), are defined to equal zero which results in equations 2.48, 2.50, 2.52, and 2.54 in Section 2.1.4. However, for the dynamic motion of the body, U_P and V_P are no longer forced to equal zero. Instead, their values are determined after (1) the motion equation (equation 3.12) is computed for the movement of the solid body, and (2) transformation takes place from the Lagrangian grid to the Eulerian grid. Further details are explained in Section 3.2.10 on obtaining U_P and V_P.

Once the imposed force equations are solved, the intermediate velocities, $\boldsymbol{u}^{\diamond}$ (equations 3.20 and 3.21), can be updated as follows,

$$U^{\diamond} = U^n + \Delta t\ F_U^{n+1} \tag{3.40}$$

$$V^{\diamond} = V^n + \Delta t\ F_V^{n+1}. \tag{3.41}$$

3.2.4 Nonlinear, Viscosity, and Pressure Terms

The intermediate velocities are update by computing the nonlinear, viscosity, and gradient of the pressure terms consecutively. Further detail can be found in Sections 2.1.5 - 2.1.7. These computations yield equations 3.22 - 3.27, respectively,

$$U^{\diamond\diamond} = U^{\diamond} - \Delta t \left[\left((U^n)^2 \right)_x + \left(U^n V^n \right)_z \right], \tag{3.42}$$

$$V^{\diamond\diamond} = V^{\diamond} - \Delta t \left[\left(U^n V^n \right)_x + \left((V^n)^2 \right)_z \right], \tag{3.43}$$

$$U^{\diamond\diamond\diamond} = U^{\diamond\diamond} + \frac{\Delta t}{Re} \left(U_{xx}^{\diamond\diamond\diamond} + U_{zz}^{\diamond\diamond\diamond} \right), \tag{3.44}$$

$$V^{\diamond\diamond\diamond} = V^{\diamond\diamond} + \frac{\Delta t}{Re} \left(V_{xx}^{\diamond\diamond\diamond} + V_{zz}^{\diamond\diamond\diamond} \right), \tag{3.45}$$

$$U^{4\diamond} = U^{\diamond\diamond\diamond} - \Delta t \left(\tilde{P}^{n+1} \right)_x, \tag{3.46}$$

$$V^{4\diamond} = V^{\diamond\diamond\diamond} - \Delta t \left(\tilde{P}^{n+1} \right)_z, \tag{3.47}$$

where $\tilde{P}^{n+1}$ is the intermediate pressure, and $U^{4\diamond}$ and $V^{4\diamond}$ are the updated intermediate velocities needed to compute the mass source/sink, pseudo-pressure, final velocities, and updated pressure in the following sections.

3.2.5 Mass Source/Sink

Determining the mass source/sink for each cell is dependent upon which discrete horizontal and vertical velocity components are inside the fluid and inside the solid. To obtain the mass source/sink, q^{n+1} (equation 3.28), needed to compute the Laplacian of the pseudo-pressure (equation 3.29), consider the illustration shown in figure 3.3. Only cells where at least one of the discrete horizontal or vertical velocity components is inside of the solid region are considered.

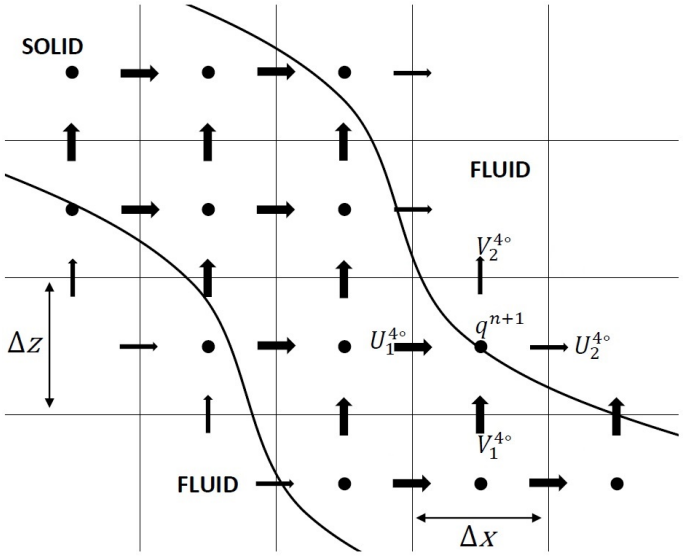

Figure 3.3: Mass Source/Sink

For any cell containing the solid body, the continuity equation reads,

$$U_2^{4\diamond}\Delta z + V_2^{4\diamond}\Delta x = U_1^{4\diamond}\Delta z + V_1^{4\diamond}\Delta x + q^{n+1}\Delta x\Delta z. \tag{3.48}$$

Solving for q^{n+1} yields equation 3.28,

$$q^{n+1} = \frac{1}{\Delta x\Delta z}\left[\left(U_2^{4\diamond} - U_1^{4\diamond}\right)\Delta z + \left(V_2^{4\diamond} - V_1^{4\diamond}\right)\Delta x\right]. \tag{3.49}$$

Consider the two-dimensional cell in figure 3.3 where $U_1^{4\diamond}$ and $V_1^{4\diamond}$ are the velocity components

inside the solid body and $U_2^{4\diamond}$ and $V_2^{4\diamond}$ are the velocity components outside the solid body [19]. For this particular cell, the continuity equation for the fluid region of the cell reads,

$$U_2^{4\diamond}\Delta z + V_2^{4\diamond}\Delta x = 0. \tag{3.50}$$

Substituting equation 3.50 into equation 3.48 and solving for q^{n+1} yields,

$$q^{n+1} = -\frac{U_1^{4\diamond}}{\Delta x} - \frac{V_1^{4\diamond}}{\Delta z}. \tag{3.51}$$

This is one of 13 cases to consider when solving for the mass source/sink of any given cell. Consider another case where if $U_1^{4\diamond}$ and $V_1^{4\diamond}$ were the velocity components outside the solid body and $U_2^{4\diamond}$ and $V_2^{4\diamond}$ were the velocity components inside the solid body, then the continuity equation would read,

$$-U_1^{4\diamond}\Delta z - V_1^{4\diamond}\Delta x = 0. \tag{3.52}$$

Substituting equation 3.52 into equation 3.48 and solving for q^{n+1} would yield,

$$q^{n+1} = \frac{U_2^{4\diamond}}{\Delta x} + \frac{V_2^{4\diamond}}{\Delta z}. \tag{3.53}$$

After each time-step, when the solid body moves causing the momentum forces and mass source/sink locations to change, cell-flagging/re-flagging must take place in order to determine the new fluid and solid cells for the next time-step. This is required in order to have more accuracy in computing the momentum forces and mass source/sink at the next time-step.

3.2.6 Pseudo-Pressure, Final Velocities, and Updated Pressure

The pseudo-pressure is used to correct the velocity field so that the continuity equation is satisfied at each computational time step [19]. To determine the pseudo-pressure, consider

equation 3.29,

$$\nabla^2 \phi^{n+1} = \frac{1}{\Delta t} \left(U_x^{4\diamond} + V_z^{4\diamond} - q^{n+1} \right). \tag{3.54}$$

This equation, yielding the Laplacian of the pseudo-pressure, is computed by substituting in the values of equations 3.26, 3.27, and 3.49. To solve for the pseudo-pressure, ϕ^{n+1}, the Laplacian inverse must be taken. The Laplacian matrix used for computing the pressure in Section 2.1.7 is also used here since the pseudo-pressure is defined at the center of each cell. Therefore, ϕ^{n+1} is defined as,

$$\phi^{n+1} = \Delta_\phi^{-1} \left(\nabla^2 \phi^{n+1} \right), \tag{3.55}$$

where Δ_ϕ^{-1} is the inverse of the Laplacian operator for ϕ. Computing the gradient of ϕ^{n+1} with respects to x and z for the intermediate velocities, $U^{4\diamond}$ and $V^{4\diamond}$, respectively, yields,

$$\nabla \phi^{n+1} = \left\langle \frac{\partial \phi^{n+1}}{\partial x}, \frac{\partial \phi^{n+1}}{\partial z} \right\rangle. \tag{3.56}$$

Once the gradient of ϕ^{n+1} is computed, the final velocities, U^{n+1} and V^{n+1}, illustrated in Chapter 4, are updated yielding,

$$U^{n+1} = U^{4\diamond} - \Delta t \frac{\partial \phi^{n+1}}{\partial x} \tag{3.57}$$

$$V^{n+1} = V^{4\diamond} - \Delta t \frac{\partial \phi^{n+1}}{\partial z}, \tag{3.58}$$

rewritten in vector form as equation 3.30,

$$\boldsymbol{u}^{n+1} = \boldsymbol{u}^{4\diamond} - \Delta t \nabla \phi^{n+1}. \tag{3.59}$$

Lastly, the pressure is updated using the pressure calculated in Section 3.2.4, the method from Section 2.1.7, the Laplacian of the pseudo-pressure defined by equation 3.29, and the

pseudo-pressure defined in equation 3.55 resulting in equation 3.32,

$$P^{n+1} = \tilde{P}^{n+1} + \phi^{n+1} - \frac{\Delta t}{\mathrm{Re}} \nabla^2 \phi^{n+1}. \tag{3.60}$$

3.2.7 Hydrodynamic Force

The hydrodynamic force used in equation 3.12 is computed in this section. Recall equation 3.31, the hydrodynamic force acting on each cell of the solid body,

$$\mathbf{F}_H^{n+1} = \int_A \left(\frac{\boldsymbol{u}^{n+1} - \boldsymbol{u}^n}{\Delta t} + \mathcal{N}\left(\boldsymbol{u}^n\right) - \boldsymbol{f}^{n+1} \right) dA,$$

where $\boldsymbol{u}^{n+1}$ are the final velocities defined in Section 3.2.6, $\boldsymbol{u}^n$ are the velocities at the previous time-step, $\mathcal{N}\left(\boldsymbol{u}^n\right)$ are the nonlinear terms calculated in Section 2.1.5, and $\boldsymbol{f}^{n+1}$ is the momentum force computed in Section 3.2.3. This equation represents the hydrodynamic force on each Lagrangian cell which is directly obtained from the Navier-Stokes equations as sum of unsteady, inertial, and momentum forcing terms without any interpolation on the surface [21]. Since this project is two-dimensional, the area of each cell is computed instead of the volume of each block as done in [21].

The Eulerian grid size is chosen to be smaller than the Lagrangian lengths Δs_1 and Δs_2 to enforce the momentum forcing inside of the solid body, to satisfy the no-slip boundary condition, and to compute the hydrodynamic force [21]. For each discrete horizontal or vertical velocity component of an Eulerian cell located inside of a Lagrangian cell, the hydrodynamic force imposed on that particular Lagrangian cell is updated.

Calculation of the area of each Lagrangian cell and determining whether a velocity component is inside a particular Lagrangian cell is done by using Heron's Formula which is outlined in Algorithm IV.

3.2.7.1 Algorithm IV

Repeat cycle for N Lagrangian cells and M Eulerian cells:

1. Calculate the edge lengths of the Lagrangian cell.

2. Calculate the length of the line segments inside the Lagrangian cell by calculating the distance from the questionable velocity component to each Lagrangian grid point. This will create four triangles inside of the Lagrangian cell.

3. Calculate the semi-perimeter of each triangle.

4. Calculate the area of each triangle which includes calculation of the four smaller triangles and the area of the two larger triangles all within the cell.

5. Sum up the four areas of the smaller triangles where
   $total_{A^{\diamond}} = A_1 + A_2 + A_3 + A_4$.

6. Add the area of the two larger triangles to calculate the actual area of the Lagrangian cell, $total_{A^{\diamond\diamond}} = A_5 + A_6$.

7. If $total_{A^{\diamond}}$ - $total_{A^{\diamond\diamond}} < 4\epsilon$, where $\epsilon \approx 2.22 \times 10^{-16}$, then the velocity component is inside of the Lagrangian cell and the hydrodynamic force can be computed for that cell.

After the hydrodynamic force is computed for each Lagrangian cell of the solid body, it is used to compute the motion equation for movement of the solid body.

3.2.8 Dynamic Motion Equation Using Finite Difference Methods

In this section, the finite difference methods used to compute the partial derivatives of the center points $\boldsymbol{X}$ of each Lagrangian cell of the solid body as well as the methods used

to compute the motion equation are explained. Recall equation 3.12,

$$\begin{aligned}
\rho \frac{\boldsymbol{X}^{n+1} - 2\boldsymbol{X}^{n} + \boldsymbol{X}^{n-1}}{\Delta t^2} &= \frac{1}{2}\sum_{a,b=1}^{2}\left[\frac{\partial}{\partial s_a}\left(K_{ab}^{T}\left(\frac{\partial \boldsymbol{X}^{n+1}}{\partial s_a}\cdot\frac{\partial \boldsymbol{X}^{n+1}}{\partial s_b} - T_{ab}^{0}\right)\frac{\partial \boldsymbol{X}^{n+1}}{\partial s_b}\right)\right] \\
&+ \frac{1}{2}\sum_{a,b=1}^{2}\left[\frac{\partial}{\partial s_a}\left(K_{ab}^{T}\left(\frac{\partial \boldsymbol{X}^{n}}{\partial s_a}\cdot\frac{\partial \boldsymbol{X}^{n}}{\partial s_b} - T_{ab}^{0}\right)\frac{\partial \boldsymbol{X}^{n}}{\partial s_b}\right)\right] \\
&+ \frac{1}{2}\frac{1}{A}\left(\mathbf{F}_{H}^{n+1} + \mathbf{F}_{H}^{n}\right).
\end{aligned}$$

The partial derivatives in the above equation, which include the tension and shearing effects, T_{ab}, are calculated, in part, using the second-order forward, backward, and centered difference methods (See figures 3.4 and 3.5). Each partial derivative is taken with respect to either s_1 or s_2.

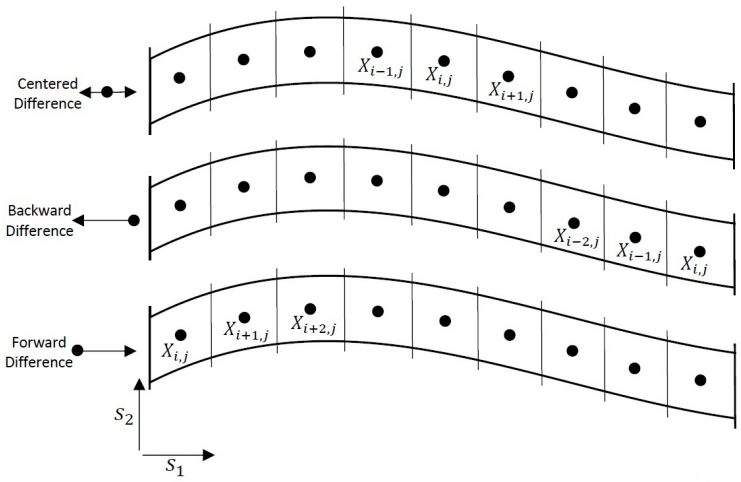

Figure 3.4: Illustration of Finite Difference Methods used to calculate the partial derivatives of the center points with respect to s_1.

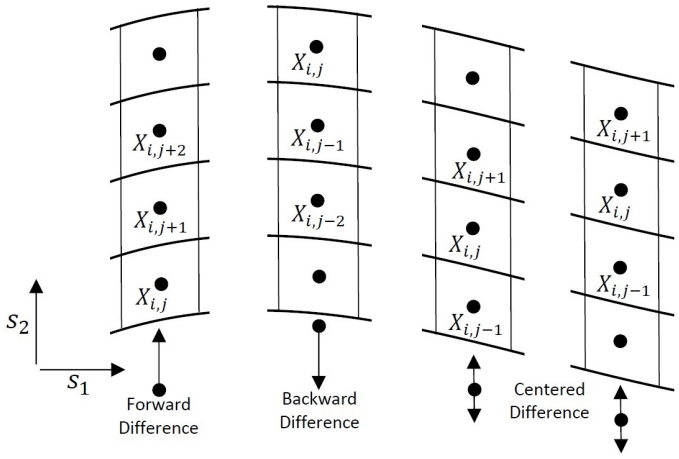

Figure 3.5: Illustration of Finite Difference Methods used to calculate the partial derivatives of the center points with respect to s_2.

In figure 3.4, if $i = 2, 3, ..., k-1$, where k is the maximum number of center points in the s_1 direction, then the second-order centered finite difference method will be used which reads,

$$\frac{\partial^2 g\left(\boldsymbol{X}_{i,j}\right)}{\partial {s_1}^2} = \frac{g\left(\boldsymbol{X}_{i+1,j}\right) - 2\,g\left(\boldsymbol{X}_{i,j}\right) + g\left(\boldsymbol{X}_{i-1,j}\right)}{\left(\Delta s_1\right)^2}, \quad \mathcal{O}\left((\Delta s_1)^2\right) \tag{3.61}$$

The second-order forward finite difference method is used if $i = 1$, and the second-order backward finite difference method is used if $i = k$. Similar steps are taken with finite difference approximations of the center points with respect to s_2 in figure 3.5.

After computing the partial derivatives of equation 3.12 using the second-order finite difference methods described above, all parts of the equation are substituted in to solve for the new location of the center points $\boldsymbol{X}$. Algorithm V describes the iterative process for solving for $\boldsymbol{X}^{n+1}$.

3.2.8.1 Algorithm V

1. Set up equation 3.12 as a system of nonlinear equations to be solved using an iterative nonlinear algebraic solver. Letting,

$$W(\boldsymbol{X}) = \frac{\partial}{\partial s_a}\left(K_{ab}^T\left(\frac{\partial \boldsymbol{X}}{\partial s_a}\cdot\frac{\partial \boldsymbol{X}}{\partial s_b} - T_{ab}^0\right)\frac{\partial \boldsymbol{X}}{\partial s_b}\right), \tag{3.62}$$

where $\boldsymbol{X} = (X, Z)^\top$, yields the system of nonlinear equations to be computed,

$$\begin{aligned} 0 &= -\rho\left(X^{n+1} - 2X^n + X^{n-1}\right) + \frac{(\Delta t)^2}{2}\left[W(X^{n+1}) + W(X^n)\right] \\ &\quad + \frac{(\Delta t)^2}{2A}\left(F_{HU}^{n+1} + F_{HU}^n\right), \end{aligned} \tag{3.63}$$

$$\begin{aligned} 0 &= -\rho\left(Z^{n+1} - 2Z^n + Z^{n-1}\right) + \frac{(\Delta t)^2}{2}\left[W(Z^{n+1}) + W(Z^n)\right] \\ &\quad + \frac{(\Delta t)^2}{2A}\left(F_{HV}^{n+1} + F_{HV}^n\right), \end{aligned} \tag{3.64}$$

where F_{HU} and F_{HV} are the hydrodynamic forces for the U and V velocities, respectively.

2. Choose an initial guess for $\boldsymbol{X}^{n+1}$.

3. Substitute initial guess for $\boldsymbol{X}^{n+1}$ into equations 3.63 and 3.64 along with the known values for $\boldsymbol{X}^n$, $\boldsymbol{X}^{n-1}$, and all other values needed. The iterative nonlinear algebraic solver will solve for the new center points, $\boldsymbol{X}^{n+1}$, outputting the Lagrangian coordinates of each point. This iterative process is done with a function tolerance of 1×10^{-8}. Note that in the initial step, let $\boldsymbol{X}^{n-1} = \boldsymbol{X}^n$ which are the values of the original Lagrangian coordinate points of the rigid body, i.e., the Lagrangian values before movement of the solid body.

After obtaining the new location of the center points of the solid body, the grid is reconstructed. In the following section, procedures for reconstruction of the Lagrangian grid, after movement of the center points of each cell, and transformation from Lagrangian coordinates to Eulerian coordinates are discussed.

3.2.9 Lagrangian Grid Reconstruction and Transformation

Lagrangian grid reconstruction and transformation of Lagrangian coordinate points to Eulerian coordinate points is necessary for visualization of the solid body in physical space. Therefore a mapping must take place from a logical representation to a physical representation of the solid body. The Lagrangian coordinates were initially defined using the distance formula and simple arithmetic on the original location of the Eulerian coordinates.

Once the new center points, $\boldsymbol{X}^{n+1}$, are computed, the old Lagrangian grid coordinates must be shifted to new Lagrangian grid coordinates to mirror the movement of the new center points. This step is done prior to transformation to the Eulerian coordinate system. Both the Lagrangian grid reconstruction and transformation to the Eulerian system is done by a mapping which is represented in figure 3.6.

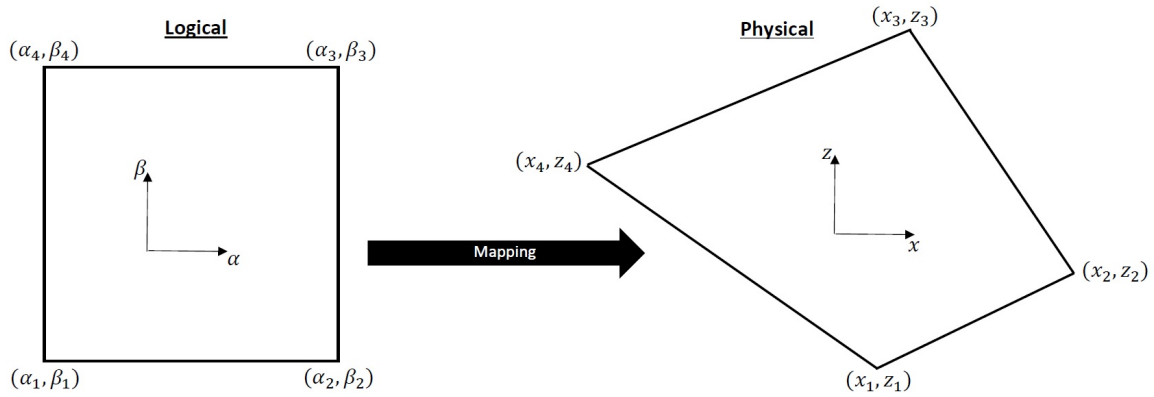

Figure 3.6: Mapping between physical and logical space.

A bilinear mapping function is created to represent the physical coordinates as logical coordinates. A general method to this mapping is described below and more detail can be found in [4]. Assume the following bilinear mapping function,

$$x = a_1 + a_2\alpha + a_3\beta + a_4\alpha\beta, \tag{3.65}$$

$$z = b_1 + b_2\alpha + b_3\beta + b_4\alpha\beta, \tag{3.66}$$

where a and b are the unknown mapping coefficients, x and z are the known physical coordinates at the n^{th} level, and α and β are the known logical coordinates at the n^{th} level. Rewriting equations 3.65 and 3.66 in matrix form yields,

$$\begin{bmatrix} x_1 \\ x_2 \\ x_3 \\ x_4 \end{bmatrix} = \begin{bmatrix} 1 & \alpha_1 & \beta_1 & \alpha_1\beta_1 \\ 1 & \alpha_2 & \beta_2 & \alpha_2\beta_2 \\ 1 & \alpha_3 & \beta_3 & \alpha_3\beta_3 \\ 1 & \alpha_4 & \beta_4 & \alpha_4\beta_4 \end{bmatrix} \begin{bmatrix} a_1 \\ a_2 \\ a_3 \\ a_4 \end{bmatrix}, \quad \begin{bmatrix} z_1 \\ z_2 \\ z_3 \\ z_4 \end{bmatrix} = \begin{bmatrix} 1 & \alpha_1 & \beta_1 & \alpha_1\beta_1 \\ 1 & \alpha_2 & \beta_2 & \alpha_2\beta_2 \\ 1 & \alpha_3 & \beta_3 & \alpha_3\beta_3 \\ 1 & \alpha_4 & \beta_4 & \alpha_4\beta_4 \end{bmatrix} \begin{bmatrix} b_1 \\ b_2 \\ b_3 \\ b_4 \end{bmatrix}. \tag{3.67}$$

Solving for the mapping coefficients by computing the inverse of the 4×4 matrix yields,

$$\begin{bmatrix} a_1 \\ a_2 \\ a_3 \\ a_4 \end{bmatrix} = \begin{bmatrix} 1 & \alpha_1 & \beta_1 & \alpha_1\beta_1 \\ 1 & \alpha_2 & \beta_2 & \alpha_2\beta_2 \\ 1 & \alpha_3 & \beta_3 & \alpha_3\beta_3 \\ 1 & \alpha_4 & \beta_4 & \alpha_4\beta_4 \end{bmatrix}^{-1} \begin{bmatrix} x_1 \\ x_2 \\ x_3 \\ x_4 \end{bmatrix}, \quad \begin{bmatrix} b_1 \\ b_2 \\ b_3 \\ b_4 \end{bmatrix} = \begin{bmatrix} 1 & \alpha_1 & \beta_1 & \alpha_1\beta_1 \\ 1 & \alpha_2 & \beta_2 & \alpha_2\beta_2 \\ 1 & \alpha_3 & \beta_3 & \alpha_3\beta_3 \\ 1 & \alpha_4 & \beta_4 & \alpha_4\beta_4 \end{bmatrix}^{-1} \begin{bmatrix} z_1 \\ z_2 \\ z_3 \\ z_4 \end{bmatrix}. \tag{3.68}$$

Once the mapping coefficients a and b are computed, the mapping from logical space to physical space is defined. The Lagrangian center points are solved for by computing equation 3.12 followed by computation of the new Lagrangian grid points by the above mapping and then transformation to the Eulerian system. Below is an outline of the mapping steps done for this project.

1. Find the mapping coefficients for the mapping from the n^{th} level Lagrangian center points to the $(n+1)^{th}$ level Lagrangian center points.

2. Use the mapping coefficients and the n^{th} level Lagrangian grid points to get the $(n+1)^{th}$ level Lagrangian grid points. Figure 3.7 shows the Lagrangian center and grid points at the n^{th} level overlapped by the Lagrangian center and grid points at the $(n+1)^{th}$ level.

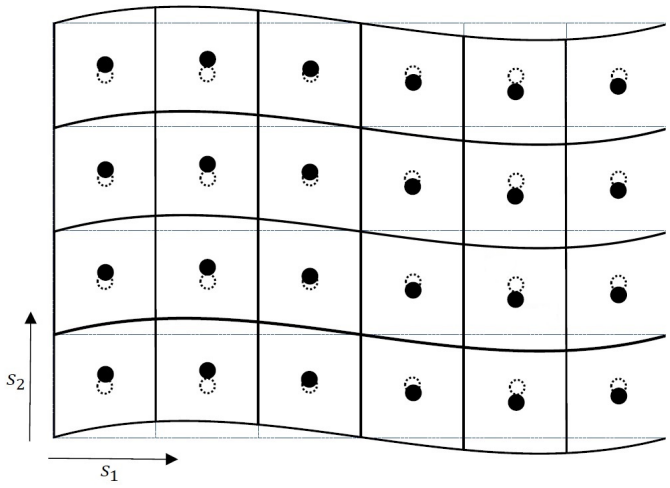

Figure 3.7: Lagrangian center and grid points at the n^{th} level (thin lines and dashed circles) overlapped by the Lagrangian center and grid points at the $(n+1)^{th}$ level (bold lines and solid circles).

3. Find the mapping coefficients for the mapping from the n^{th} level Lagrangian grid points to the n^{th} level Eulerian grid points.

4. Use the mapping coefficients from Step 3 and the $(n+1)^{th}$ level Lagrangian grid points from Step 2 to get the $(n+1)^{th}$ level Eulerian grid points.

After the mapping procedures are completed, resulting in the updated Eulerian coordinate points of the Lagrangian boundary, the velocity of the boundary can be determined. Further detail is given in Section 3.2.10.

3.2.10 Eulerian Velocities of Solid Body After Movement

In the first three projects, computations were done for a rigid boundary. This allowed for the velocities at the boundary, U_P and V_P from Section 2.1.4, to be initialized as zero and remain zero throughout the computational cycle. In this project, computations are done for a deformable boundary. This means that the solid body is free to move where its movement is caused by the no-slip boundary conditions and the hydrodynamic force. Therefore, the velocities at the boundary are no longer enforced to be zero throughout the computational cycle. Instead, these velocities are defined after the mapping of the Lagrangian coordinates to Eulerian coordinates of the solid boundary takes place.

Although there are an m amount of layers defining the Lagrangian grid for this project, the velocities of the Lagrangian grid in the Eulerian system are only needed and computed for the exterior layers of the boundary where the fluid and solid meet. The velocities of the mapped Lagrangian grid points to Eulerian space, defined as Ex and Ez, are computed using the second-order backwards finite difference method in time yielding,

$$(Ex)^n = \frac{3(Xe)^n - 4\,(Xe)^{n-1} + (Xe)^{n-2}}{2\Delta t}, \quad \mathcal{O}\left((\Delta t)^2\right) \tag{3.69}$$

$$(Ez)^n = \frac{3(Ze)^n - 4\,(Ze)^{n-1} + (Ze)^{n-2}}{2\Delta t}, \quad \mathcal{O}\left((\Delta t)^2\right) \tag{3.70}$$

where (Xe, Ze) represents the Eulerian coordinates of the Lagrangian boundary transformed from the Lagrangian grid to Eulerian space.

After these values are calculated, U_P and V_P are calculated where these values are defined for each Eulerian boundary cell. Consider the illustration in figure 3.8.

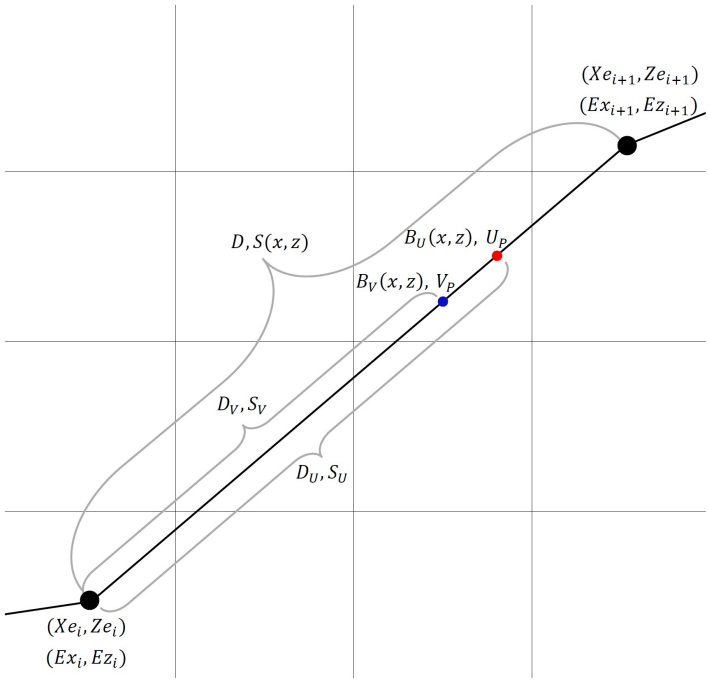

Figure 3.8: Illustration of points needed to define U_P and V_P.

Let $B_U(x,z)$ and $B_V(x,z)$ (explained in Section 2.1.3) represent the new U and V boundary points to be used in each Eulerian cell along the immersed boundary. Then for S representing the difference of Eulerian velocities in the x and z directions and for D representing the distance between two points on the boundary, the following equations for linear interpolation of the velocities U_P and V_P on the immersed boundary are,

$$\frac{D_U}{D} = \frac{S_U}{S(x)} \tag{3.71}$$

$$\frac{D_V}{D} = \frac{S_V}{S(z)}. \tag{3.72}$$

where,

$$D = \sqrt{(Xe_{i+1} - Xe_i)^2 + (Ze_{i+1} - Ze_i)^2} \tag{3.73}$$

$$D_U = \sqrt{(B_U(x) - Xe_i)^2 + (B_U(z) - Ze_i)^2} \tag{3.74}$$

$$D_V = \sqrt{(B_V(x) - Xe_i)^2 + (B_V(z) - Ze_i)^2} \tag{3.75}$$

$$S_U = U_P - Ex_i \tag{3.76}$$

$$S_V = V_P - Ez_i \tag{3.77}$$

$$S(x) = Ex_{i+1} - Ex_i \tag{3.78}$$

$$S(z) = Ez_{i+1} - Ez_i. \tag{3.79}$$

Substituting equations 3.73 - 3.79 into their respective positions of equations 3.71 and 3.72 yields,

$$\frac{\sqrt{(B_U(x) - Xe_i)^2 + (B_U(z) - Ze_i)^2}}{\sqrt{(Xe_{i+1} - Xe_i)^2 + (Ze_{i+1} - Ze_i)^2}} = \frac{U_P - Ex_i}{Ex_{i+1} - Ex_i}, \tag{3.80}$$

$$\frac{\sqrt{(B_V(x) - Xe_i)^2 + (B_V(z) - Ze_i)^2}}{\sqrt{(Xe_{i+1} - Xe_i)^2 + (Ze_{i+1} - Ze_i)^2}} = \frac{V_P - Ez_i}{Ez_{i+1} - Ez_i}. \tag{3.81}$$

Solving for U_P and V_P produces the following two equations,

$$U_P = (Ex_{i+1} - Ex_i) \frac{\sqrt{(B_U(x) - Xe_i)^2 + (B_U(z) - Ze_i)^2}}{\sqrt{(Xe_{i+1} - Xe_i)^2 + (Ze_{i+1} - Ze_i)^2}} + Ex_i, \tag{3.82}$$

$$V_P = (Ez_{i+1} - Ez_i) \frac{\sqrt{(B_V(x) - Xe_i)^2 + (B_V(z) - Ze_i)^2}}{\sqrt{(Xe_{i+1} - Xe_i)^2 + (Ze_{i+1} - Ze_i)^2}} + Ez_i. \tag{3.83}$$

Once U_P and V_P are computed for each Eulerian cell defining the immersed boundary, these values are used in equations 2.47, 2.49, 2.51, and 2.53 to interpolate what the exterior neighboring velocities of the fluid need to be in the horizontal and vertical directions as the fluid approaches the boundary (See figures 2.7, 2.8, 2.9, and 2.10 in Section 2.1.4.) From this point, the momentum forcing terms can be computed in Section 3.2.3.

In the next chapter, results of this project are presented. The U and V velocities are displayed using a meshed grid where the color bar will define the intensity of the velocities at each part of the grid defining the cerebral artery and adjoining aneurysm surrounded by interior and exterior fluids.

Chapter 4

NUMERICAL RESULTS

Figures 4.1-4.8 simulate the U and V velocity profiles of pulsatile blood flow through a rigid cerebral artery with an adjoining rigid saccular aneurysm. Figures 4.9-4.30 simulate the U and V velocity profiles of pulsatile blood flow through an elastic cerebral artery with an adjoining elastic saccular aneurysm. The following parameters used to run this simulation are: $\rho_S = 1160$, $\rho_F = 1060$, $\mu = 2.78 \times 10^{-3}$, $u_{max} \approx 7.958 \times 10^{-1}$, $K_{11} = K_{22} = 9 \times 10^{-3}$, $K_{12} = K_{21} = 5 \times 10^{-3}$, $D = 2.6 \times 10^{-3}$ scaled to $D = 1$, $Th = 1 \times 10^{-1}$, $Lg = 4$ which is the number layers of the Lagrangian grid in the s_2 direction for both the top and bottom of the artery, $s_1 = 116$ for the top boundary which includes the aneurysm wall, $s_1 = 89$ for the bottom of the artery wall, $L_x = 16 \times 10^{-3}$ scaled by D to $L_x \approx 6.1538$, $L_z = 14 \times 10^{-3}$ scaled by D to $L_z \approx 5.3846$, $n_z = 1600$, $n_x = 1000$, $Re \approx 7.8898 \times 10^2$, $\Delta x \approx 6.1538 \times 10^{-3}$, $\Delta z \approx 3.3654 \times 10^{-3}$, $\Delta t = 5 \times 10^{-4}$ s, and $NT = 6000$. Note the changes in the color-bar for each figure at each time-step.

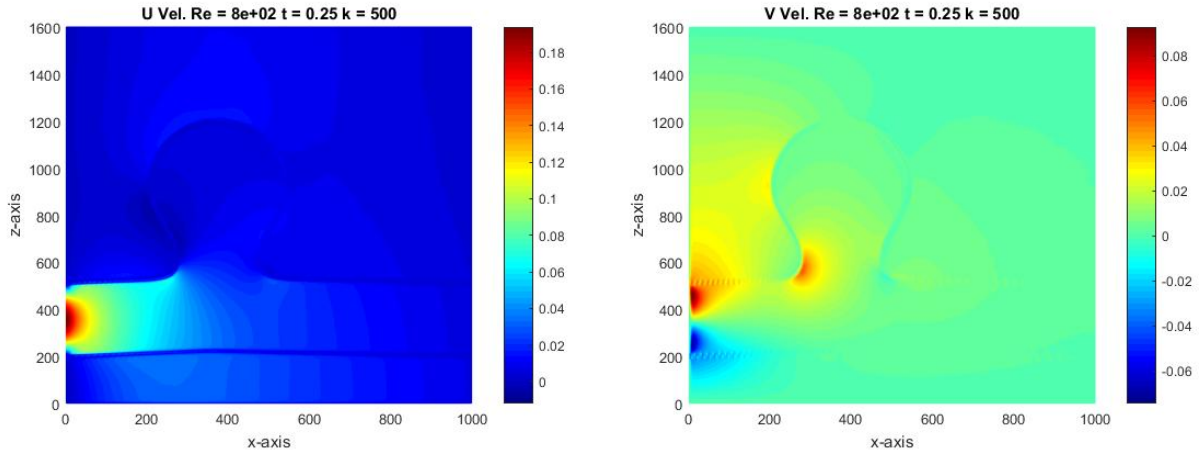

Figure 4.1: (a) U and (b) V velocity profile at $t = 0.25$ s, $u_{\max} \approx 7.7537 \times 10^{-1}$ m/s

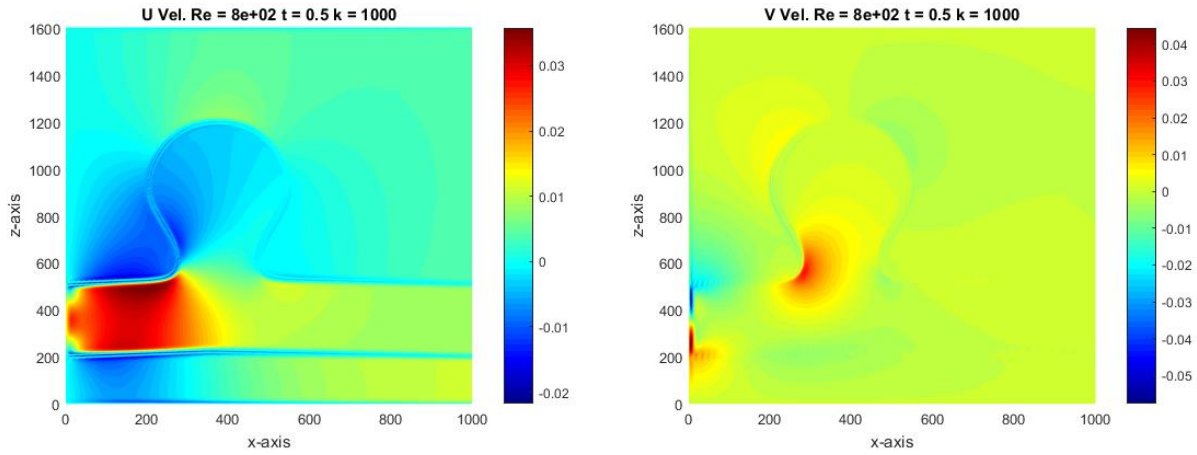

Figure 4.2: (a) U and (b) V velocity profile at $t = 0.5$ s, $u_{\max} = 5.3618 \times 10^{-2}$ m/s

Figures 4.1-4.8 define the artery and aneurysm at a rigid state. Computations of the boundary at a rigid state are done in order to obtain a defined boundary prior to movement. This is done for two complete time cycles ending at $t = 2$ s. Once this process presents stable results, the boundary is released to move which can be seen in figures 4.9-4.30.

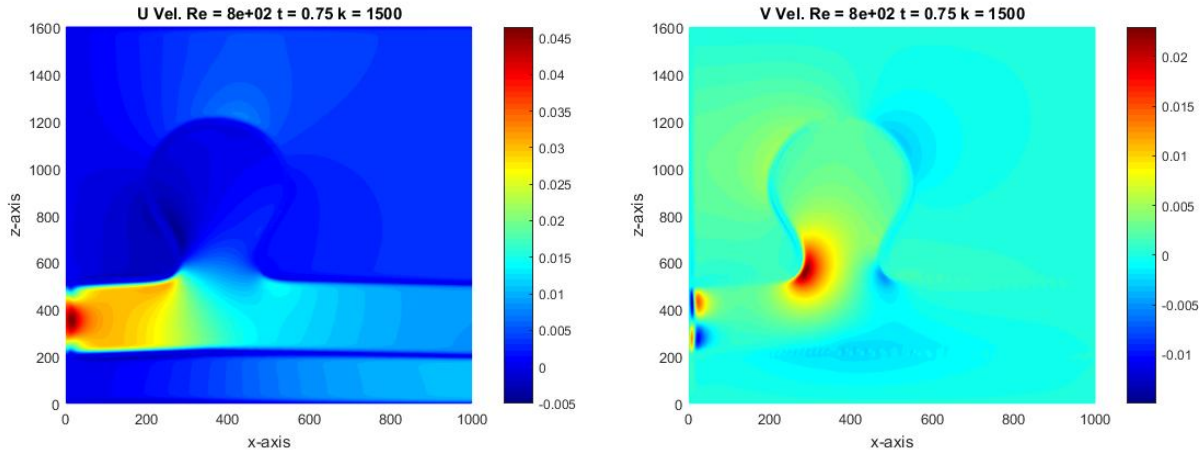

Figure 4.3: (a) U and (b) V velocity profile at $t = 0.75$ s, $u_{\max} \approx 1.6758 \times 10^{-1}$ m/s

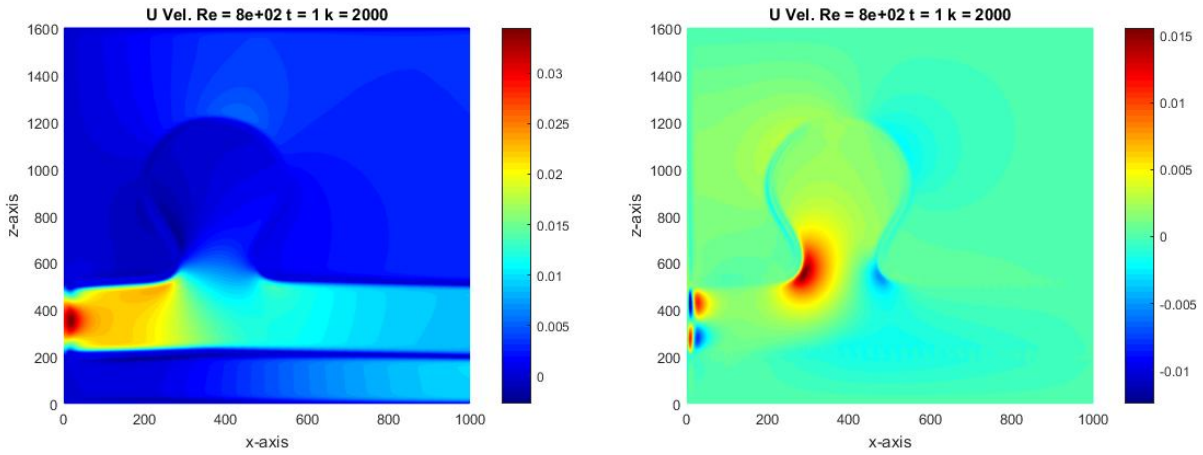

Figure 4.4: (a) U and (b) V velocity profile at $t = 1$ s, $u_{\max} \approx 1.2009 \times 10^{-1}$ m/s

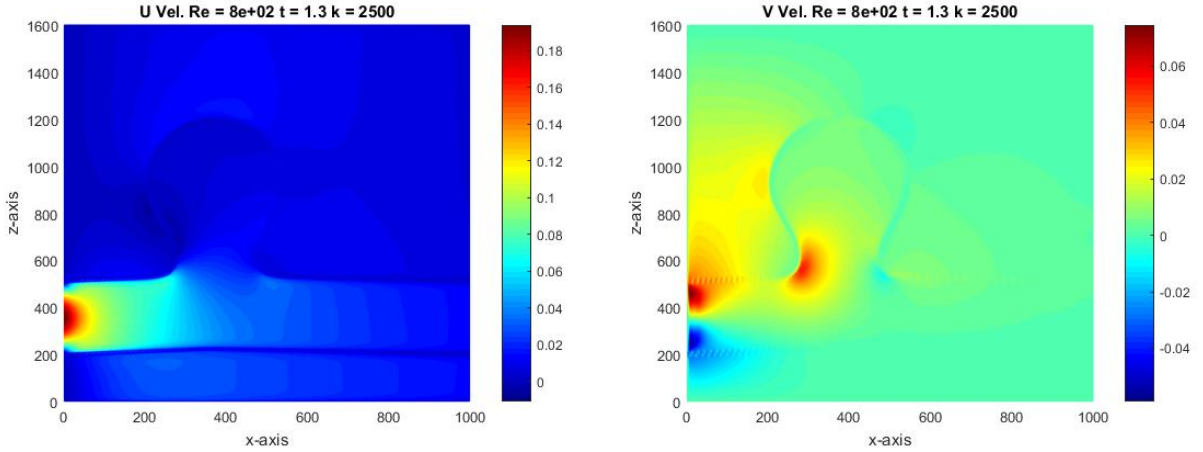

Figure 4.5: (a) U and (b) V velocity profile at $t = 1.3$ s, $u_{\max} \approx 7.7537 \times 10^{-1}$ m/s

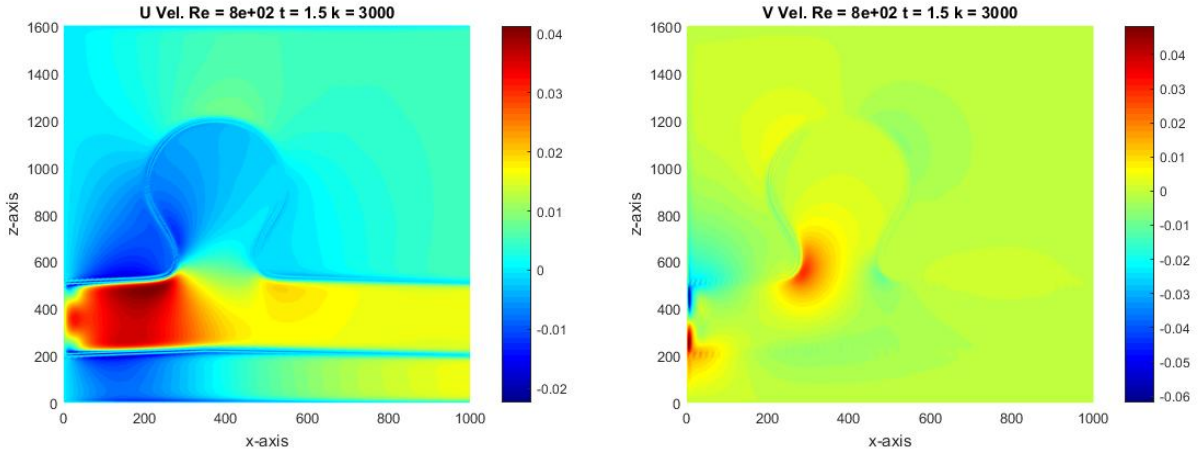

Figure 4.6: (a) U and (b) V velocity profile at $t = 1.5$ s, $u_{\max} \approx 5.3612 \times 10^{-2}$ m/s

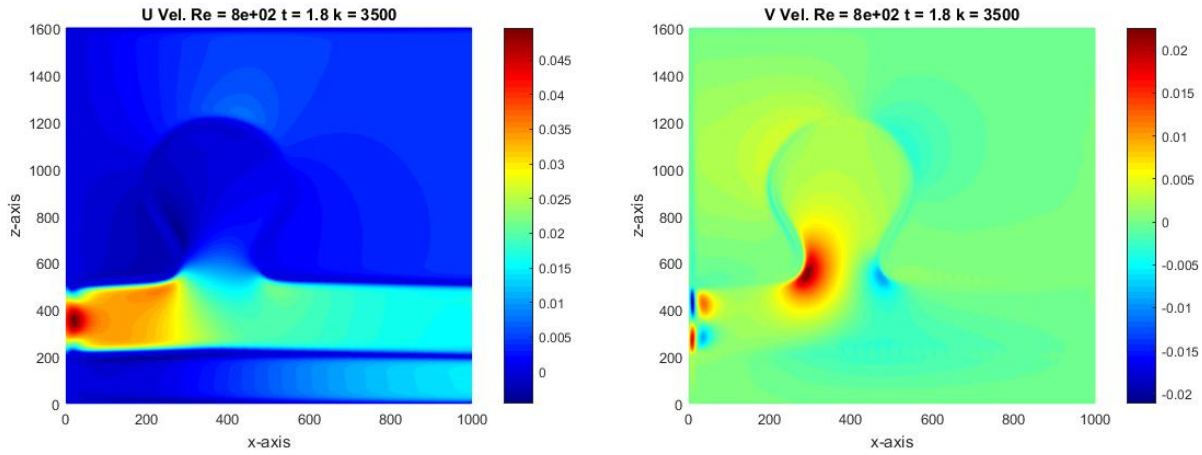

Figure 4.7: (a) U and (b) V velocity profile at $t = 1.8$ s, $u_{\max} \approx 1.6758 \times 10^{-1}$ m/s

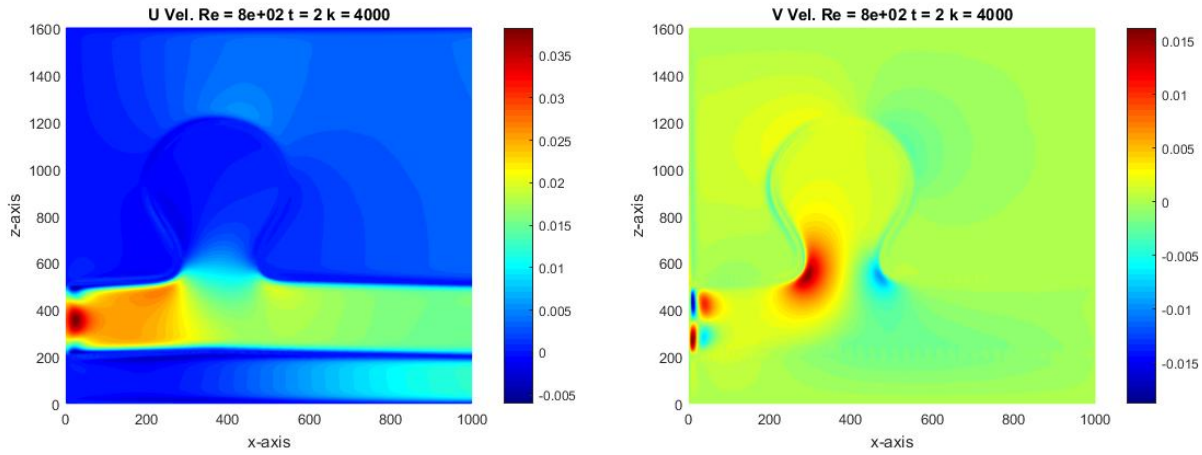

Figure 4.8: (a) U and (b) V velocity profile at $t = 2$ s, $u_{\max} \approx 1.2009 \times 10^{-1}$ m/s

After the boundary is initialize and seen by the fluid, the boundary is now released to move. Figure 4.9 represents the movement of the boundary at $t = 2.05$ seconds. Note that the movement is not obvious at this early stage.

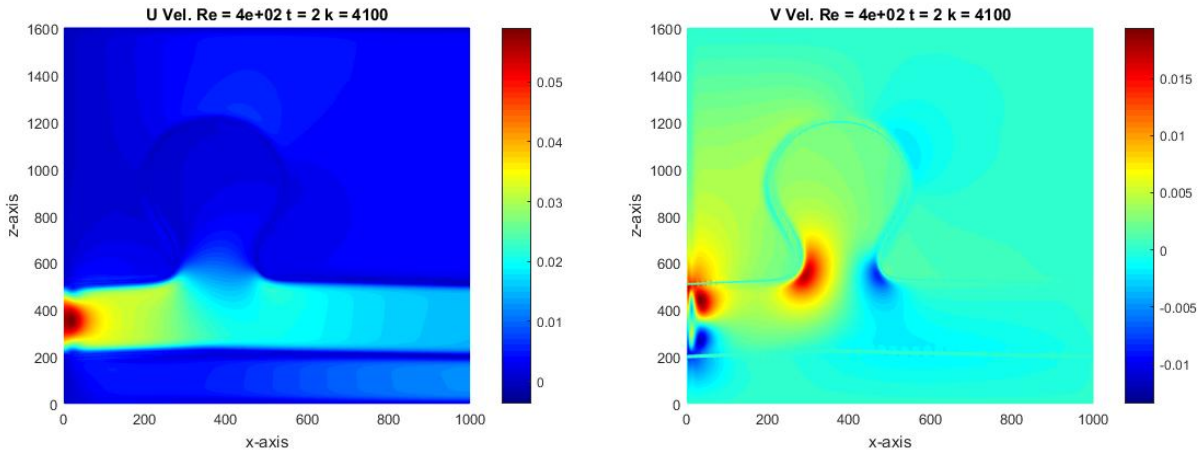

Figure 4.9: (a) U and (b) V velocity profile at $t = 2.05$ s, $u_{\max} \approx 2.3163 \times 10^{-1}$ m/s

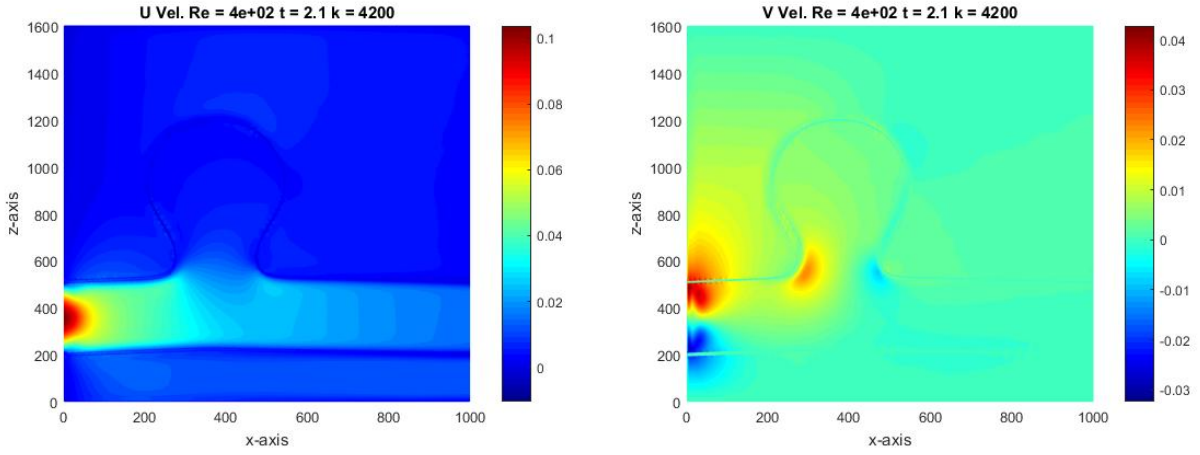

Figure 4.10: (a) U and (b) V velocity profile at $t = 2.1$ s, $u_{\max} \approx 4.1587 \times 10^{-1}$ m/s

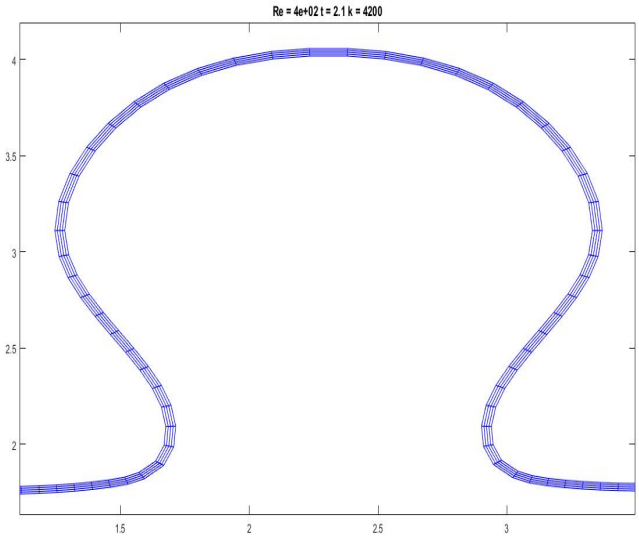

Figure 4.11: The aneurysm at $t = 2$ s (red lines) versus $t = 2.1$ s (blue lines, not quite visible).

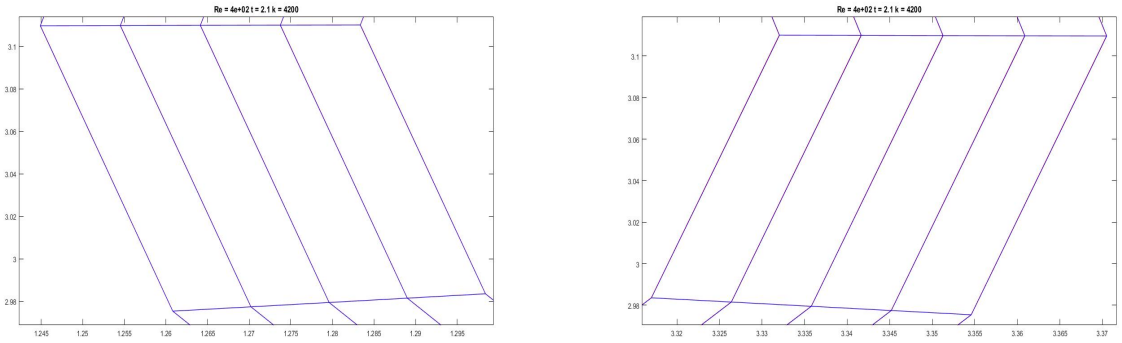

Figure 4.12: (a) The proximal and (b) distal side of the aneurysm at $t = 2$ s (red lines) versus $t = 2.1$ s (blue lines, not quite visible).

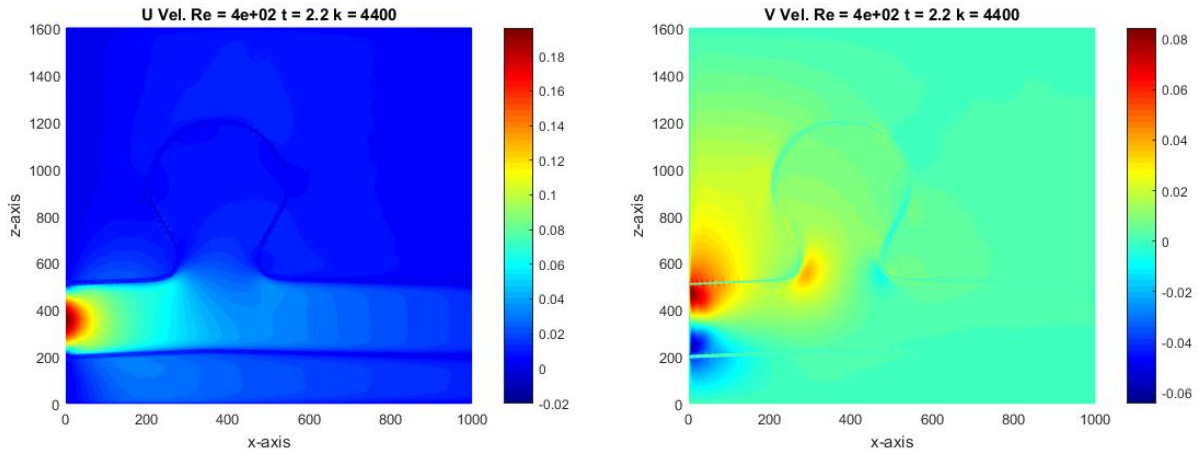

Figure 4.13: (a) U and (b) V velocity profile at $t = 2.2$ s, $u_{\max} \approx 7.8563 \times 10^{-1}$ m/s

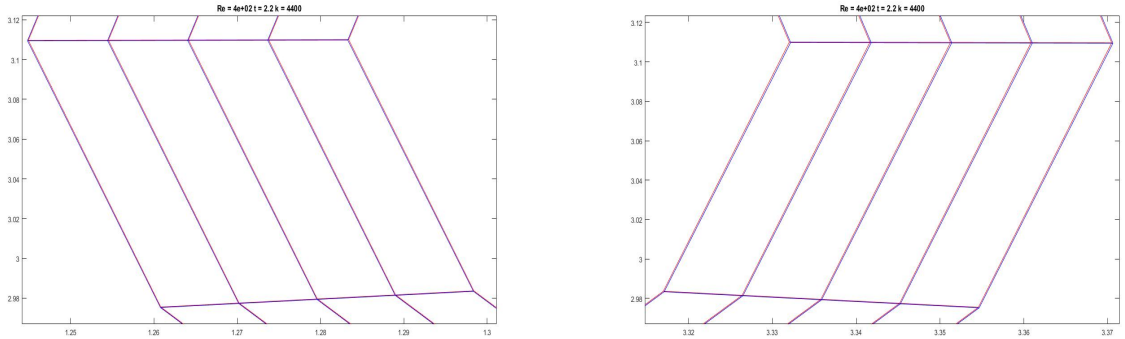

Figure 4.14: (a) The proximal and (b) distal side of the aneurysm at $t = 2$ s (red lines) versus $t = 2.2$ s (blue lines).

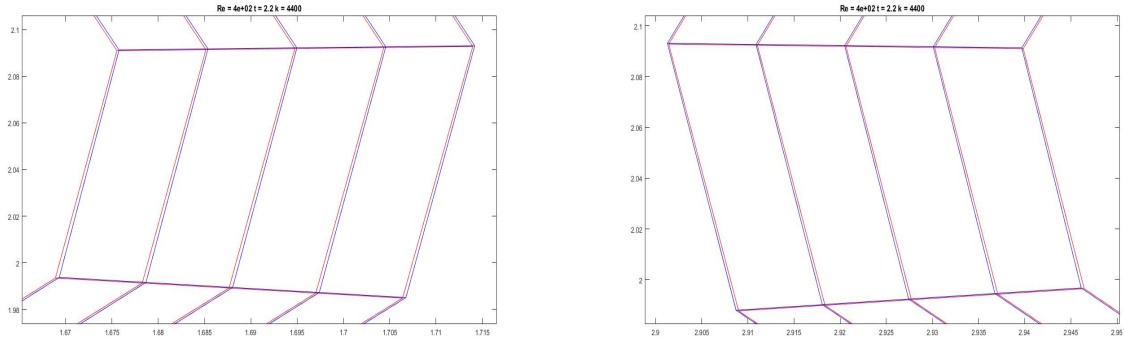

Figure 4.15: (a) The proximal and (b) distal side of the ostium (neck) at $t = 2$ s (red lines) versus $t = 2.2$ s (blue lines).

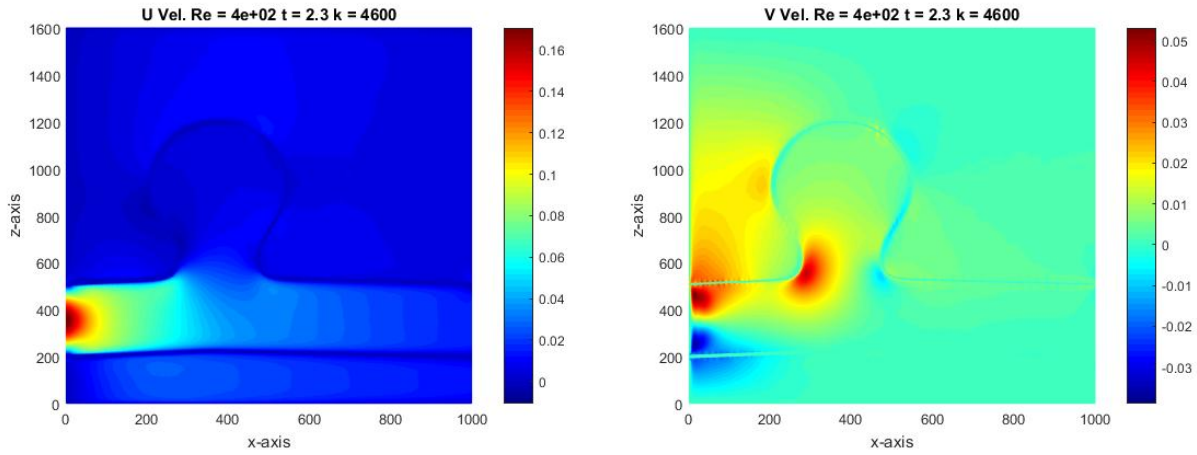

Figure 4.16: (a) U and (b) V velocity profile at $t = 2.3$ s, $u_{\max} \approx 6.8165 \times 10^{-1}$ m/s

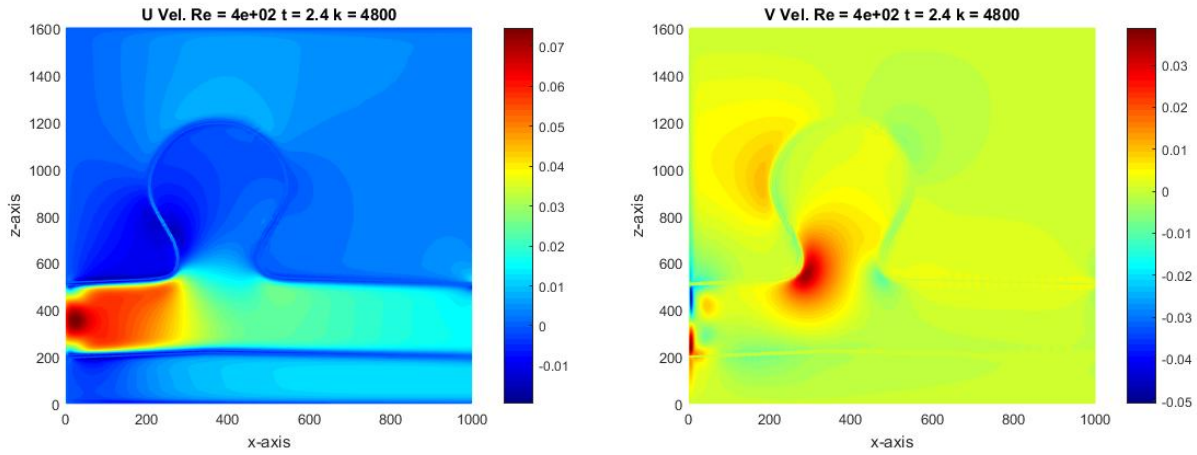

Figure 4.17: (a) U and (b) V velocity profile at $t = 2.4$ s, $u_{\max} \approx 2.5242 \times 10^{-1}$ m/s

In figure 4.17(a), discoloration at the left side of the aneurysm (the light blue region) represents movement at approximately 1×10^{-2} m/s. This movement is caused by a vortex that is beginning to take place as the fluid is being pushed to that side of the aneurysm as it pushes off of the right side of the aneurysm.

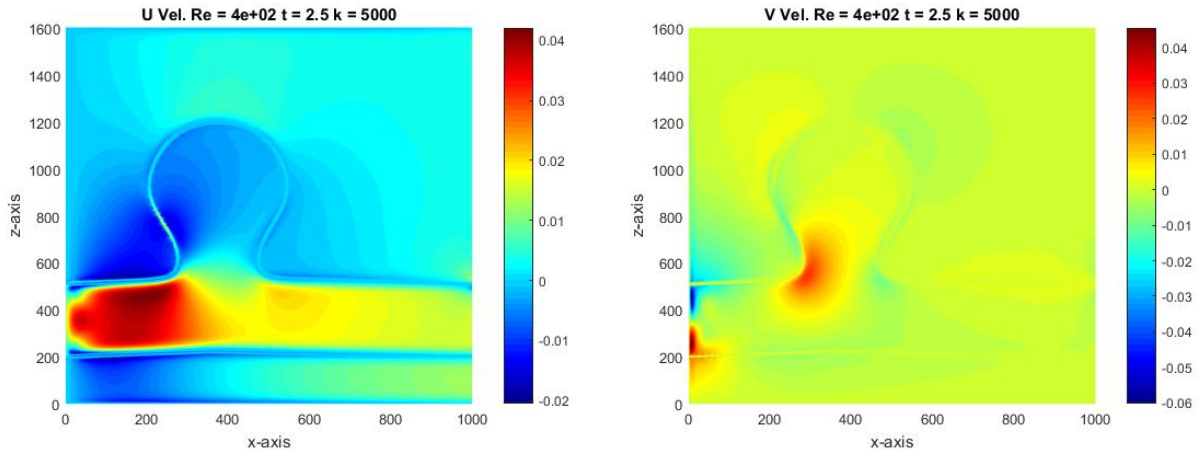

Figure 4.18: (a) U and (b) V velocity profile at $t = 2.5$ s, $u_{\max} \approx 5.3618 \times 10^{-2}$ m/s

In figure 4.18(a), the velocity of the proximal side of the aneurysm is becoming more intense resulting in a peak velocity of approximately 1.75×10^{-2} m/s.

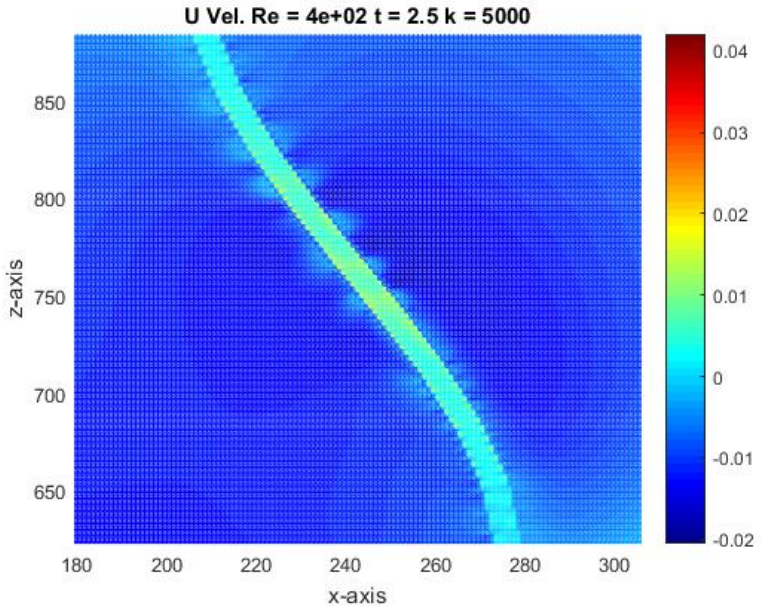

Figure 4.19: (a) Magnification of proximal region of the aneurysm at $t = 2.5$ s

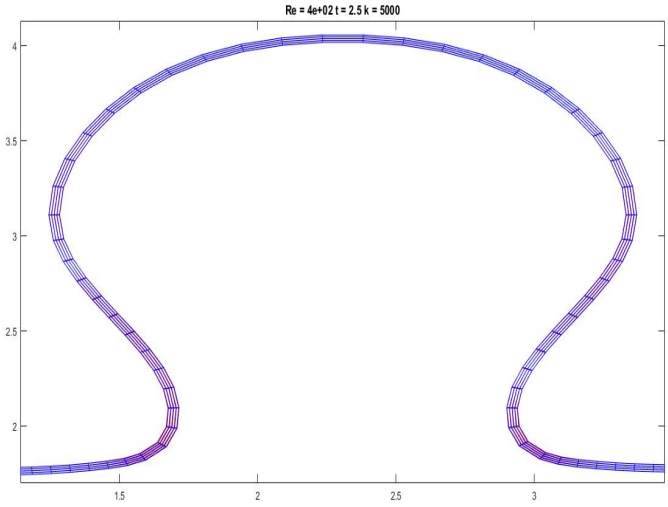

Figure 4.20: The aneurysm at $t = 2$ s (red lines) versus $t = 2.5$ s (blue lines).

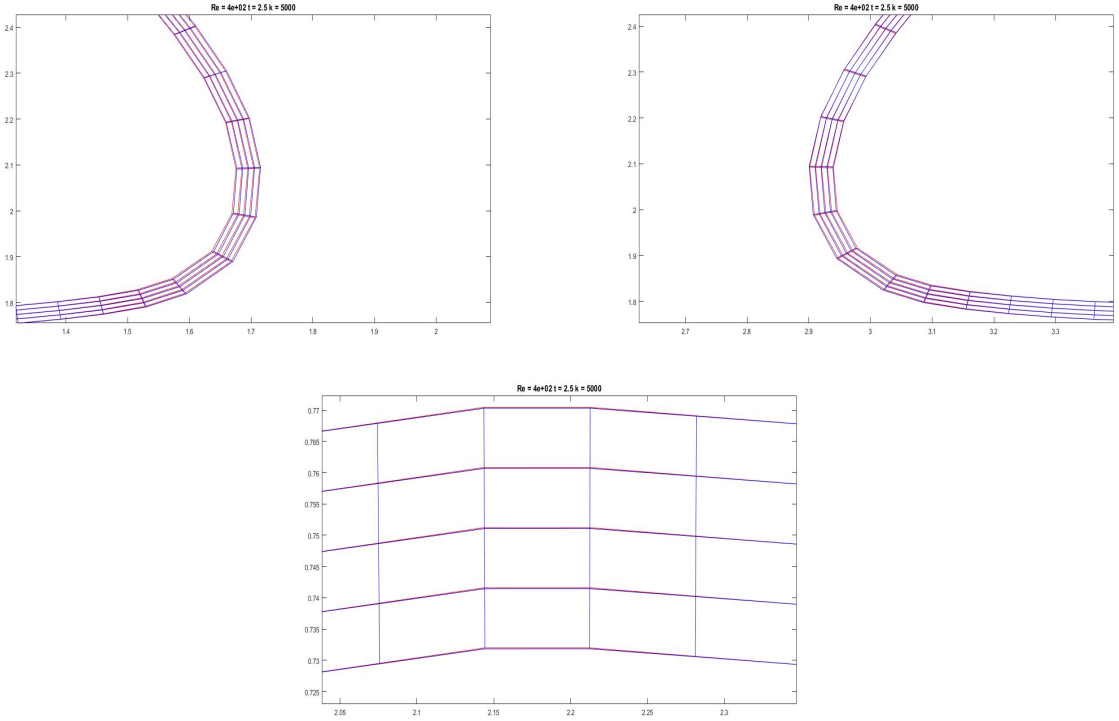

Figure 4.21: Magnification of (a) the proximal side of the ostium (neck); (b) the distal side of the ostium (neck); (c) the middle region of the bottom of artery at $t = 2$ s.

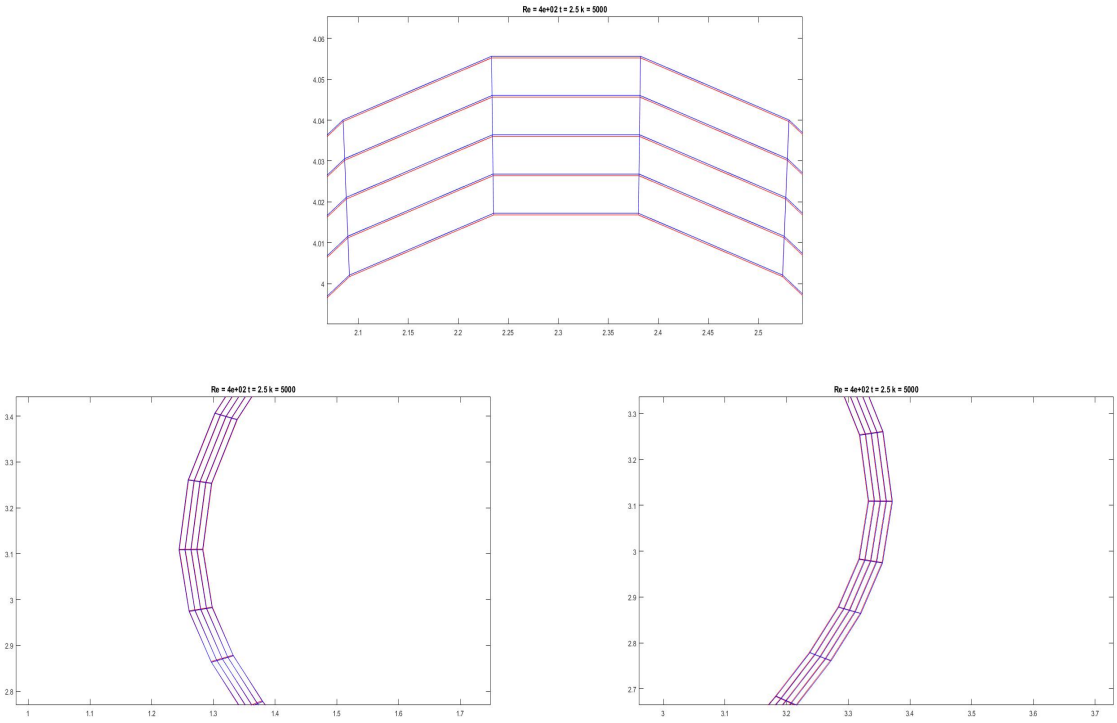

Figure 4.22: Magnification of (a) the top of the aneurysm; (b) the proximal side of the aneurysm; (c) the distal side of the aneurysm at $t = 2$ s.

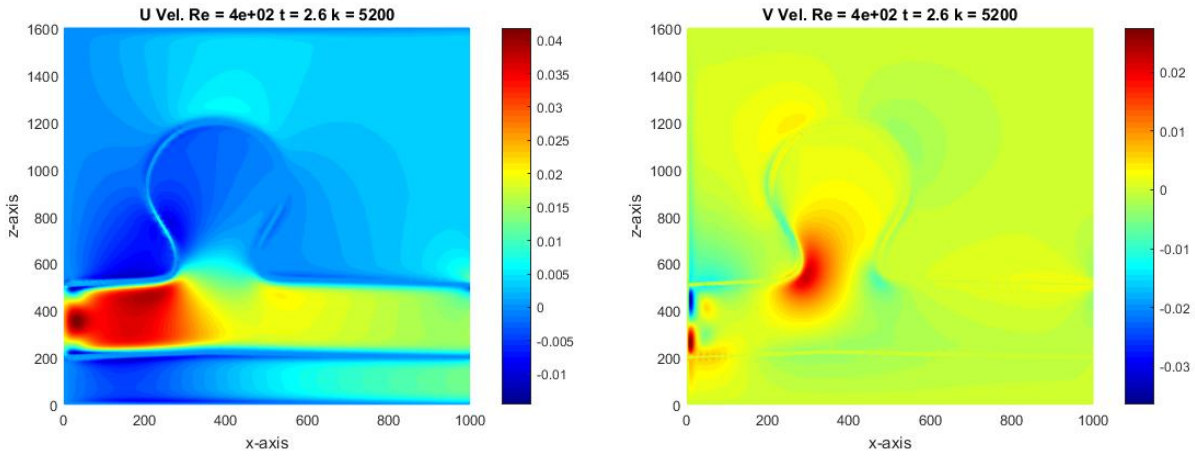

Figure 4.23: (a) U and (b) V velocity profile at $t = 2.6$ s, $u_{\max} \approx 1.0828 \times 10^{-1}$ m/s

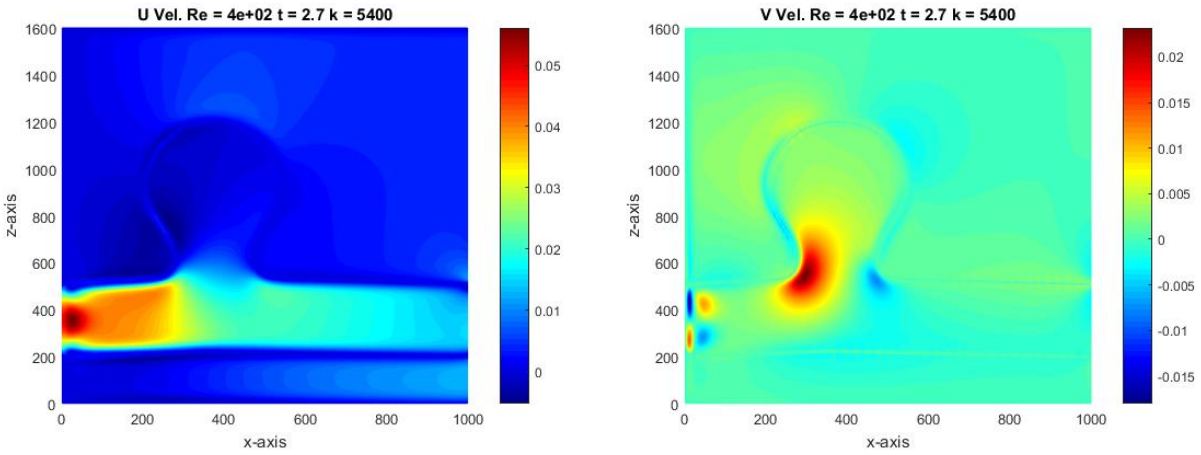

Figure 4.24: (a) U and (b) V velocity profile at $t = 2.7$ s, $u_{\max} \approx 1.9438 \times 10^{-1}$ m/s

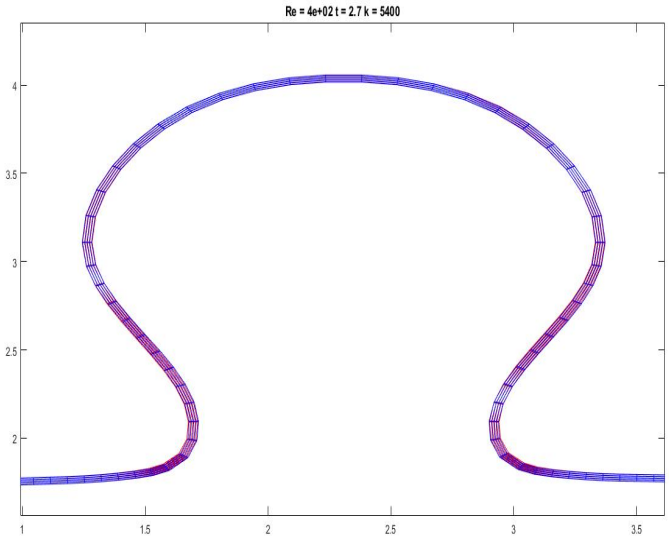

Figure 4.25: The aneurysm at $t = 2$ s (red lines) versus $t = 2.7$ s (blue lines).

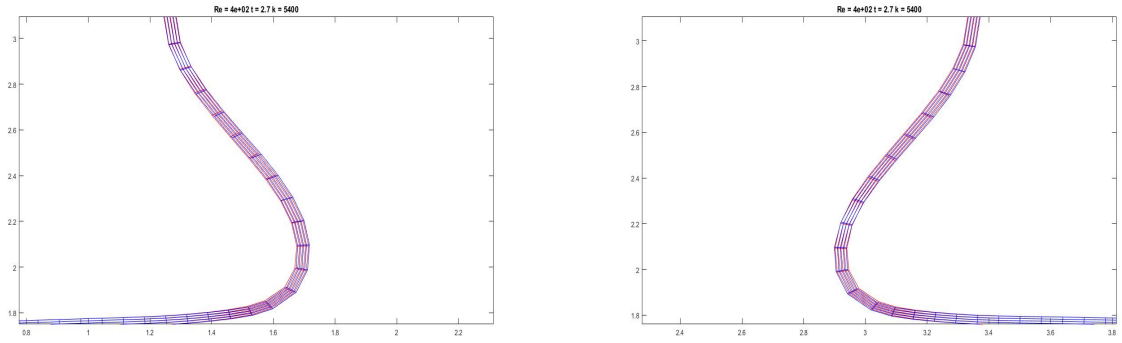

Figure 4.26: (a) The proximal and (b) distal side of the ostium leading up to the aneurysm at $t = 2$ s (red lines) versus $t = 2.7$ s (blue lines).

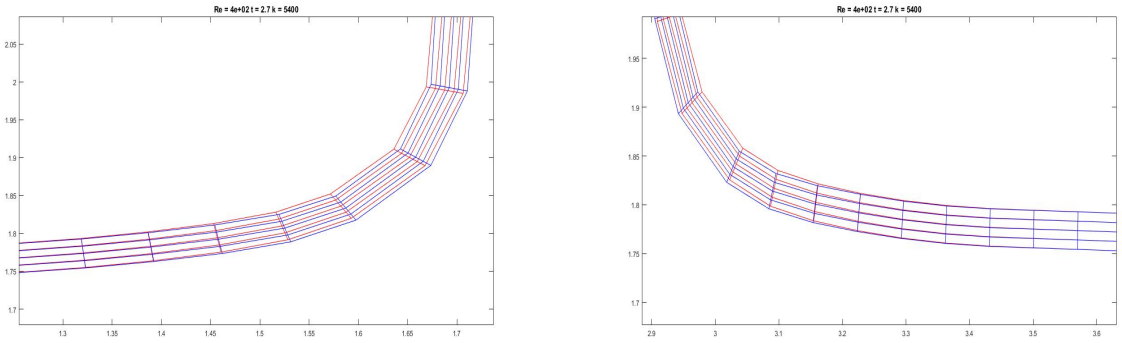

Figure 4.27: (a) The proximal side of the top artery wall leading up to the ostium and (b) the distal side of the ostium leading down to the artery wall at $t = 2$ s (red lines) versus $t = 2.7$ s (blue lines).

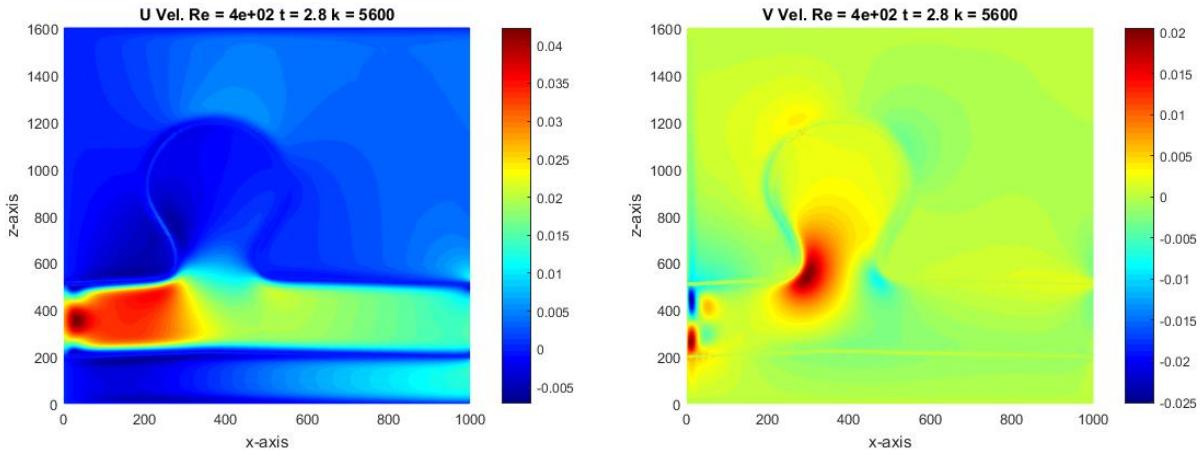

Figure 4.28: (a) U and (b) V velocity profile at $t = 2.8$ s, $u_{\max} \approx 1.1657 \times 10^{-1}$ m/s

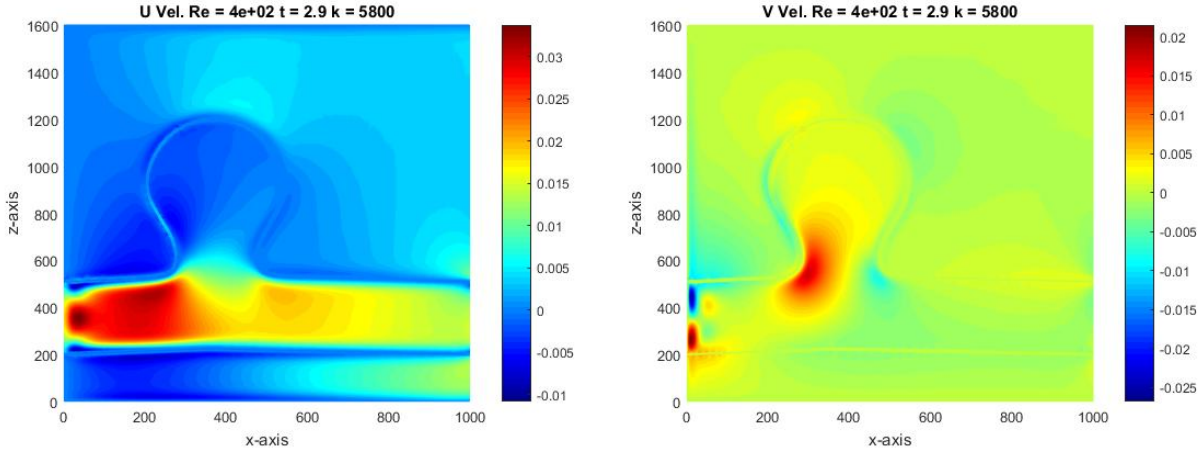

Figure 4.29: (a) U and (b) V velocity profile at $t = 2.9$ s, $u_{\max} \approx 7.4527 \times 10^{-2}$ m/s

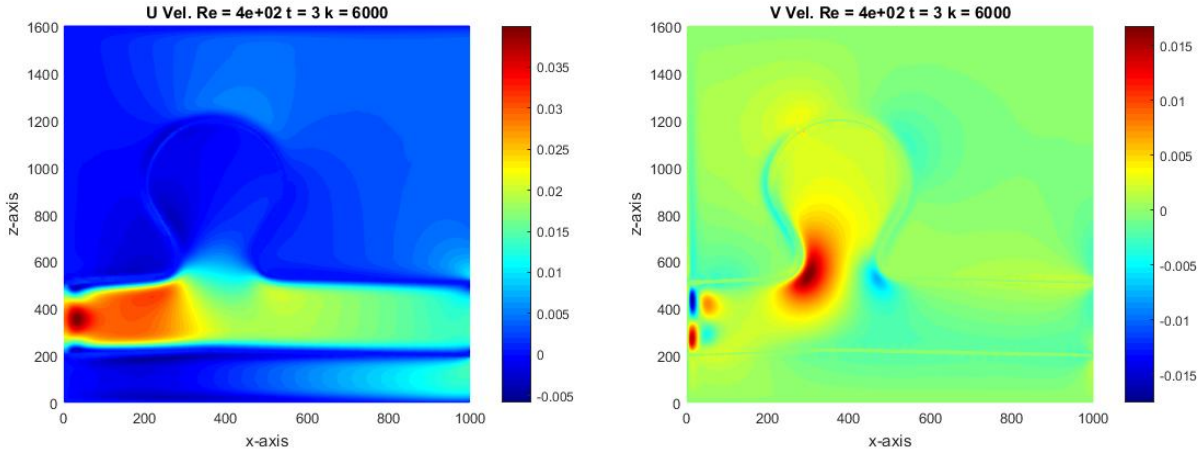

Figure 4.30: (a) U and (b) V velocity profile at $t = 3$ s, $u_{\max} \approx 1.2009 \times 10^{-1}$ m/s

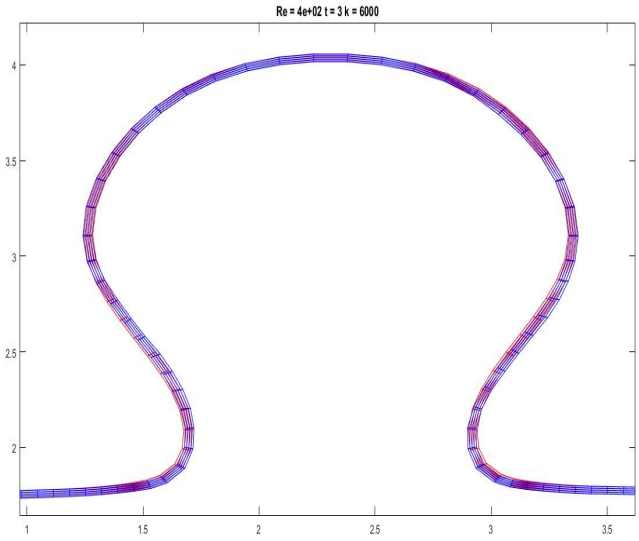

Figure 4.31: The aneurysm at $t = 2$ s (red lines) versus $t = 3$ s (blue lines).

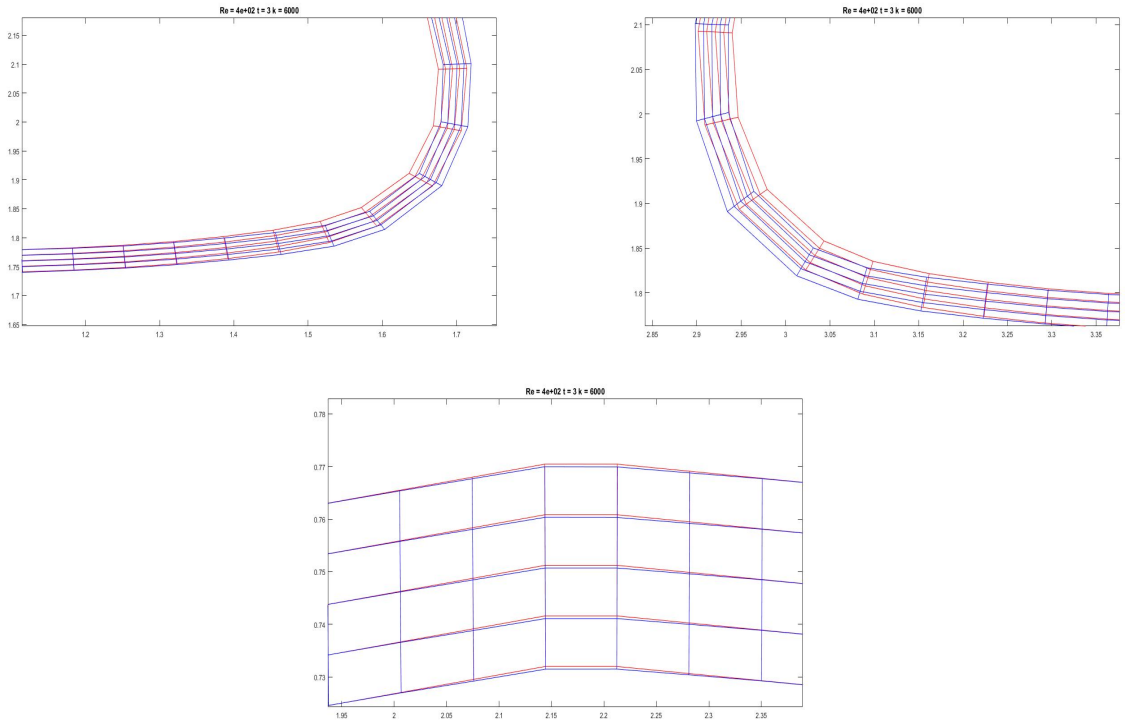

Figure 4.32: (a) The proximal side of the top artery wall leading up to the ostium,(b) the distal side of the ostium leading down to the artery wall and (c) the middle region of the bottom of artery at $t = 2$ s (red lines) versus $t = 3$ s (blue lines).

All figures, displayed in this chapter, represent the simulation of a deformable cerebral artery and adjoining saccular aneurysm as interior and exterior forces were enforced. One may consider increasing the grid size and decreasing the time step which will allow the boundary to be defined much quicker resulting in less movement of exterior fluid from the initial effects of x-velocities prior to boundary enforcement.

Also, increasing the tension and shearing constants will result in a more flexible boundary where the arterial and aneurysmal walls will be allowed to move more freely. Decreasing the shearing and tension constants will result in more resistance of arterial and aneurysmal wall movement from the effects of the interior and exterior fluid forces.

Chapter 5

CONCLUSION

In the first project, presented in Section 2.1, laminar flow of water was simulated through a rigid cylinder around a rigid circular solid. An immersed boundary method was applied to handle the solid body. The two-dimensional incompressible Navier-Stokes equations, which governs the flow of the fluid, were solved on a staggered Eulerian grid. The numerical code was verified through the results obtained and then modified to solve for flow through an artery with an adjoining rigid saccular aneurysm.

The second project, presented in Section 2.2, demonstrated laminar flow of blood through a rigid cerebral artery with an adjoining rigid saccular aneurysm. The same methods in the first project were used in this project in order to compute the two-dimensional incompressible Navier-Stokes equations. The only modification made was the change of the immersed boundary from a rigid circular solid to a rigid artery with its adjoining saccular aneurysm. The results obtained were qualitatively in agreement with results in Lott et al.'s paper [24].

In the third project, presented in Section 2.3, modifications were made to the second project to simulate pulsatile flow of blood through the rigid artery and aneurysm. This was done by introducing a fast Fourier transform in order to approximate the inlet blood flow at the entrance of the artery. Results showed that blood remained inside the inflow domain as it pulsated through, i.e., there was no leakage outside of the flow domain.

After stable results from all three projects, the fourth and final project was able to be simulated. In this project, pulsatile blood flow through a deformable artery and adjoining saccular aneurysm was simulated. This introduced the dynamic equation for the motion of an elastic body which was solved in the Lagrangian coordinate system using the Crank-Nicolson method, and the Navier-Stokes equations were solved in the Eulerian coordinate

system as done in the previous projects. The coupling of these two sets of equations allowed for movement of the artery and saccular aneurysm at each time step with respect to the flow of the blood and the forces that the blood imposed on the boundary.

This dissertation presented a unique combination of studies done by Mori and Peskin, Seibold, Lee and Choi, and Ghaffari et al. to create fluid-structure interaction using a finite-difference, immersed boundary method to simulate blood flow through a cerebral artery and its adjoining saccular aneurysm. A semi-implicit numerical code solving the two-dimensional nonlinear incompressible Navier-Stokes equations was created similar to that of work done by Seibold who presented the lid driven cavity problem, and simulations of laminar and pulsatile blood flow through the rigid cerebral artery and its adjoining aneurysm were simulated. Then with the aid of Mori and Peskin's [30] and Lee and Choi's [21] work, success in coupling the two-dimensional Navier-Stokes equations with the equation of motion for an elastic body was achieved to simulate blood–aneurysm vessel interaction.

As done by Ghaffari et al. [9], a Lagrangian structured grid covered the deformable aneurysm and artery walls which was coupled with the surrounding fluid by hydrodynamic forces calculated on the Eulerian grid. Unlike Di and Ge [7] who solved Poisson's equation for pressure before computing the body force, in this research, the force was calculated prior to solving Poisson's equation for the pressure. The same results were achieved where a divergence-free flow field in the fluid domain and no-slip boundary conditions on the immersed boundary were produced.

This work validated the lid driven cavity problem presented by Seibold [34] (not pictured), flow around a circular solid, Poiseuille flow and pulsatile flow through a rigid aneurysm. The novelty and major contribution of this work is that it uniquely tracks free surfaces by using second-order finite difference methods to compute the velocity of surface cells. This work also uses a mapping technique to transform and restore the location of the deformable body in Eulerian space.

Results of all four projects demonstrated that the immersed boundary method used and the coupling of the two-dimensional incompressible Navier-Stokes with the dynamic equation for the motion of an elastic body are potential tools for simulations involving fluid-solid interactions on both rigid and elastic boundaries. Stability, accuracy, and consistency of the results of the fourth project allows for modifications to be taken into consideration on a quantitative basis proposed in Chapter 6, Future Work.

Chapter 6

FUTURE WORK

Future work includes checking if the present model gives a non-zero pressure field even though the velocity is near zero. Also, modification of the numerical code from two-dimensions to three-dimensions using the three dimensional Navier-Stokes equations as follows,

$$U_t = -(U^2)_x - (UW)_y - (UV)_z + \frac{1}{Re}(U_{xx} + U_{yy} + U_{zz}) - P_x + F_U \tag{6.1}$$

$$W_t = -(UW)_x - (W^2)_y - (VW)_z + \frac{1}{Re}(W_{xx} + W_{yy} + W_{zz}) - P_y + F_W \tag{6.2}$$

$$V_t = -(UV)_x - (VW)_y - (V^2)_z + \frac{1}{Re}(V_{xx} + V_{yy} + V_{zz}) - P_z + F_V \tag{6.3}$$

$$U_x + W_y + V_z = 0, \tag{6.4}$$

coupled with the three-dimensional motion equation where the volume of each block will be incorporated and the bending and twisting effects will take into effect resulting in the following equation,

$$\rho\frac{\partial^2 \boldsymbol{X}}{\partial t^2} = \sum_{a,b=1}^{2}\left[\frac{\partial}{\partial s_a}\left(K_{ab}^{T}\left(T_{ab} - T_{ab}^{0}\right)\frac{\partial \boldsymbol{X}}{\partial s_b}\right) - \frac{\partial^2}{\partial s_a \partial s_b}\left(K_{ab}^{B}\left(B_{ab} - B_{ab}^{0}\right)\right)\right] + \frac{\mathbf{F}_H}{V}. \tag{6.5}$$

Things that are expected to be observed during this process are signs of no air pockets and free surfaces as a result of pulsatile flow.

Future work also includes incorporation of the Womersley number which is a dimensionless expression used to characterize the unsteady flow in blood vessels [25]. A quantitative

study is to be considered where the values for the tension and shearing constants are chosen based on the mechanical properties of a human subject's cerebral arteries to be used in computing the dynamic equation for the motion of an elastic body. Incorporation of disparity in the tension and shearing coefficients of the artery to that of the aneurysm will need to be taken into consideration due to the artery wall, normally, being stiffer than the wall of its adjoining aneurysm.

Applying both the current model and three-dimensional model to actual angiographic configurations of a cerebral aneurysm will be considered as well as creating a boundary mesh for three clipping configurations and computing the flow of blood through the clipped aneurysms.

REFERENCES

[1] Arthurs, K.M., Moore, L.C., Peskin, C.S., Pitman, E.B. and Layton, H.E. (1998). "Modeling Arteriolar Flow and Mass Transport Using the Immersed Boundary Method." *Journal of Computational Physics.* **147**: 402–440.

[2] Bazilevs, Y., Calo, V.M., Zhang, Y. and Hughes, T.J.R. (2006). "Isogeometric fluid-structure interaction analysis with applications to arterial blood flow." *Comput. Mech.* **38**: 310–322.

[3] Bazilevs, Y., Hsu, M.-C., Zhang, Y., Wang, W., Kvamsdal, T., Hentschel, S. and Isaksen, J.G. (2010). "Computational vascular fluidstructure interaction: methodology and application to cerebral aneurysms." *Biomech Model Mechanobiol.* **9**: 481–498.

[4] Brieda, L. "Interpolation using an arbitrary quadrilateral." *pic-c.* Particle In Cell Consulting LLC., 4 June 2012. Retreived from https:www.particleincell.com/2012/quad-interpolation/.

[5] Brouillard, A.M., Sun, X., Siddiqui, A.H. and Lin, N. (2016). "The Use of Flow Diversion for the Treatment of Intracranial Aneurysms: Expansion of Indications." *Cureus.* **8**(1): e472.

[6] Carallo, C., Irace, C., Pujia, A., De Franceschi, M.S., Crescenzo, A., Motti, C., Cortese, C., Mattioli, P.L. and Gnasso, A. (1999). "Evaluation of Common Carotid Hemodynamic Forces: Relations With Wall Thickening." *Hypertension. Journal of the American Heart Association.* **34**: 217–221.

[7] Di, S. and Ge, W. (2015). "Simulation of dynamic fluidsolid interactions with an improved direct-forcing immersed boundary method." *Particuology.* **18**: 22–34.

[8] Endres, J., Kowarschik, M., Redel, T., Sharma, P., Mihalef, V., Hornegger, J. and Dörfler, A. (2012). "A Workflow for Patient-Individualized Virtual Angiogram Generation Based on CFD Simulation." *Computational and Mathematical Methods in Medicine.* **2012**: 24 pages.

[9] Ghaffari, S.A., Viazzo, S., Schneider, K. and Bontoux, P. (2015). "Simulation of forced deformable bodies interacting with two-dimensional incompressible flows: Application to fish-like swimming." *International Journal of Heat and Fluid Flow.* **51**: 88–109.

[10] Higashida, R.T. (2003). "What you should know about cerebral aneurysms." *American Stroke Association, A Division of American Heart Association.*

[11] Hirt, C.W. and Nichols, B.D. (1981). "Volume of Fluid (VOF) Method for the Dynamics of Free Boundaries." *Journal of Computational Physics.* **39**: 201–225.

[12] Huang, W-X. and Sung, H.J. (2009). "An immersed boundary method for fluid-flexible structure interaction." *Comput. Methods Appl. Mech. Engrg.* **198**: 2650–2661.

[13] Isaksen, J.G., Bazilevs, Y., Kvamsdal, T., Zhang, Y., Kaspersen, J.H., Waterloo, K., Romner, B. and Ingebrigtsen, T. (2008). "Determination of Wall Tension in Cerebral Artery Aneurysms by Numerical Simulation." *Stroke. Journal of the American Heart Association.* **39**: 3172–3178.

[14] Jansen, I.G.H., Schneiders, J.J., Potters, W.V., van Ooij, P., van den Berg, R., van Bavel, E., Marquering, H.A. and Majoie, C.B.L.M. (2014). "Generalized versus Patient-Specific Inflow Boundary Conditions in Computational Fluid Dynamics Simulations of Cerebral Aneurysmal Hemodynamics." *American Journal of Neuroradiology.* **35**(8): 1543–1548.

[15] Jeong, W. and Rhee, K. (2012). "Hemodynamics of Cerebral Aneurysms: Computational Analyses of Aneurysm Progress and Treatment." *Computational and Mathematical Methods in Medicine.* **2012**: 11 pages.

[16] Jiang, J. and Strother, C.M. (2013). "Interactive Decomposition and Mapping of Saccular Cerebral Aneurysms Using Harmonic Functions: Its First Application With Patient-Specific Computational Fluid Dynamics (CFD) Simulations." *IEEE Transactions on Medical Imaging.* **32**(2): 153–164.

[17] Jones, Z.R. (2014). "The Effect of Artery Bifurcation Angles on Fluid Flow and Wall Shear Stress in the Middle Cerebral Artery." Thesis(M.S.), California Polytechnic State University.

[18] Karmonik, C., Yen, C., Grossman, R.G., Klucznik, R. and Benndorf, G. (2009). "Intraaneurysmal flow patterns and wall shear stresses calculated with computational flow dynamics in an anterior communicating artery aneurysm depend on knowledge of patient-specific inflow rates." *Acta Neurochir.* **151**: 479–485.

[19] Kim, J., Kim, D. and Choi, H. (2001). "An Immersed-Boundary Finite-Volume Method for Simulations of Flow in Complex Geometries." *Journal of Computational Physics.* **171**: 132–150.

[20] Le, D.V., White, J., Peraire, J., Lim, K.M. and Khoo, B.C. (2009). "An implicit immersed boundary method for three-dimensional fluid-membrane interactions." *Journal of Computational Physics.* **228**: 8427–8445.

[21] Lee, I. and Choi, H. (2014). "A discrete-forcing immersed boundary method for the fluid-structure interaction of an elastic slender body." *Journal of Computational Physics.* **280**: 529–546.

[22] Li, Y., Yun, A. and Kim, J. (2012). "An immersed boundary method for simulating a single axisymmetric cell growth and division." *J. Math. Biol.* **65**: 653–675.

[23] Lind, L., Andersson, J., Larsson, A. and Sandhagen, B. (2009). "Shear stress in the common carotid artery is related to both intima-media thickness and echogenecity." *Clinical Hemorheology and Microcirculation.* **43**: 299–308.

[24] Lott, D.A., Siegel, M., Chaudhry, H.R. and Prestigiacomo, C.J. (2009). "Computational fluid dynamic simulation to assess flow characteristics of an in vitro aneurysm model." *J. NeuroIntervent Surg.* **1**: 100–107.

[25] Loudon, C. and Tordesillas, A. (1998). "The Use of the Dimensionaless Womersley Number to Characterize the Unsteady Nature of Internal Flow." *J. Theor. Biol.* **191**: 63–78.

[26] Marzo, A., Singh, P., Larrabide, I., Radaelli, A., Coley, S., Gwilliam, M., Wilkinson, I.D., Lawford, P., Reymond, P., Patel, U., Frangi, A. and Hose, D.R. (2011). "Computational Hemodynamics in Cerebral Aneurysms: The Effects of Modeled Versus Measured Boundary Conditions." *Annals of Biomedical Engineering.* **39**(2): 884–896.

[27] Meuschke, M., Voss, S., Beuing, O., Preim, B. and Lawonn, K. (2017). "Combined Visualization of Vessel Deformation and Hemodynamics in Cerebral Aneurysms." *IEEE Transactions on Visualization and Computer Graphics.* **23**(1): 761–770.

[28] Mikhal, J. (2012). "Modeling and simulation of flow in cerebral aneurysms." *Ph.D. Thesis, University of Twente, P.O. Box 217, 7500 AE Enschede, The Netherlands*

[29] Morales, H.G., Larrabide, I., Geers, A.J., Roman, L.S., Blasco, J., Macho, J.M. and Franji, A.F. (2013). "A Virtual Coiling Technique for Image-Based Aneurysm Models by Dynamic Path Planning." *IEEE Transactions on Medical Imaging.* **32**(1): 119–129.

[30] Mori, Y. and Peskin, C.S. (2008). "Implicit second-order immersed boundary methods with boundary mass." *Comput. Methods Appl. Mech. Engrg.* **197**: 2049–2067.

[31] Oubel, E., Cebral, J.R., DeCraene, M., Blanc, R., Blasco, J., Macho, J., Putman, C.M. and Frangi, A.F. (2010). "Wall motion estimation in intracranial aneurysms." *Physiological Measurement.* **31**: 1119–1135.

[32] Paál, G., Ugron, A., Szikora, I. and Imre Bojtár, I. (2007). "Flow in simplified and real models of intracranial aneurysms." *International Journal of Heat and Fluid Flow.* **28**: 653–664.

[33] Rossitti, S. (1998). "Shear Stress in Cerebral Arteries Carrying Saccular Aneurysms." *Acta Radiologica.* **39**(6): 711–717.

[34] Seibold, B., "A compact and fast Matlab code solving the incompressible Navier-Stokes equations on rectangular domains." 31 March 2008. Retreived from www-math.mit.edu/cse.

[35] Shen, L. and Chan, E-S. (2008). "Numerical simulation of fluid-structure interaction using a combined volume of fluid and immersed boundary method." *Ocean Engineering.* **35**: 939–952.

[36] Shishir, S.S., Miah, A.K., Islam, A.K.M.S. and Hasan, A.B.M.T. (2015). "Blood Flow Dynamics in Cerebral Aneurysm - CFD Simulation." *Procedia Engineering.* **105**: 919–927.

[37] Sugiyama, S.-I., Meng, H., Funamoto, K., Inoue, T., Fujimura, M., Nakayama, T., Omodaka, S., Shimizu, H., Takahashi, A. and Tominaga, T. (2012). "Hemodynamic Analysis of Growing Intracranial Aneurysms Arising from a Posterior Inferior Cerebellar Artery." *World Neurosurg.* **78**(5): 462–468.

[38] Tateshima, S., Chien, A., Sayre, J., Cebral, J. and Viñuela, F. (2010). "The effect of aneurysm geometry on the intra-aneurysmal flow condition." *Interventional Neuroradiology.* **52**: 1135–1141.

[39] Torii, R., Oshima, M., Kobayashi, T., Takagi, K. and Tezduyar, T.E. (2009). "Fluidstructure interaction modeling of blood flow and cerebral aneurysm: Significance of artery and aneurysm shapes." *Comput. Methods Appl. Mech. Engrg.* **198**: 3613–3621.

[40] Tremmel, M., Xiang, J., Natarajan, S.K., Hopkins, N., Siddiqui, A.H., Levy, E.I. and Meng, H. (2010). "Alteration of Intraaneurysmal Hemodynamics for Flow Diversion Using Enterprise and Vision Stents." *World Neurosurgery.* **74**: 306–315.

[41] Udaykumar, H.S., Mittal, R., Rampunggoon, P. and Khanna, A. (2001). "A Sharp Interface Cartesian Grid Method for Simulating Flows with Complex Moving Boundaries." *Journal of Computational Physics.* **174**: 345–380.

[42] Valen-Sendstad, K., Mardal, K.-A. and Steinman, D.A. (2013). "High-resolution CFD detects high-frequency velocity fluctuations in bifurcation, but not sidewall, aneurysms." *Journal of Biomechanics.* **46**: 402–407.

[43] Valencia, A., Burdiles, P., Ignat, M., Mura, J., Bravo, E., Rivera, R. and Sordo, J. (2013). "Fluid Structural Analysis of Human Cerebral Aneurysm Using Their Own Wall Mechanical Properties." *Comput Math Methods Med.* **2013**: 11 pages.

[44] Valencia, A. and Solis, F. (2006). "Blood flow dynamics and arterial wall interaction in a saccular aneurysm model of the basilar artery." *Computers and Structures.* **84**: 1326–1337.

[45] Vanella, M., Rabenold, P. and Balaras, E. (2010). "A direct-forcing embedded-boundary method with adaptive mesh refinement for fluidstructure interaction problems." *Journal of Computational Physics.* **229**: 6427–6449.

[46] Ventikos, Y., Holland, E.C., Bowker, T.J., Watton, P.N., Kakalis, N.M.P., Megahed, M., Zhu, F., Summers, P.E. and Byrne, J.V. (2009). "Computational modelling for cerebral aneurysms: risk evaluation and interventional planning." *The British Journal of Radiology*. **82**: S62–S71.

[47] Wang, C. and Eldredge, J. (2015). "Strongly coupled dynamics of fluids and rigid-body systems with the immersed boundary projection method." *Journal of Computational Physics*. **295**: 87–113.

[48] Wong, G.K.C. and Poon, W.S. (2011). "Current status of computational fluid dynamics for cerebral aneurysms: The clinicians perspective." *Journal of Clinical Neuroscience*. **18**: 1285–1288.

[49] Wu, Y., Yang, P.F., Shen, J., Huang, Q.H., Zhang, X., Qian, Y. and Liu, J.M. (2012). "A comparison of the hemodynamic effects of flow diverters on wide-necked and narrow-necked cerebral aneurysms." *Journal of Clinical Neuroscience*. **19**: 1520–1524.

[50] Xenos, M.A. (2017). "An Euler-Lagrange approach for studying blood flow in an aneurysmal geometry." *Proceedings Royal Society A*. **473**(2199).

[51] Xu, S. and Wang, J.Z. (2006). "An immersed interface method for simulating the interaction of a fluid with moving boundaries." *Journal of Computational Physics*. **216**: 454–493.

[52] Yang, J. and Stern, F. (2012). "A simple and efficient direct forcing immersed boundary framework for fluidstructure interactions." *Journal of Computational Physics*. **231**: 5029–5061.